Volume 7 • No 2 • Dec 2019 • ARO ISSN: 2410-9355 • DOI: 10.14500/2307-549X

ARO

The Scientific Journal of Koya University

Removal of Listeria monocytogenes Biofilm with Some Local Plant Extracts of Kurdistan Region • Synthesis of new series of Pyrazoline, and study their Kinetics and Reaction Mechanism • Electrical and Structural properties of Copper Oxide (CuO) thin films on Plastic substrate deposited by spray pyrolysis technique • L-Tryptophan as Fluorescent Probe for Determination of Folic Acid in Pharmaceutical Products • Aqra Anticline: A Growing Structure in the Iraqi Kurdistan Region • High-Performance Ultra-Compact Dual-Band Bandpass Filter for Global System for Mobile Communication-850/Global System for Mobile Communication-1900 Applications • Pollution Problems in Koya City due to Private Electrical Generators • Docking Study to Predict the Efficacy of Phosphatidylinositol 3-Kinase α Inhibitors • Education Needs to Support Architecture, Engineering, and Construction Collaboration Using Building Information Modeling • Skin Temperature Distribution over Human Head Due to Handheld Mobile Phone Call using Thermal Imaging Camera • Theoretical Study of the [4+2] Cycloaddition Reaction of Trifluoroethylene with Five-membered Chalcogens Heterocyclic Compounds.

ISSN: 2410-9355 (printed version) **ISSN: 2307-549X (electronic version)**
ARO - DOI: 10.14500/2307-549X

ARO-The Scientific Journal of Koya University

The ARO ("Today" in Hewramí Kurdish), is an international scientific journal published by the Koya University with p-ISSN: 2410-9355, e-ISSN: 2307-549X and DOI: 10.14500/2307-549X. ARO is a journal of original scientific research, global news, and commentary. The ARO Scientific Journal is a peer-reviewed, open access journal that publishes original research articles as well as review articles in all areas of Science and Engineering.

ARO the Scientific Journal Office

Koya University, University Park
Danielle Mitterrand Boulevard, Koya KOY45
Kurdistan Region - F.R. Iraq

Tel.: +964 (0) 748 012 7423
Mobile: +964 (0) 750 187 5489
E-mail: aro.journal@koyauniversity.org
url: aro.koyauniversity.org

December - 2019 | Befranber – 2719

ARO

The Scientific Journal of Koya University

Vol VII, No 1(2019)

Contents

ARO Editorial Words

Dear readers,

ARO, the Scientific Journal of Koya University, is closing its Issue Thirteen (Vol VII, No 2, 2019). It has been a challenging, exciting and yet progressive season for our journal. ARO has managed to publish 11 original research articles that show our commitment to publishing quality original works. ARO is publishing its 13th issue as an internationally listed Scientific Journal in Kurdistan Region of Iraq. Notably, ARO has been accepted for indexing in the Emerging Sources Citation Index (ESCI), a new edition of Web of Science™ as of Feb 2016. Content in this issue is under consideration by Clarivate Analytics to be accepted in the Science Citation Index Expanded™ (SCIE) during 2019. ARO's individual articles are currently listed by Clarivate Analytics using articles unique DOI numbers which is a historical achievement for our academic community. ARO is starting its seventh-year journey in leading the quality of regional scientific publications with global impact. The editorial team have been working tirelessly to keep the novel mission and sustain ARO's future publications with greater impacts and citations. It is exciting that ARO has been awarded to DOAJ Seal listing which is an indication of a trusted high standard open access scientific work. The upcoming new season will be an even more exciting period in ARO's life as Clarivate Analytics will examine our journal for a full permanent listing.

ARO was created with a long-term vision of becoming accessible to all researchers in Kurdistan and beyond, and covering a wide range of scholarly disciplines in the sciences. ARO is a peer-reviewed, open-access journal that publishes original scientific research, global news, letters and commentary as well as review articles in areas of natural sciences and technology. In this issue, you will have access to original research papers in a variety of areas, such as Physics, Chemistry, Biology, Material Science, Civil Engineering, Architectural Engineering, Software Engineering, Electrical and Electronics Engineering, Petroleum Engineering and Geology.

The great responses from researchers, academics and professionals in the last six years have made us create a wider Editorial Board which serves the wider submitted scientific manuscripts. However, it is clear that having a dedicated and well-organised editorial board for the journal is only one side of the coin. The other is the ability to attract submissions of quality research and scholarly work. We are thankful to all of those who put their trust in Aro and presented their original research work for publication in Vol VII, No 2 (2019) of the journal, as well as, our thanks are extended to the 19 peer-reviewers from the Universities worldwide for their efforts in reviewing and enabling this issue of ARO.

Your support and feedback are invited and appreciated.

Dilan M. Rostam
Editor-in-Chief

Wali M Hamad
Executive Publisher

Dilan M. Rostam, Salah I. Yahya, Basim M. Fadhil, Fahmi F. Muhammad, Mohammed H. S. Zangana, Jorge Correia, Executive Editor, Fouad Mohammed, Jacek Binda, Nadhir Al-Ansari, Howri Mansurbeg, Tara Fuad Tahir, Yazen A. Khaleel.
Executive Editorial Board

DOI: 10.14500/2307-549X ARO p-ISSN: 2410-9355, e-ISSN: 2307-549X

Removal of *Listeria monocytogenes* Biofilm with Some Local Plant Extracts of Kurdistan Region, Iraq

Srwa A. Mohammed

Department of Medical Microbiology, Faculty of Science and Health, Koya University, Koya, KOY45, Kurdistan Region - F.R. Iraq

***Abstract*—The results of removing or reducing biofilm were determined using subinhibitory concentrations (SICs) of some local plants in the flora of Kurdistan region of Iraq on biofilm production in *Listeria monocytogenes*. About 10–500 µg/ml of the plant extracts were used against growth and biofilm production in tissue culture plates which were measured spectroscopically. The SIC effects of each of *Eugenia caryophyllata* (Clove) and *Rhus glabra* (Sumac) have significantly affected on planktonic cells and reduced sessile cells or biofilm formation in *L. monocytogenes*. Remarkably, the data showed strong biofilm reduction under synergistically effect of the plant extract mixed with the antimicrobial agents in multidrug-resistant *L. monocytogenes*. Whereas the SIC some of other plant extracts such as *Salix candida* and pomegranate (*Punica granatum*) have significantly enhanced biofilm expression in *L. monocytogenes,* but the use of these extracts synergistically with some antibiotics also resulted in inhibition of biofilm in comparison to merely use of either the extracts or antibiotics. The result of statistical analyses shows that $P > 0.05$. The results showed that the combination of plant extract with antibiotic together has more effect than using plant merely.**

***Index Terms*—Biofilm, *Eugenia caryophyllata, Listeria monocytogenes, Salix candida*.**

I. Introduction

Biofilm is an organized aggregate of microorganisms living within an extracellular polymeric matrix that they produce and irreversibly attached to fetish or living surface which will not remove unless rinse quickly (Hurlow, et al., 2015).

Cell-to-cell communication is an important process, during which the required microbial cell density is attained. This leads to the secretion of signaling molecules, known as autoinducers. These autoinducers facilitate quorum sensing. At this stage of maturation, certain gene products are expressed that are considered important for the formation of extracellular polymeric substances (EPS). Since EPS is the main material in the biofilm's three-dimensional structure, interstitial voids are then produced in the matrix (Muhsin, et al., 2018).

ARO-The Scientific Journal of Koya University
Volume VII, No.1(2019), Article ID: ARO.10385, 4 pages
DOI: 10.14500/aro.10385
Received 21 January 2019; Accepted 10 August 2019
Regular research paper: Published 10 December 2019
Corresponding author's e-mail: srwa.ali@koyauniversity.org

Biofilms occur on a wide variety of surfaces including living tissues, industrial equipment, and food processing surfaces such as conveyor belts, plastic, and stainless steel equipment. Since bacterial cells can be easily transferred from biofilms to food products, biofilms formed by pathogens such as *Listeria monocytogenes* are of particular concern for food industries. It has been demonstrated that *L. monocytogenes* can grow and form biofilms on several food processing surfaces including rubber, plastics, glass, and stainless steel. Biofilms of listeria protect cells from the action of antimicrobials and sanitizers, potentially allowing long-term persistence of the microorganism in the food processing environment (Giuseppe, et al., 2013).

Biofilm organisms have an inherent resistance to antibiotics, disinfectants, and germicides. The use of synthetic material for implantation is widely associated with "implant-associated infection" due to biofilm production. In the long run, they may be very damaging due to immune complex disease (Donlan and Costerton, 2002; García-Almendárez, et al., 2007).

Plant-derived compounds have gained widespread interest in the search to identify the alternatives for microbial control (Essawi and Srour, 2000). The compounds are widely accepted due to the perception that they are safe and have a long history of use in folk medicine for the prevention and treatment of diseases and infections (Guarrera, 2005). The present study was focused on using plant extracts at sub-minimum inhibition concentration (MIC) against the clinically relevant *L. monocytogenes* biofilms.

II. Materials and Methods

Twelve local plants used in this study. Some of them were obtained from Koya Haebatsultan and others from local market in Sulaimani city.

A. Screening of Biofilm Production

L. monocytogenes isolate that produce biofilm was received from Srwa, 2014, for the current study. Confirmation tests were done through colony morphology and biochemical tests. The isolate was subcultured and the control was prepared in tryptic soy broth (TSB) for 18 h at 37°C. Before the experiments, the strain was vortexed for 5 min and the optical density adjusted to 1–1.5 at 600 nm by spectrophotometer according to McFarland scale to the overnight culture was standardized to a concentration of 3×10^8 CFU/ml.

The strain diluted by obtaining 50 µl of sample to 950 µl broth aliquots of 200 µl transferred to pre-sterilized, 96-well polystyrene microtiter plates commercially available (Deltalab S.L., Spain), then incubated for 24 h at 37°C. After incubation, discard the bacterial suspension totally each well was washed with 200 µl sterile phosphate buffer solution (PBS), then put on the hot plate for 1 h at 60°C for fixation, 25 µl of 1% crystal violet was added to each well, after 15 min at room temperature, each well was washed with 200 µl sterile PBS. The absorbance was determined at wavelength 450–630 nm in an enzyme-linked immunosorbent assay microtiter (Botic England). Controls were performed with crystal violet binding to the wells exposed only to the culture medium without bacteria (Bose, et al., 2009).

B. Plants Classification

The plants were classified by Dr. Eqbal Muhammed Xareb. She is assistant prof. in Koya University/Biology Department and her specialty is horticulture, apple leaves (*Malus domestica*), leaves of *Quercus infectoria*, leaves of bitter vetch (*Lathyrus montanus*), clove (*Eugenia caryophyllata*), and sumac (*Rhus glabra*), *Portulaca oleracea*, *Vitis vinifera* leaves, and *Citrullus colocynthis*, *Anthemis tinctoria* (*Matricaria chamomilla*), *Salix candida*, leaves *Pistacia terebinthus,* and pomegranate (*Punica granatum*).

C. Preparation of Methanol Crude Extracts

The plant samples were collected, and 12 plant extracts were prepared using absolute methanol; add 10 g of grinded plants to the conical flask. Then, 25 ml of absolute methanol was added to the flask then placed in the refrigerator for 3 days. After 72 h, the extracts were filtered through a Whatman filter paper No. 42 (125 mm) and it concentrated using a rotary evaporator (Laborota 4000, SN 090816862, Germany) (Odey, et al., 2012). At the final step, the extracted was transferred into vials and stored at 4°C.

D. Determination of MIC

The minimum inhibitory concentration (MIC) of medicinal plant extracts understudying was determined by turbidity method (spectrophotometric method) at 600 nm, and the following dilutions were prepared for each extract (10, 20, 30, 40, 50, 60, 70, 80, 100, 200, 300, 400, 500, 600,700, 800, 1000, and 1100 µM) (Ncube, et al., 2008), according to the plant activity, sub-MIC was adjusted. A stock solution of the extracts directly used without dilution, with the control of the bacterial suspension that prepared previously by two methods: 1 – 0.5 ml of the bacterial suspension was put in the wells of the (96-well polystyrene microtiter) plates and the plant extracts was added directly and 2 – 0.5 ml of the bacterial suspension of *L. monocytogenes* was put in the wells of the microtiter plate and was incubated for 24 h to allow set the sessile or biofilm formation. Then, it was mixed with the plant extracts at sub-MIC for each of the 12 extracts. Each well was compared with the control well (Djordjevic, et al., 2002).

E. Susceptibility Test

Antibiotic susceptibility test was conducted for biofilm that produces by *L. monocytogenes* isolate and was used eight extra high-performance liquid chromatography (Sigma) antimicrobials powder that has 100% activity. The bacterial strains were inoculated into TSB and incubated for 24 h at 37°C to allow forming biofilm; then, MIC of antimicrobial agents was added to microwells after discard the bacterial suspension (NCCLS, 2000). The antimicrobial agents that were used [ampicillin (AMP), chloramphenicol (CHL), nalidixic acid (NAL), Rifampin (RIF), Tetracycline (TET), Carbincillin (CAR), Streptomycin (STR), and neomycin (N)].

F. Combination Effect of Antimicrobial Agents with Some Effective Plants on Biofilm

The extracts at sub-MIC were mixed with antimicrobial agents at sub-MIC in sterile Eppendorf tubes. The mixtures were transferred into the wells of the 96 microtiter plates which contain biofilm of *L. monocytogenes* isolate, to determine the nature of the interactions between the extracts and antimicrobial agents using Equation 1 (Srwa and Shwan, 2017).

$$\frac{MIC_{xy}\,in\ combination}{MIC_{x}\,alone}+\frac{MIC_{xy}\,in\ combination}{MIC_{y}\,alone} \qquad 1$$

G. Statistical Analyses

Z score was done for double OD before 10 h incubation and after 10 h incubation. The result was 1.58 from Z score and $P = 0.11$. The result shows that $P > 0.05$ (Richard and Morris, 2000).

III. Results and Discussion

A. Reducing Biofilm Formation in L. monocytogenes by 12 Different Types of Plant Extract

Twelve different types of plant extract were screened for their antimicrobial activities against both planktonic and sessile or biofilm bacteria. First method: The extracts were initially tested on planktonic microorganisms using the MIC assay. The results showed clove (*E. caryophyllata*), *A. tinctoria* (*M. chamomilla*), *S. candida,* leaves *P. terebinthus,* and sumac (*R. glabra*); crude extracts have good effect on inhibiting *L. monocytogenes*. About 0.5 ml of the bacterial suspension from control sample was mixed with the crude methanol plant extracts 10, 40, 80, 500, and 500 µl/ml, respectively, and incubating overnight, then culturing on nutrient agar. The results show no growth isolated for each of them. Meanwhile, some of the extracts can be used such as supportive media or such as nutrient for bacteria. The study of Nyila, et al., 2012 used 13 different sorts of plant extract against *L. monocytogenes* planktonic cells and showed that epigallocatechin was found to be active against *L. monocytogenes* at a concentration of 0.062 mg/ml. While, (Nzeako and Lawati, 2008) used thyme and clove essential oils as antifungal agents and showed growth inhibitions of more than 25 mm (diameter) up to 1:16

dilution. And showed the minimum fungicidal concentration (MFC) of thyme and clove for all the organisms were 1.9 x 10^3 µg/mL for thyme and 2.5 x 10^3 µg/mL for clove. Second method: Treating *L. monocytogenes* that produce biofilm with 12 different types of plant extracts were tested on sessile cells or biofilm formation after incubating for 24 h and set the biofilm. The results are shown in Fig. 1.

Fig. 1 shows the effect of crude methanol extracts of *Q. infectoria* leaves, leaf of bitter vetch (*L. montanus*), bark of clove (*E. caryophyllata*), and seed of sumac (*R. glabra*). In the well (A3, A9, A11, and C8) (0.191, 0.181, 0.284, and 0.178, respectively), they have good effects on reducing biofilm that produces by *L. monocytogenes,* by adding 35, 35, 8, and 8 µl, respectively, of the extracts at sub-MIC in the prepared well previously by adding bacterial suspension and incubating for 24 h till biofilm set by tested isolate and discard the suspension just remain biofilm in the wells. The results were read by ELIZA and well A1 shows control of *L. monocytogenes* OD reading was 1.192.

On the other hand, some of the plant extracts enhance or increase biofilm formation such as *P. oleracea*, *S. candida, P. granatum*, *V. vinifera* leaves, and *C. colocynthis* in the A4, B6, B9, C1, and C2, respectively, and OD reading for each of them was 3.22, 2.50, 2. 34, 5.60, and 6.32, respectively, as shown in Fig. 1. The present study in accordance with the study of Sandasi, et al., 2010, used 16 different types of plant including clove against three pathogenic microorganisms (*L. monocytogenes*, *Pseudomonas aeruginosa*, and *Candida albicans*), but peppermint was the only extract that showed the best antibiofilm activity against all the tested organisms on a preformed biofilm and also showed that the inhibition of growth of a preformed biofilm was more difficult to achieve resulting in most of the extracts enhancing the growth of the biofilms. Furthermore, the study of Nyila, et al., 2010, showed listerial biofilms, treated with *Syzygium aromaticum* or *Mentha spicata* essential oils, and exhibited the same biomass (absorbance 0.09) as that of the positive control (ciprofloxacin). It was, therefore, assumed that the antilisterial activity of these essential oils could be attributed to the activity of their major chemical constituents, eugenol, and carvone. However, surprisingly, these compounds alone caused biofilm enhancement rather than inhibition.

B. Susceptibility Test

Susceptibility test was conducted for biofilm that produces by *L. monocytogenes*, eight widely antimicrobials at final concentration were used (AMP, NAL, N, STR, CHL, RIF, TET, and CAR) in well (A1, A2, A3, A4, A5, A6, A7, and A8, respectively), which demonstrated in Fig. 2. OD reading of biofilm that produces by *L. monocytogenes* was 1.195, but when exposed to the antibacterial agents, the relative activity of the biofilm was markedly higher than that in single-species biofilms and the optical density reading of biofilm was 1.439, 1.293, 1.164, 1.144, 1.163, 1.171, 1.104, and 1.092, respectively, as shown in Table I. The study of Burmølle, et al., 2006, was found to interact synergistically in biofilms formed in 96-well microtiter plates: Biofilm biomass was observed to increase by >167% in biofilms formed by the four strains compared to biofilms composed of single strains.

TABLE I
SUSCEPTIBILITY TEST FOR BIOFILM THAT DEVELOPED BY *LISTERIA MONOCYTOGENES* ISOLATE

Isolate	Control	AMP	NAL	N	STR	CHL	RIF	TET	CAR
Listeria monocytogenes	A9	A1	A2	A3	A4	A5	A6	A7	A8
	1.192	1.439	1.293	1.164	1.144	1.163	1.171	1.151	1.092

AMP: Ampicillin, NAL: Nalidixic acid, N: Neomycin, STR: Streptomycin, CHL: Chloramphenicol, RIF: Rifadin, TET: Tetracycline, CAR: Carbenicillin

TABLE II
THE EFFECTS OF COMBINATION ANTIBIOTICS AND SOME PLANT EXTRACTS ON BIOFILM PRODUCED BY *LISTERIA MONOCYTOGENES*

Listeria monocytogenes	RIF	TET	STR	N	AMP
Clove	B1 0.155	B2 0.192	B3 0.108	B5 0.111	B11 0.179
Pomegranate	B6 0.131	B7 0.091	B8 0.106	B9 0.178	B10 0.124
Sumac (*Rhus anacardiaceae*)	A12 0.253	B12 0.182	C1 0.118	C2 0.177	C3 0.112
Salix candida	C6 0.075	C7 0.055	C8 0.056	C9 0.091	C5 0.065

RIF: Rifadin, TET: Tetracycline, STR: Streptomycin, N: Neomycin, AMP: Ampicillin

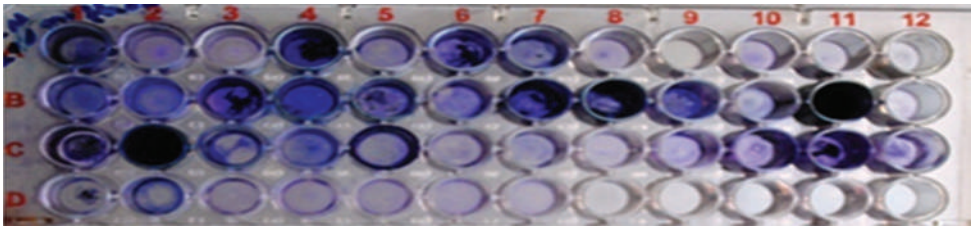

Fig. 1. Treating *Listeria monocytogenes* biofilm with 12 different types of plant extracts.

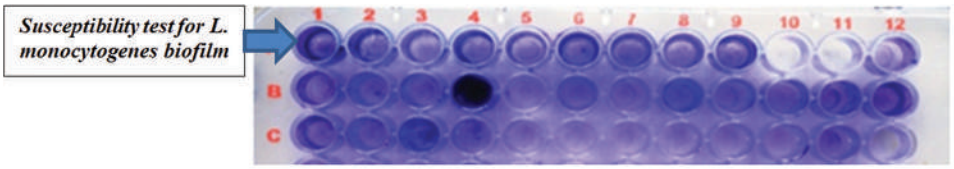

Fig. 2. Treating *Listeria monocytogenes* biofilm with antimicrobial agents and mixed (antimicrobial agents with plant extracts).

When exposed to the antibacterial agent hydrogen peroxide or TET, the relative activity (exposed versus non-exposed biofilms) of the four-species biofilm was markedly higher than that in any of the single-species biofilms.

C. Treating L. monocytogenes Biofilm with Mixed Antimicrobial Agents and Plant Extracts

Combination of five different sorts of antimicrobial agents mixed with three different plant extracts such as clove (*E. caryophyllata*), pomegranate, sumac (*R. glabra*), and *S. candida* separately. They have good effects on reducing biofilm as shown in Fig. 2. The OD reading for each of them demonstrates in Table II. The present study showed synergistic activity between antimicrobial agents and these plant extracts and this agrees with the study of Srwa and Shwan, 2017 showed in their study synergistic activity between plant extracts and antimicrobial agents on biofilm produced by *Klebsiella pneumonia.*

In general, sumac (*Rhus anacardiaceae*) and clove (*E. caryophyllata*) were the only two extracts with low concentration showed good antibiofilm activity and good antibacterial activity against *L. monocytogenes,* while some of the extracts enhanced bacterial activity and biofilm development. And the use of these extracts synergistically with some antibiotics also resulted in inhibition of biofilm in comparison to merely use of either the extracts or antibiotics. There is little study about reducing biofilm by traditional herbs or plants, while many researches nowadays carried out about inhibition of bacterial activity.

IV. Conclusion

The results show that the reduction of biofilm mass using plant extracts has good effect, but using the combination of plant and antibiotic together has more effect than using plant solely.

Acknowledgments

We would like to express our deepest and warmest gratitude to the entire members in Science and Health Research Center (SHRC) of Koya University for their help and kindness.

References

Bose, S., Khodke, M., Basak, S., and Malick, S.K., 2009. Detection of biofilm producing staphylococci: need of the hour. *Journal of Clinical and Diagnostic Research*, 3(6), pp.1915-1920.

Burmølle, J.S.W., Dhana R., Lars H.H., Søren J.S.M., and Staffan, K., 2006. Enhanced Biofilm formation and increased resistance to antimicrobial agents and bacterial invasion are caused by synergistic interactions in multi species biofilms. *Journal of American Society for Microbiology Applied and Environmental Microbiology*, 72(6), pp.3916-3923.

Djordjevic, D., Wiedmann, M., and Mclandsborough, L.A., 2002. Microtitre plate assay for assessment of *Listeria monocytogenes* biofilm formation. *Applied and Environmental Microbiology*, 68(6), pp.2950-2958.

Donlan, R.M., and Costerton, W., 2002. Biofilms: Survival mechanisms of clinically relevant microorganisms. *Clinical microbiological Review*, 15(2), pp.167-193.

Essawi, T., and Srour, M., 2000. Screening of some palestinian medicinal plants for antibacterial activity. *Journal Ethnopharmacology*, 70(3), pp.343-349.

García-Almendárez, B.E., Cann, I.K.O., Martin, S.E., Guerrerro-Legrreta, I., and Regalado, C., 2007. Effect of *Lactococcus lactis* UQ2 and its bacteriocin on *Listeria monocytogenes* biofilms. *Food Control*, 19, pp.670-680.

Giuseppe, B., Russo, P., Capozzi, V., Amodio, M.L., Giuseppe, S., and Luciano, B., 2013. *Listeria monocytogenes*, biofilm formation and fresh cut produce. *Food and Environmental Sciences*, pp.114-123.

Guarrera, P.M., 2005. Traditional phytotherapy in central Italy (Marche, Abruzzo, and Latium). *Fitoterapia*, 76(1), pp.1-25.

Hurlow, J., Couch, K., Laforet, K., Bolton, L., Metcalf, D., and Bowler, P., 2015. Clinical biofilms: A challenging frontier in wound care. *Adv Wound Care*, 4, pp.295-301.

Muhsin, J., Wisal, A., Saadia, A., Fazal, J., Muhammad, I., Muhammad, A.N., Tahir, H., Muhammad, A., Muhammad, R., and Muhammad, A.K., 2018. Bacterial biofilm and associated infections. *Journal of the Chinese Medical Association*, 81(1), pp.7-11.

National Committee for Clinical Laboratory Standards (NCCLS). 2000. *Methods for Dilution Antimicrobial Susceptibility Tests for Bacteria that Grow Aerobically*. National Committee for Clinical Laboratory Standards, Wayne, PA.

Ncube, N.S., Afolayan, A.J., and Okoh, A.I., 2008. Assessment techniques of antimicrobial properties of natural compounds of plant origin: Current methods and future trends. *African Journal of Biotechnology*, 7(12), pp.1797-1806.

Nyila, M.A., Leonard, C.M., Hussein, A.A., and Lall, N., 2012. Activity of South African medicinal plants against *Listeria monocytogenes* biofilms, and isolation of active compounds from *Acacia karroo. South African Journal of Botany*, 78, pp.220-227.

Nzeako, B.C., and Lawat, B.A., 2008. Comparative studies of antimycotic potential of thyme and clove oil extracts with antifungal antibiotics on *Candida albicans*. *African Journal of Biotechnology*, 7(1), pp.1612-1619.

Odey, M.O., Iwara, I.A., Udiba, U.U., Johnson, J.T., Inekwe, U.V., Asenye, M.E., and Victor, O., 2012. Preparation of plant extracts from indigenous medicinal plants. *International Journal of Science and Technology*, 1(12), pp.688-692.

Richard, J.L., and Morris, L.M., 2000. *An Introduction to Mathematical Statistics and its Applications*. 3rd ed. Prentice-Hall, New Jersey, p.282.

Sandasi, M., Leonard, C.M., and Viljoen, A.M., 2010. The *in vitro* antibiofilm activity of selected culinary herbs and medicinal plants against *Listeria Monocytogenes*. *Letters in Applied Microbiology*, 50(1), pp.30-5.

Srwa, A.M., 2014. Biofilm determination of *Listeria monocytogenes* that isolated from different sources. *Journal of Life Science*, 8(10), pp.1-5.

Srwa, A.M., and Shwan, K.R., 2017. Inhibition of biofilmi production in multi-drug resistant *Klebsiella pneumonia* by extract of some plants in the flora of Koya city. *Proceedings ICNS Charmo Journal*, 2, pp.60-67.

Synthesis of Novel Series of Pyrazoline, and Study their Kinetics and Reaction Mechanism

Kosrat N. Kaka, Salam G. Taher, Wali M. Hamad and Aram H. Ibrahim

Department of Chemistry, Faculty of Science and Health, Koya University,
Koya KOY45, Kurdistan Region – F.R. Iraq

***Abstract*—A new series of novel pyrazoline compounds were synthesized by addition of thiosemicarbazide to the 2,6-dibenzylidenecyclohexanone (Chalcone) and its parasubstituted derivatives. This study was conducted for four purposes. First, a series of five-membered ring pyrazoline compounds were synthesized, and the structure of all new products obtained is supported by spectral data (^{1}H-NMR, ^{13}CNMR, infrared, and ultraviolet [UV]-visible), and the effect of substituents was studied. Second, the reaction kinetics of the newly synthesized compounds was studied to investigate the reaction mechanism pathway and order of the reaction; it was found that the reaction undergoes through Claisen route of mechanism with first-order reaction. Third, the thermodynamics of the reaction were studied, the rate of the reaction, Arrhenius parameters (A), and thermodynamic parameters for activation includes free energies (E_a), entropies ($\Delta S^{\#}$), and Gibbs free energy ($\Delta G^{\#}$) were estimated. Finally, the compensation effect was also studied and found the same pathway for all of the synthesized pyrazoline compounds.**

***Index Terms*—Pyrazolines, Kinetics, Mechanism, Chalcones, Compensation effect, Thiosemicarbazide, Claisen and Michael Pathway.**

I. Introduction

Nucleophilic addition to α, β-unsaturated carbonyl compound as aldehydes, ketones carboxylic acids, and esters is one of the common reactions in organic synthesis. The presence of two conjugated functional groups C=C and C=O in the structure of α, β-unsaturated carbonyl compounds ease the nucleophilic addition reaction to occur frequently (Esmaeel, 1988). Moreover, α, β-unsaturated enones are important intermediate in many addition reactions of nucleophiles due to inductive polarization of carbonyl group at the β position (Ebenezer and Wight, 1995, Hamad et al., 2016). Furthermore, electrophilic addition (McCrae, 1973), Claisen addition (Carey, 1996), and Michael addition (Gutsche, 1967) are the most known types of such kind of reactions, and the use of heterocyclic compounds is the most common, due to their interesting biological activities.

Pyrazoline is a heterocyclic compound that contains two adjacent nitrogen atoms; it can be synthesized using variety of methods. Pyrazoline compounds are not stable; readily convert to cyclopropane derivatives in the presence of heat or base catalyst (Qiu et al., 2008; Ramage et al., 1957). Pyrazoline and its derivatives are important compounds which constitute the basic framework of certain drug (Patel et al., 2011); also they are important precursors for pharmaceuticals and pesticides (Sloop et al., 2008).

Pyrazoline compounds show a variety of biological activates such as anticonvulsant (Beyhan et al., 2017), antimicrobial (Joshi et al., 2012, Pandya et al., 2017, Kendre and Baseer, 2013, Hassan, 2011) antituberculosis, antileishmanial (Monga et al., 2014), and antifungal properties (Hassan, 2011).

There are several works that have been published for the synthesis of pyrazolines. Mainly, the pyrazoline synthesis is based on the cyclization reaction of different chalcones with hydrazine compounds (Li et al., 2007, Lévai, 2005, Powers et al., 1998, Joshi et al., 2012, Pandya et al., 2017, Monga et al., 2014, Ethiraj et al., 2013, Kendre and Baseer, 2013, Hassan, 2011, Fazaeli et al., 2010), as shown in Scheme 1.

Beyhan et al. reported a different method for the synthesis of pyrazoline compounds from the reaction of chalcones (prepared from methyl aryl ketones with substituted aldehydes) with thiosemicarbazide and N-(4-chlorophenyl) semicarbazide in alkaline medium (Beyhan et al., 2017). Another method for the synthesis of pyrazoline is through the reaction of substituted hydrazonoyl and N-phenylmaleimide in good yield (Abdelhamid et al., 2000), Scheme 2.

The kinetic studies of pyrazoline formation from reaction of different chalcones with different compounds such as Schiff base, hydrazine, and thiourea in dimethylformamide and dimethylsulfoxide (DMSO) have been measured spectrophotometerically. The reaction is first order with respect to each reactant undergoes one or two steps to produce pyrazolines or pyrimidine thiones (Al-Khayat, 2010, Kaka et al., 2016). The kinetics of the reaction for the substituted chalcones have been also studied and found first-order reaction (Upadhyay, 2007).

ARO-The Scientific Journal of Koya University
Volume VII, No.2(2019), Article ID: ARO.10508, 9 pages
DOI: 10.14500/aro.10508
Received 06 March 2019; Accepted: 18 August 2019
Regular research paper: Published 10 December 2019
Corresponding author's e-mail: Kosrat.nazad@koyauniversity.org

 http://dx.doi.org/10.14500/aro.10508

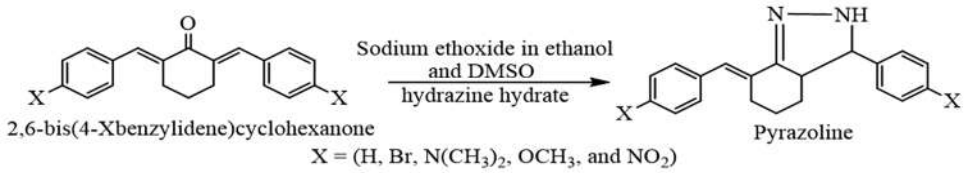

Scheme 1. Reaction pathway.

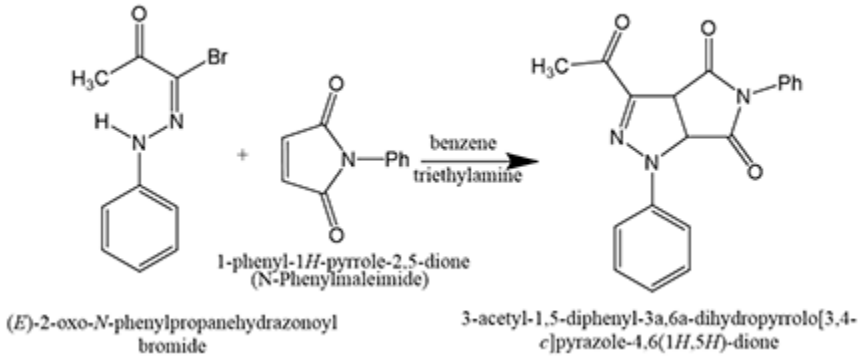

Scheme 2. Pyrazoine synthesis.

The present study is concerned with the kinetics of our synthesized pyrazolines and its derivatives. The effect of the electron configuration of substituents in para position of chalcones on the rate of chemical reaction and on the stability of activated compounds is studied. Moreover, the suitable mechanism for the reaction was suggested. Finally, the compensation effects for the substituent were observed and showed the expected routes.

II. Experimental

The infrared (IR) spectra (KBr, υ cm^{-1}) for the synthesized compounds were measured using (Fourier-transform- IR [FT-IR]) spectrophotometer, and the ultraviolet (UV)-visible spectra were estimated by Agilent Cary-100 (UV-visible Spectrophotometer). Nuclear magnetic resonance (NMR) spectra were showed on BRUKER 500.133 MHz spectrometer (UK) using DMSO as a solvent.

A. General Procedure

Synthesis of (E)-7-benzylidene-3-phenyl-3,3a,4,5,6,7-hexahydro-2H-indazole-2-carbothioamide and its derivatives:

Compound (A), X= H
Compound (B), X=N(CH_3)$_2$
Compound (C), X=NO_2

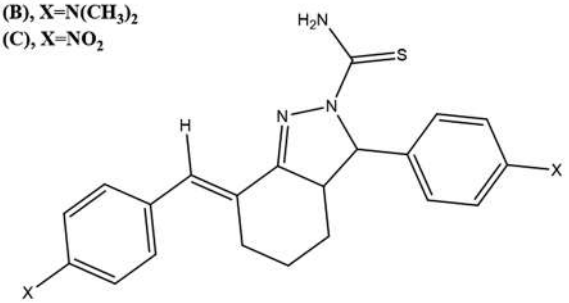

Thiosemicarbazide (4-mole eq.) was dissolved in absolute ethanol containing (10% sodium ethoxide). It was then added to a stirred solution of 1-mole equation of 2, 6-dibenzylidenecyclohexanone (Chalcone) or equivalent to one of its derivatives dissolved in 5 ml DMSO. The reaction mixture was stirred for 24 h at room temperature and refluxed for another 24 h. The reaction mixture was then cooled and poured into 10 ml of ice water. The product was precipitated, washed twice with cold water to give the crude product, it was purified by recrystallization from ethanol to give pure product (A, B, and C), (67%, 63%, and 77% yield), respectively.

For the purpose of kinetic study, the Agilent Cary-100 UV-visible spectrophotometer was used for scanning wavelength against absorbance to follow-up the absorbance change of the reactions at fixed wavelength. The spectrophotometer was supplied with the quartz cuvette type (Q) supported with Teflon quick fit stopper used for holding sample at constant temperature. The reaction temperature was controlled using an automatic thermostat type (Cary temperature controller) attached with circulating built-in pump to ensure a constant speed of circulating water. The supply company insulated all pipe connections properly so that temperature deviation inside the reaction cuvette was varied within the limits of ±0.01°C.

The rate of the reaction was determined by reaction between thiosemicarbazide and chalcones (A, B, and C) in DMSO and basic medium (sodium ethoxide) using absolute ethanol as a solvent.

For the purpose of zeroing at λ_{max} (259.00) nm, chalcone (0.002 mmol/l, 1 mL), sodium ethoxide 10% (1 mL), and 0.5 mL of each of the DMSO, ethanol solvents were mixed in quartz cell for both of the reaction and blank readings.

To study the reaction kinetic, thiosemicarbazide (0.0001 mmol/l, 1mL) was added to the reaction cell, and

ethanol (1 mL) was added to the blank cell to reach the volume completion. The absorbance was monitored at different temperature. The decrease in the absorbance of thiosemicarbazide at λ_{max} (259.00) nm in DMSO was occurred at different temperatures. The color changed from pale yellow to colorless gradually, due to the gradual consuming the thiosemicarbazide gradually, and converting to product.

The rates constant was evaluated by fitting the absorbance – time data to the appropriate pseudo first-order rate Equation-1 using linear regression program:

$$\ln (\Lambda_o - \Lambda_\infty)/(\Lambda_t - \Lambda_\infty) = k_{obs.}\, t \quad (1)$$

Where:

Λ_o=Absorbance of the thiosemicarbazide at time zero.

Λ_t=Absorbance of the thiosemicarbazide at different time.

Λ_∞=Absorbance of the thiosemicarbazide after reaction complete (when the absorbance became constant).

$k_{obs.}$ = The rate constant for the pseudo first-order of the reaction.

$k_{obs.} = k\,[\text{Thiosemicarbazide}]^n$; n=Order of the thiosemicarbazide as a pseudo first-order.

III. Results and Discussion

Compounds [A, B, and C] were synthesized by the reaction of 1 mole equivalent of chalcones (Kaka, 2017) with 4 mole equivalents of thiosemicarbazide in DMSO and basic medium (sodium ethoxide) using absolute ethanol as a solvent, as shown in Scheme 3.

TABLE I
The IR Spectrum Assignment of the Compounds (A, B, and C)

Compound	N-$H_{str.}$ υ/cm^{-1}(m)	C=$N_{str.}$ υcm^{-1}(w)	N-$H_{bend.}$ υcm^{-1}(w)	C=$C_{str.}$ Aromatic υcm^{-1}(m)	N-H wag υ/cm^{-1}(m)
A	3338, 3279	1650	1638	1625	748
B	3408, 33371	1694	1678	1603	770
C	3380, 33359	1659	1635	1597	769

The structure of synthesized compounds was confirmed through a combination of various spectroscopic techniques including IR, UV-visible spectrophotometer, ^{1}H-NMR, and^{13}C NMR spectra. The IR spectrum for the compound (A) showed two clear bands at 3338 and 3279 cm^{-1} corresponding to primary NH_2 group, and a band at 1650 cm^{-1} which was corresponded to the C=N stretching vibration. The C=C group band was appeared at 1625 cm^{-1}, whereas the N-H bending vibration appeared near 1638 cm^{-1}. The total characterization of IR bands for the compounds (A, B, and C) is shown in Table I.

The proton and carbon NMR of the compound (A, B, and C) is characterized in Table II.

The total characterization of proton and carbon NMR for the compounds (A) and its spectra is shown in the following pictorial Fig. 1.

Below ^{1}H-NMR and ^{13}C-NMR spectrum belongs to compound (A) Fig. 1:

In this study, the kinetic study of the formation of new pyrazoline compounds was conducted using UV-Visible spectroscopy by following the decrease in the absorbance of thiosemicarbazide (λ_{max} 259.00 nm). The band of the used thiosemicarbazide did not interfere with other spectral bands of chalcone and the product (pyrazoline). The decrease in absorbance of thiosemicarbazide is exactly equivalent to the remaining concentration of the reactant. Ethanol and DMSO were found to be suitable solvents for all the kinetic measurements. The reaction was found to be slow. Preliminary, attempts were made to find suitable concentration range of thiosemicarbazide, which obeys Beer's-Lambert law. A ratio of concentrations of (1:20) thiosemicarbazide: chalcones (or its derivatives) was found to be adequate and used in all our measurements. Table V shows λ_{max} of substituted thiosemicarbazide and chalcones, and the valid range of Beer-Lambert law. At first, a full scan of the reaction spectrum (between thiosemicarbazide and three different chalcones separately) was performed to

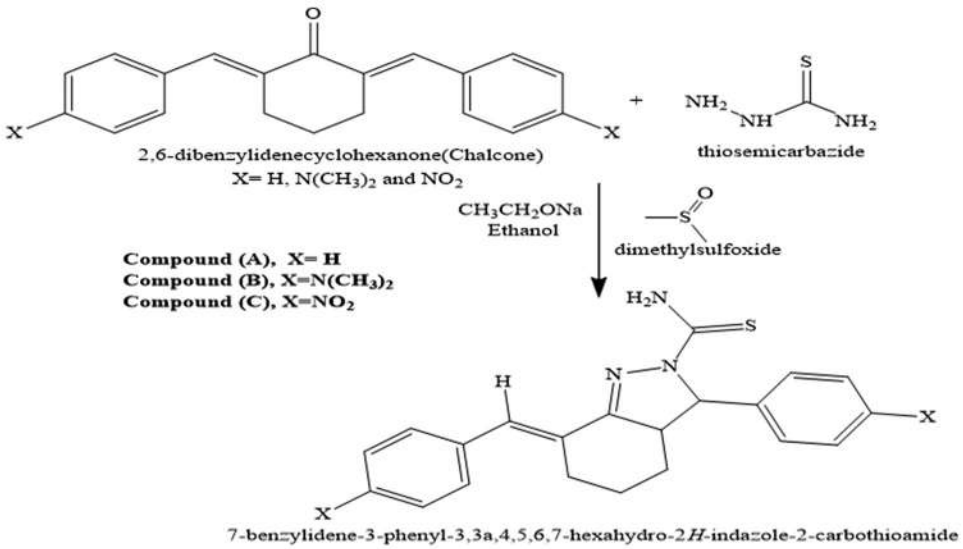

Scheme 3. Reaction pathway of pyrazoline synthesis.

 http://dx.doi.org/10.14500/aro.10508

TABLE II
^{1}H-NMR Chemical Shift Assignment in PPM of the Compounds(A, B, and C)

Comp.	X	Chemical shifts in PPM
A	-H	9.31 (2H, br.s, NH_2), 7.49–7.26 (8H, m, Ar-H), 6.35 (1H, m, CH=C), 3.92(1H, d, CH-N), 2.46–2.45 (1H, m, CH-C=N), 2.27–2.23 (2H, m, CH-C=CH), 1.37–1.33 (4H, m, CH_2-CH_2).
B	-N$(CH_3)_2$	9.29 (2H, br.s, NH_2), 7.54–6.60 (8H, m, Ar-H), 6.30 (1H, m, CH=C), 3.94(1H, d, CH-N), 2.94 (12H, s, N $(CH_3)_2$, 2.48–2.45 (1H, m, CH-C=N), 2.24–2.22 (2H, m, CH-C=CH), 1.39–1.30 (4H, m, CH_2-CH_2),
C	-NO_2	9.26 (2H, br.s, NH_2), 8.16–7.56 (8H, m, Ar-H), 6.44 (1H, m, CH=C), 3.96(1H, d, CH-N), 2.51–2.49 (1H, m, CH-C=N), 2.31–2.26 (2H, m, CH-C=CH), 1.37–1.33 (4H, m, CH_2-CH_2),

TABLE III
^{1}H-NMR for Compound (A)

Proton	PPM	Multiplicity	Integration
$H_{12, 13, 15, 16, 17, 18, 20, and 21}$	7.49–7.26	d	8
H_{23}	6.35	s	1
H_2	2.27–2.23	m	2
H_3	1.37–1.33	m	2
H_4	1.37–1.33	m	2
H_5	2.45	m	1
H_8	3.92	d	1
H_{26}	9.31	br. s	2

TABLE IV
^{13}C-NMR for Compound (A)

Carbon	PPM
$C_{12, 13, 15, 16, 17, 18, 20, 21, and 23}$	141.6, 135.6, 130.3, 128.2, 124.3
C_2	28.0
C_3	25.1
C_4	24.3
C_5	43.6
C_8	78.5
C_{24}	177.1

TABLE V
Maximum Absorption of Chalcones and Pyrazolines in Dimethylsulfoxide

λ_{max} of pyrazoline	Pyrazoline	λ_{max} of chalcone	Compounds
344	A	350	Chalcone (p-H)
349	B	448	Chalcone (p-N $(CH_3)_2$)
330	C	337	Chalcone (p-NO_2)

choose a suitable wavelength for kinetic measurements, as shown in Fig. 2.

As we mentioned in the experimental part, after a 24 h of stirring and mixing of the reactants (thiosemicarbazide, sodium ethoxide, chalcone, and its derivatives) in DMSO, an appropriate absorption band of pyrazoline-H and its derivatives was built up systematically in the 344.00 nm.

The figure below shows the decreases in absorbance of the thiosemicarbazide with no interference either with reactant or product or with no side reactions.

The rate of the disappearance of thiosemicarbazide is found to be sensitive to the temperature change in the range between 298.15 K and 318.15 K. Therefore, the runs were carried out within this range of temperature.

In earlier study, theoretically, kinetic measurements of any bimolecular reaction are found totally second-order when 1:1 mixing mole ratio was used, which means first-order for each of reactants (Kaka, 2017).

Practically, the reaction showed first-order reaction for thiosemicarbazide, Equation 2.

To simplify our kinetic investigations and mathematical treatments of data, a pseudo first-order reaction was followed using large excess of chalcones (20-fold) compared to thiosemicarbazide concentration. In this case, the rate of reaction became:

$$r = k_{obs.}\,[\text{Thiosemicarbazide}] \quad (2)$$

Where $k_{obs.} = k\,[\text{Chalcones}]^1$, in this case, the thiosemicarbazide was found to be pseudo first-order of reaction. Plots of $\ln\frac{A_o - A_\infty}{A_t - A_\infty}$ versus time were always straight lines with slope that corresponds to $k_{obs.}$

The above Equation (1) was applied for a mixture of thiosemicarbazide concentration of 2×10^{-4} M and large amount of chalcones (20-fold) (0.004 M) for all of the reactions under study and lead to reasonable reaction rates even at different temperatures. Many runs were performed at different temperatures, and the measurements were always followed toward the completion of reaction. Typical plots show excellent fit to Equation (1) and were always linear, as shown in Fig. 3. Thus, the assumption of pseudo first-order reaction was fully proven.

The observed rate constant was calculated from the slope of the Equation (1). The standard deviation of the slope represented reasonable value of estimated rate constant (K).

Plots of ln k_{obs} using data listed in Tables VI-VII versus the reciprocal absolute temperature between 298.15 and 318.15 K were drawn and found acceptable straight lines. The least-square method was used for plotting Arrhenius equations, and treating the mean rates constants at each temperature as a single point with a unit of weight.

The entropies of activation also gave good evidence about the shape of the activated complex and about the mechanistic pathway. The $\Delta S^{\#}$ is estimated from the A-Factor, at 308.15 K, according to the following Equation (3).

$$\Delta S^{\#} = R \times \ln A/((e^2 kT)/h) \quad (3)$$

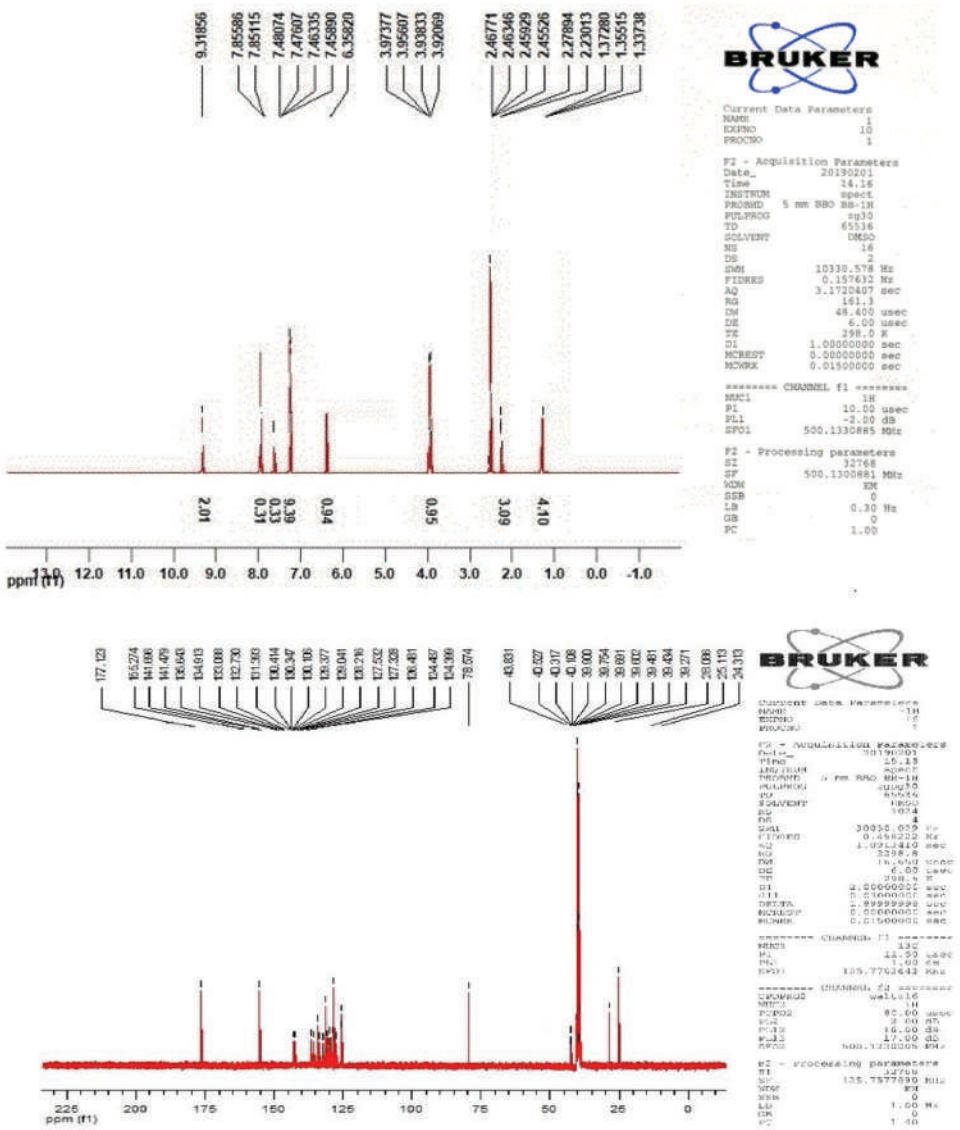

Fig. 1. ^{1}H, ^{13}C-NMR spectrum for compound (A).

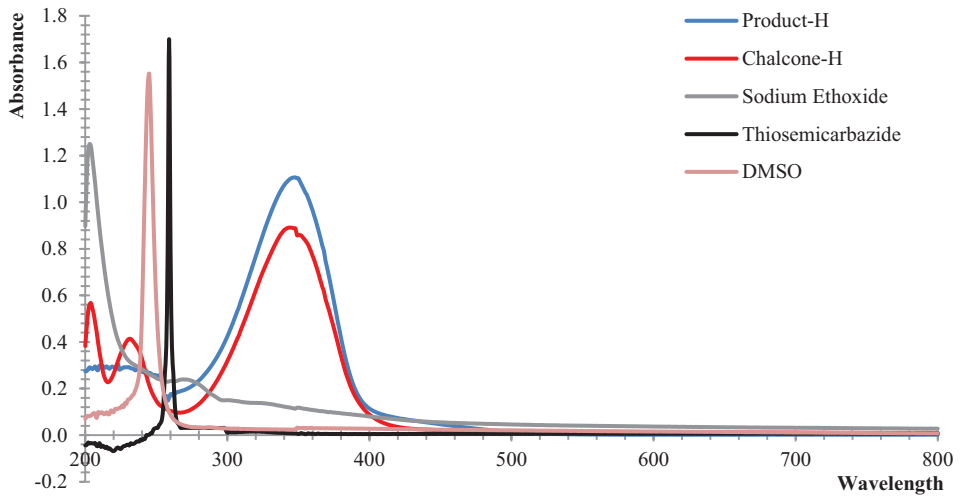

Fig. 2. Ultraviolet-visible spectrum for thiosemicarbazide, chalcones-H, sodium ethoxide, and product pyrazoline-H in dimethylsulfoxide (each one alone).

http://dx.doi.org/10.14500/aro.10508

A factor was calculated according to Arrhenius equation, as shown in Fig. 4, the intercept is Ln A.

ΔS# = Entropy of activation (J mol^{-1} K^{-1}), R = Gas constant (8.314 J/mol. K).

A = Arrhenius factor was calculated from Intercept of Arrhenius equation K = A e–E/RT. ((time)-1(Conc.)1-n) n=order of reaction, e= 2.72, K = 1.38*10−23 m^2 kg/s-2K-1, T=Absolute temperature (K), h=6.62*10–34 m^2 kg/s.

The effect of substituted chalcones on the rate of the condensation process was studied. In the inspection of the effect of the electron-donating groups (-$N(CH_3)_2$), we have noticed that these groups increase the electron density at the β-carbon of the C=C of the chalcone (the reaction center), by conjugation. This can cause the reducing in the rate of reaction compared with the unsubstituted parent analogous. On the other hand, the electron withdrawing groups (-NO_2) decrease the availability of electrons at the β- carbon of the (C=C) of the chalcone by conjugation, results in strengthening the attractive forces between reactants and enhancing the reaction rate. The difference in rates of reaction was found to be in the following order

$$\underline{p\text{-}NO_2\text{-}p\text{-}H\text{-}p\text{-}N(CH_3)_2}$$

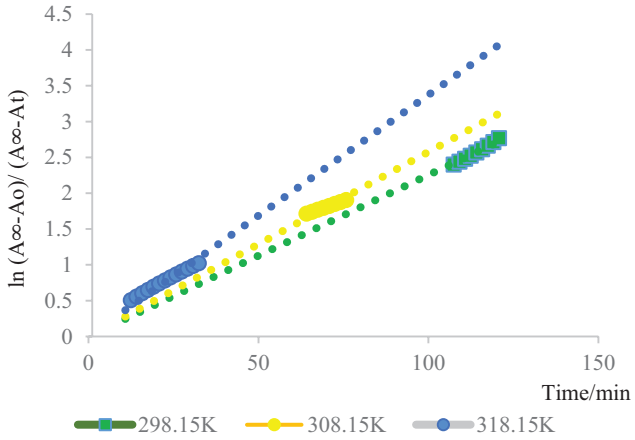

Fig. 3. Pseudo first-order plot for the reaction of chalcone-H with thiosemicarbazide (using sodium ethoxide) in dimethylsulfoxide at different temperatures.

Moving from left to right, the rate of the reaction increase of the observed reaction rates is shown in Fig. 5 and Tables VI-VII.

The values of activation parameters are of great importance to describe the mechanism under all circumstances studied here. The energies of activation for all reactants are generally small in value and vary within (26.897–4.781) KJ/mol. The variation of their values may be attributed to the electron-donating or withdrawing capabilities of the attacked groups.

Other important factors that control the reaction rate are the A-Factor and it $\Delta S^{\#}$. These two factors are related to each other by the Equation (3), which is derived from the transition state theory (Ceylan and Gezegen, 2008). Using the above equation a value A ≅ $10^{13.5}$ s^{-1} corresponds to $\Delta S^{\#}$=0. The decrease in this value results in a negative entropies of activation. It is noticed that all of A-factors obtained for all the reactions under study are less than the above-mentioned value and correspondingly all the obtained $\Delta S^{\#}$ values are negative.

The negative values of the $\Delta S^{\#}$ of the reaction of all chalcones with thiosemicarbazide are shown in Tables VI-VII, indicate the formation of a restricted intermediate which suffers from lack of center degrees of freedom as compared to the reactants. The decrease in the value of A-factor provides an important indication about the stability of the intermediate and hence gives good support for explaining the reason for the differences in the value of rate constants. Since the decrease in the values of both A-factor and $\Delta S^{\#}$ leads to the same target. From these investigations, it can be concluded that the reaction of the chalcone with the thiosemicarbazide nucleophile proceeds through the formation of transition state in a relatively slow step. The rate constant values, the A-parameters values, the Gibbs free energy of activation (the reactions have the same mechanism route, as shown in Tables VI-VII), as well as the negative values of activation entropies are quite in agreement with the suggested mechanistic route. The reaction takes place according to Claisen route rather than Michael route depending on IR spectral data, which showed no

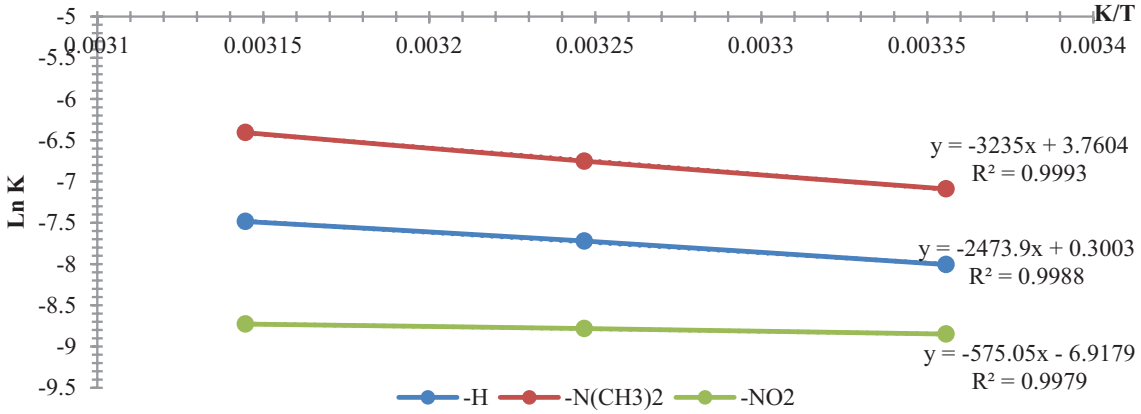

Fig. 4. Arrhenius plots for the reaction of compounds chalcones (-H, -$N(CH_3)_2$ and –NO_2) with thiosemicarbazide in dimethylsulfoxide as a solvent.

peaks of N-H stretching of pyrazoline ring. In addition of that, ChemOffice 3D program theoretical calculations found that the heat of formation (H. F.) of unsubstituted Claisen product equal to 131.8 kcal/mol which is less than Michael product equal to 228.8 kcal/mol. This means the reaction goes through Claisen route because has less value of heat of formation. The mechanism of the reaction is shown in Scheme 5.

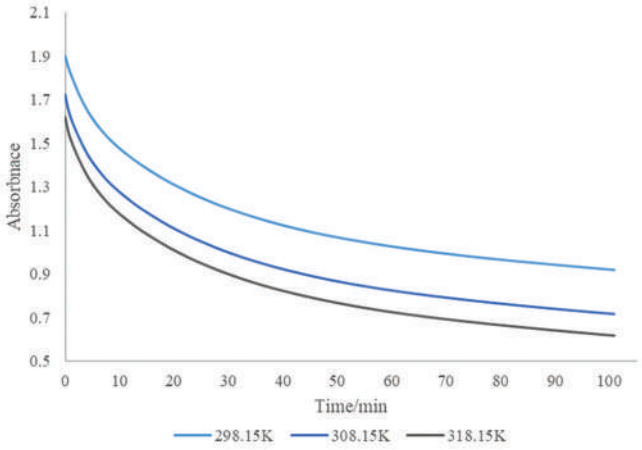

Fig. 5. Decrease in the concentration of thiosemicarbazide at different times and temperatures.

The kinetic study of the pyrazoline compounds (A, B, and C) cannot fully explain the reaction mechanism; therefore, organic chemistry facts must be applied in combination with kinetic calculations.

To understand the certain mechanism of formation of all of the pyrazoline compounds (A, B, and C), true compensation effect was applied. It was noted that the compensation effect was a straight line for all substituent as shown in Fig. 6, which means all of the pyrazoline compounds (A, B, and C) forms according to the same route of mechanism. Moreover, the compensation effect also confirmed no effect of used solvents on the route of the mechanism (Fig. 6).

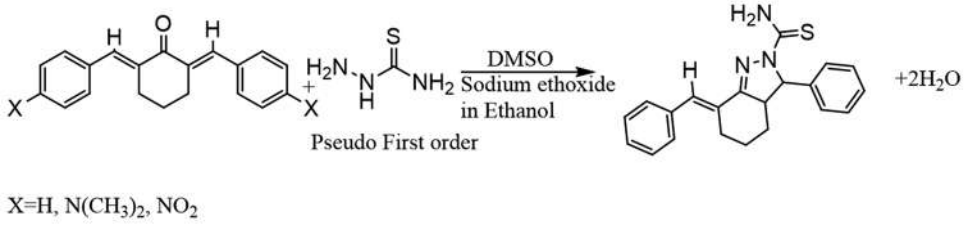

Scheme 4. Reaction pathway of payrazoline.

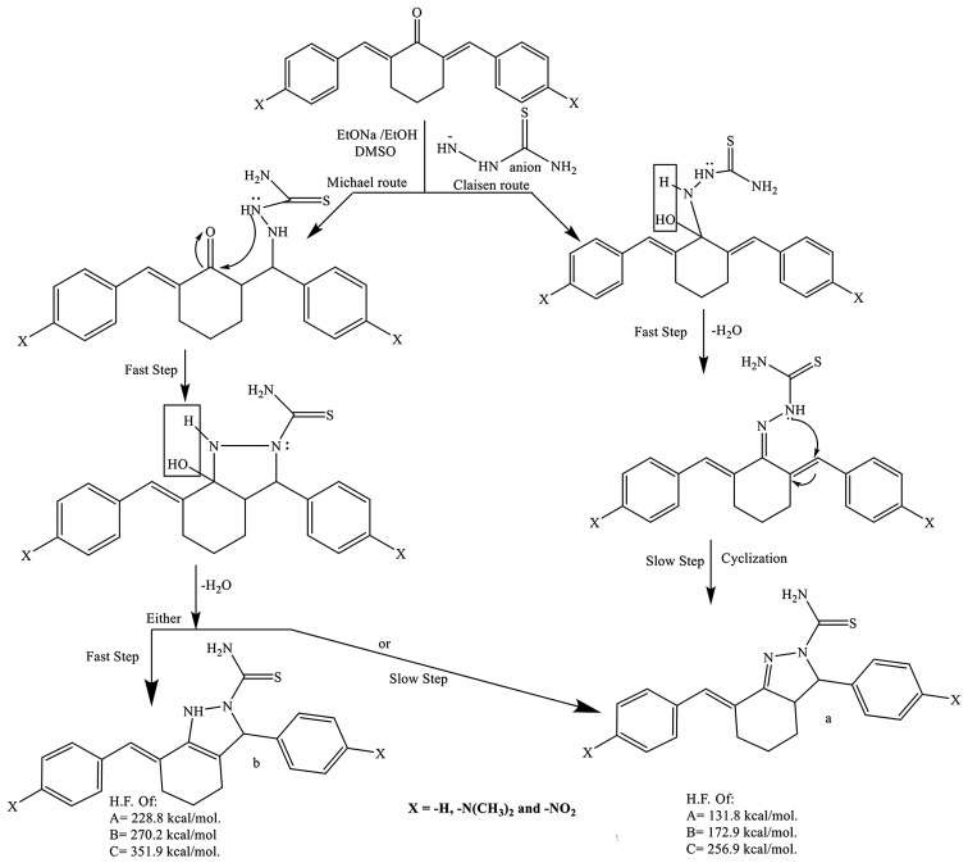

Scheme 5. Proposed reaction mechanism.

 http://dx.doi.org/10.14500/aro.10508

TABLE VI
OBSERVED RATE CONSTANTS, FOR THE REACTION CHALCONE-H WITH THIOSEMICARBAZIDE, OBTAINED FROM KINETIC PLOTS AT DIFFERENT

T/K	K (s)/10^4 s^{-1}	t ½/10^{-2} s	E/KJmol^{-1}	$\Delta S^{\#}$/JK^{-1} mol^{-1}	$\Delta G^{\#}$/KJ mol^{-1}	A/10^{-4}	R^2	SD/10^4
298.15	1.435	48.293	4.781	−311.019	100.621	9.899	0.9885	0.038
308.15	1.535	45.147					0.9900	0.058
318.15	1.620	42.778					0.9900	0.078

TABLE VII
OBSERVED RATE CONSTANTS, FOR THE REACTION CHALCONE-N $(CH_3)_2$ WITH THIOSEMICARBAZIDE, OBTAINED FROM KINETIC PLOTS AT DIFFERENT TEMPERATURES

T/K	K (s)/10^4 s^{-1}	t ½/10^{-2} s	E/KJ mol^{-1}	$\Delta S^{\#}$/JK^{-1} mol^{-1}	$\Delta G^{\#}$/KJ mol^{-1}	A/s^{-1}	R^2	SD/10^4
298.15	3.333	20.790	20.568	-251.007	97.916	1.350	0.9911	0.053
308.15	4.433	15.632					0.9800	0.025
318.15	5.622	12.338					0.9900	0.044

TABLE VIII
OBSERVED RATE CONSTANTS, FOR THE REACTION CHALCONE-NO_2 WITH THIOSEMICARBAZIDE, OBTAINED FROM KINETIC PLOTS AT DIFFERENT

T/K	K (s)/10^4 s^{-1}	t ½/10^{-2} s	E/KJ mol^{-1}	$\Delta S^{\#}$/JK^{-1} mol^{-1}	$\Delta G^{\#}$/kJ mol^{-1}	A/10^1 s^{-1}	R^2	SD/10^4
298.15	8.330	8.316	26.897	−222.240	95.379	4.297	0.9993	0.017
308.15	11.670	5.940					0.9940	0.089
318.15	16.500	4.200					0.9911	0.048

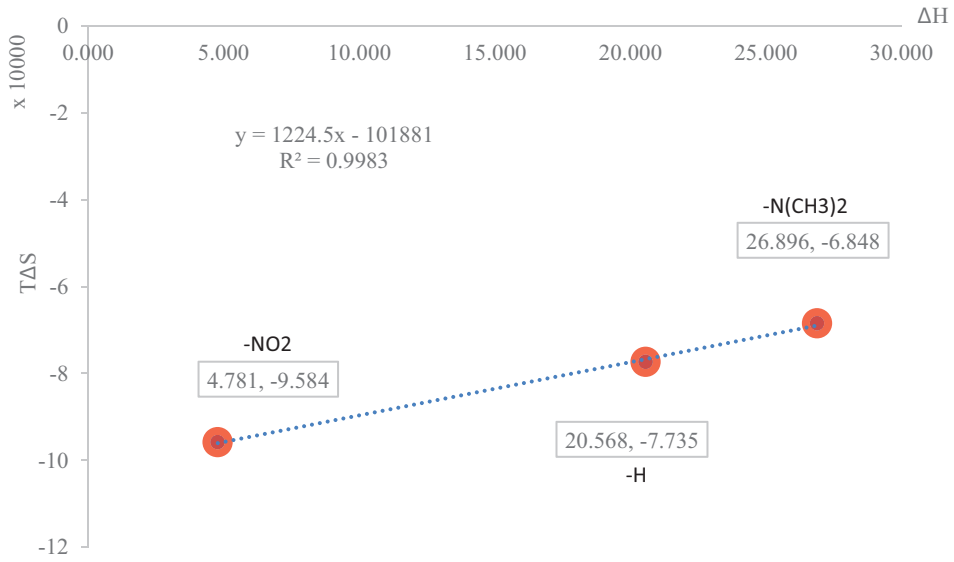

Fig. 6. Compensation effect for the (A, B, and C) compounds.

IV. CONCLUSIONS

A series of novel pyrazoline compounds (A, B, and C) were synthesized successfully and fully characterized using UV-Vis, ^{1}H-NMR, ^{13}C-NMR, and FT-IR spectroscopy. The kinetic study showed first-order reaction of thiosemicarbazide with chalcones to form pyrazoline compounds (A, B, and C). The substituents affected the rate of the reaction according to the following sequence. The highest rate of the reaction is found for the electron-donating group ($N(CH_3)_2$, and the lowest for the electron withdrawing group (NO_2).

$$\underline{p\text{-}NO_2\text{-}p\text{-}H\text{-}p\text{-}N(CH_3)_2}$$

It is also concluded that the low values of Arrhenius factor and correspondingly the negative values of $\Delta S^{\#}$ activation provided support to the restricted transition state, which is, demand some degrees of freedom in slow step of the reaction.

The relative constancy of $\Delta G^{\#}$ of activation values and compensation effect indicated that the reaction of all the substituted chalcones and its derivatives have the same reaction mechanism (Kaka, 2017), it is proposed that the reaction takes place according to Claisen route rather than Michael route based on IR spectral data, which showed no peaks of N-H stretching of pyrazoline ring which is expected to appear if the reaction goes through Michael route. Moreover, the heat of formation of Claisen product is less than Michael product based on ChemOffice 3D program calculations.

V. Acknowledgment

We are greatly indebted to Koya University, Faculty of Science and Health, Chemistry Department, for many helps and providing facilities that made this work possible.

References

Abdelhamid, A., Zohdi, H., Sallam, M., and Ahmed, N. 2000. Reactions with hydrazonoyl halides. 31. Synthesis of some new pyrrolidino [3, 4-c] pyrazolines, pyrazoles, and pyrazolo [3, 4-d] pyridazines. *Molecules,* 5, pp.967-973.

AL-Khayat, R.Z. 2010. *PhD Thesis.* University of Mosul.

Beyhan, N., Kocyigit-Kaymakcioglu, B., Gümrü, S., and Aricioglu, F. 2017. Synthesis and anticonvulsant activity of some 2-pyrazolines derived from chalcones. *Arabian Journal of Chemistry,* 10, pp.S2073-S2081.

Carey, F. 1996. *Organic chemistry*. McGraw-Hill, New York, p.749.

Ceylan, M., and Gezegen, H. 2008. Preparation of 1, 5-diketones by addition of cyclohexanone to chalcones under solvent-free phase transfer catalyst condition. *Turkish Journal of Chemistry*, 32, pp.55-61.

Ebenezer, W., and Wight, P. 1995. In: Katrizky, A.R., Meth-Cohn, O., and Ress, C.W., editors. *Comprehensive organic function group transfoamation*. Vol. 3. Pergmon Press, Oxford, p.206.

Esmaeel, D.M.T. 1988. *Organic chemistry*. Directors are Publishing Houses, Mosul.

Ethiraj, K., Nithya, P., Krishnakumar, V., Mathew, A.J., and Khan, F.N. 2013. Synthesis and cytotoxicity study of pyrazoline derivatives of methoxy substituted naphthyl chalcones. *Research on Chemical Intermediates*, 39, pp.1833-1841.

Fazaeli, R., Aliyan, H., Bordbar, M., and Mohammadi, E. 2010. H3PW12O40: Highly efficient catalysts for the synthesis of novel 1, 3, 5-triaryl-2-pyrazoline derivatives. *Open Catalysis Journal*, 3, pp.79-82.

Gutsche, C.D. 1967. *Chemistry of carbonyl compounds*. Prentice-Hall, New Jersey.

Hamad, W.M., Kaka, K.N. Al-Hamadany, A.J., and Dabbagh, A.M. 2016. Synthesis and spectral characterization of some fused pyrimidine thiones. *Journal Of Raparin University*, 3**,** p.87.

Hassan, S.Y. 2011. Synthesis and biological activity of some new pyrazoline and pyrimidine derivatives. *Journal of the Brazilian Chemical Society*, 22**,** pp.1286-1298.

Joshi, V.D., Kshirsagar, M.D., and Sarita, S. 2012. Synthesis and antimicrobial activities of various pyrazolines from chalcones. *International Journal of ChemTech Research*, 4**,** pp.971-975.

Kaka, K., Dabbagh, A., and Hamad, W. 2016. Kinetics Study of the Formation of Pyrmidine Thione from the Reaction of 2, 6-Dibenzylidinecyclohexanone and its derivatives with Thiourea. *ARO The Scientific Journal of Koya University*, 4**,** pp.37-42.

Kaka, K.N. 2017. Kinetics and Mechanistics Studies on the Formation of 2,6-dibenzylidinecyclohexanones and their Reactions with Bromine, Hydrazine and Thiourea. *Ph.D*, Mosul.

Kendre, M., and Baseer, M. 2013. Synthesis and evaluation of some new pyrazoline derivatives as antimicrobial agents. *Oriental Journal Chemistry*, 29, pp.253-256.

Lévai, A. 2005. Synthesis of chlorinated 3, 5-diaryl-2-pyrazolines by the reaction of chlorochalcones with hydrazines. *Arkivoc*, 9, pp.344-352.

Li, J.T., Zhang, X.H., and Lin, Z.P. 2007. An improved synthesis of 1, 3, 5-triaryl-2-pyrazolines in acetic acid aqueous solution under ultrasound irradiation. *Beilstein Journal of Organic Chemistry*, 3, p.13.

Mccrae, W. 1973. *Basic organic reactions*. Heyden and Son Ltd., London.

Monga, V., Goyal, K., Steindel, M., Malhotra, M., Rajani, D.P., and Rajani, S.D. 2014. Synthesis and evaluation of new chalcones, derived pyrazoline and cyclohexenone derivatives as potent antimicrobial, antitubercular and antileishmanial agents. *Medicinal Chemistry Research*, 23, pp.2019-2032.

Pandya, M., Kapadiya, K., Pandit, C., and Purohit, D. 2017. Synthesis of halogenated chalcones, pyrazolines and microbial evaluation of derived scaffolds. *Journal of Scientific and Industrial Research*, 76, pp.173-178.

Patel, M., Dodiya, B., Ghetiya, R., Joshi, K., Vekariya, P., Bapodara, A., and Joshi, H. 2011. Synthesis and antimicrobial evaluation of pyrazoline derivatives. *International Journal ChemTech Research*, 3, pp.967-974.

Powers, D.G., Casebier, D.S., Fokas, D., Ryan, W.J., Troth, J.R., and Coffen, D.L. 1998. Automated parallel synthesis of chalcone-based screening libraries. *Tetrahedron*, 54, pp.4085-4096.

Qiu, H., Sarkar, S.M., Lee, D.H., and Jin, M.J. 2008. Highly effective silica gel-supported N-heterocyclic carbene Pd catalyst for suzuki miyaura coupling reaction. *Green Chemistry*, 10, pp.37-40.

Ramage, G., Rodd, E., and Landquist, J. 1957. XVI. *Chemistry of carbon compounds. IVC, heterocyclic compounds*. Elsevier, New York.

Sloop, J.C., Lechner, B., Washington, G., Bumgardner, C.L., Loehle, W.D., and Creasy, W. 2008. Pyrazole formation: Examination of kinetics, substituent effects, and mechanistic pathways. *International Journal of Chemical Kinetics*, 40, pp.370-383.

Upadhyay, S.K. 2007. *Chemical kinetics and reaction dynamics*. Springer Science and Business Media, Berlin.

http://dx.doi.org/10.14500/aro.10558

Electrical and Structural Properties of Copper Oxide Thin Films Deposited on Plastic Substrate by Spray Pyrolysis Technique

Mohammad G. Faraj, Askander K. Kaka and Halo D. Omar

Department of Physics, Faculty of Science and Health, Koya University, Koya KOY45, Kurdistan Region - F.R. Iraq

Abstract— **In this paper, copper oxide (CuO) thin films were deposited on polyimide plastic substrates by spray pyrolysis technique at different temperatures from 250 to 300°C. All the deposited films were characterized by X-ray diffraction (XRD) technique, ultraviolet (UV)-visible spectrophotometer, and hall effect measurements for the investigation of structural, optical, and electrical properties. The effects of substrate temperature on the structural, optical, and electrical properties of the films were studied. The XRD results revealed that all the CuO films have a face-centered cubic structure. The crystallite grain size was calculated using Scherrer formula and it was found that at the substrate temperature of 300°C, the CuO film presented maximum crystallite grain size of about 81.2 nm. The root mean square (RMS) roughness of the films was measured by scanning tunneling microscopy. RMS was increased with the rise of temperature. The optical transmission measurements by UV-visible spectrophotometer were used to determine the energy gap of the CuO films. Results showed that the optical energy gap has decreased with increasing the substrate temperature. Hall effect measurements showed that all the films are of p-type conductivity. Depending on the substrate temperature, hall measurement showed that the electrical resistivity and carrier concentration are varied from 77.4 Ω cm to 52.7 Ω cm and from 6.3×10^{15} cm^{-3} to 10.1×10^{15} cm^{-3}, respectively.**

Index Terms — **Copper oxide, Chemical spray pyrolysis, Thin film, Polyimide.**

I. Introduction

Copper oxide (CuO) is an important semiconductor material due to their important applications in many technological fields such as gas sensors (Mariammal, et al., 2013; Hubner, et al., 2011) and solar cells (Chandrasekaran, 2013; Amri, et al., 2013). This is due, first, to the low cost, the non-toxicity, and the availability of copper in nature, second to the simplicity of the deposition process of its components. CuO is a p-type semiconductor.

Regarding the preparation of CuO thin films, different physical and chemical deposition techniques are adopted, such as magnetron sputtering, spin coating, thermal evaporation, and shower pyrolysis (Dolai, et al., 2017; Nalbant, et al., 2013; Akkari, et al., 2007; Morales and Sanchez, 2005). Among the previously mentioned systems, splash pyrolysis is a promising technique because of its minimal effort nature and appropriateness for saving expansive zone thin-films (Faraj and Taboada, 2017).

Research on CuO testimony on adaptable polymeric substrates, for example, polyimide (PI) is gaining immense interests because of their adaptability, light-weight, minimal effort, high temperature opposition (regularly up to 400°C handling temperature), low coefficient of warm development coefficient of thermal expansion, low dampness take-up, and high dampness discharge qualities, its amazing electrical properties and furthermore expanded voltage perseverance (Faraj and Taboada, 2017; Faraj, et al., 2017). Because of its predominant properties, PI has discovered applications as substrates in adaptable thin-film sun oriented cells, adaptable printed circuits, and high thickness interconnects (Faraj and Pakhuruddin, 2015; Faraj, et al., 2017; Faraj and Omar, 2014).

A study has been reported on the characterization of CuO thin film on glass substrates with a spray pyrolysis technique (Chaudhary, et al., 2004). The novelty of the current work is to prepare and characterize thin film of CuO fabricated on PI plastic substrates.

In this paper, CuO thin films are prepared through chemical spray pyrolysis technique on PI plastic substrates at different substrate temperatures (250, 275, and 300°C). The influence of the substrate temperature on the structural, optical, and electrical properties of the CuO films is then studied.

II. Experimental Details

In this work, PI plastic substrates from DuPont corporation were used. Substrates were first cleaned using alcohol for 10 min to get rid of contamination, rinsed with deionized water, and dried with nitrogen gas. CuO thin films have been prepared on PI plastic substrates by chemical spray

ARO-The Scientific Journal of Koya University
Volume VII, No.2 (2019), Article ID: ARO.10558, 5 pages
DOI: 10.14500/aro.10558
Received 05 August 2019; Accepted 08 October 2019
Regular research paper: Published 10 December 2019
Corresponding author's e-mail: mohammad.ghaffar@koyauniversity.org

pyrolysis. The precursor solution was prepared by dissolving 0.1 M copper chloride ($CuCl_2.2H_2O$) in distilled water. To prepare 40 ml of the precursor solution the required quantity of salt is dissolved in double-distilled water. The substrate temperature was kept at different (250, 275, and 300°C) and the deposition time was fixed for 20 min.

The thickness of the film was optimized to be 500 nm. The film thickness was measured by the weighting method through a digital balance type (Meter AE-160) with sensitivity of 10^{-4} g, and the thickness was calculated according to the following equation (Ismail and Faraj, 2009).

$$t = \frac{\Delta m}{\rho . A} \quad (1)$$

Where, t is the thickness of the film, Δm is the mass of the film, ρ is the total density of the film, and A is the area of the film. The crystallographic structure of the prepared CuO thin films was determined using a high-resolution X-ray diffractometer (XRD) system (model: Panalytical empyrean) with CuKα radiation (λ) of 0.154 nm. The surface morphology of the CuO films was studied by scanning tunneling microscopy (STM) (model: NT-MDT Solver Nano). The optical properties of the films were characterized by a ultraviolet (UV)-visible spectrophotometer (model: UV-1240, Shimadzu). The hall measurement was implemented with HL5500PC system.

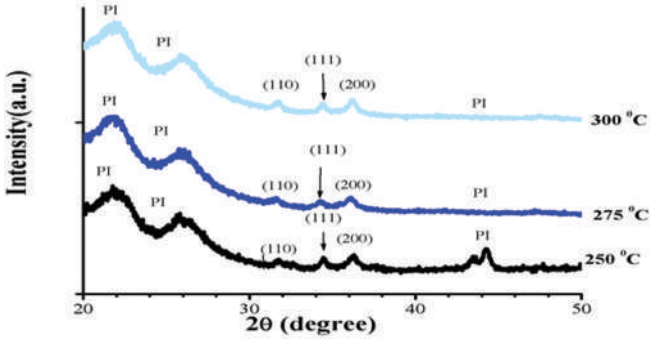

Fig. 1. X-ray diffraction patterns of copper oxide films on polyimide plastic at substrate temperatures of 250, 275, and 300°C.

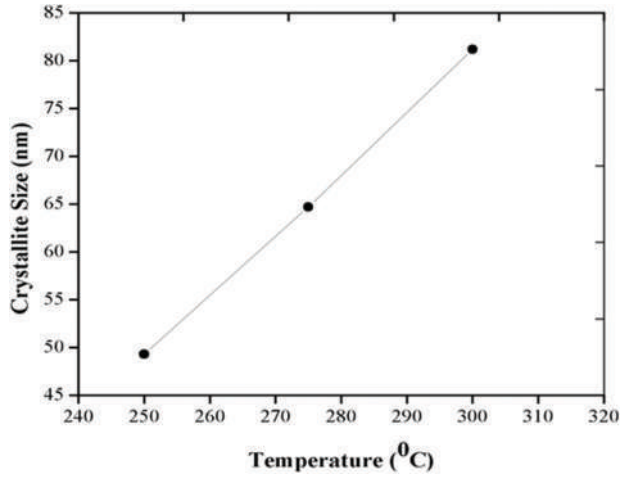

Fig. 2. Crystalline grain sizes as a function of substrate temperatures.

III. Results and Discussion

A. Structural Properties

Fig. 1 displays the patterns of XRD for the CuO thin films deposited on PI plastic for three different substrate temperatures. All CuO films have face-centered cubic structure (JCPDS card No.03-1005). The three pinnacles which have a place with the PI polymer are situated at 22.1°, 26.0°, and 44.6°, as shown in Fig. 1. This outcome concurs

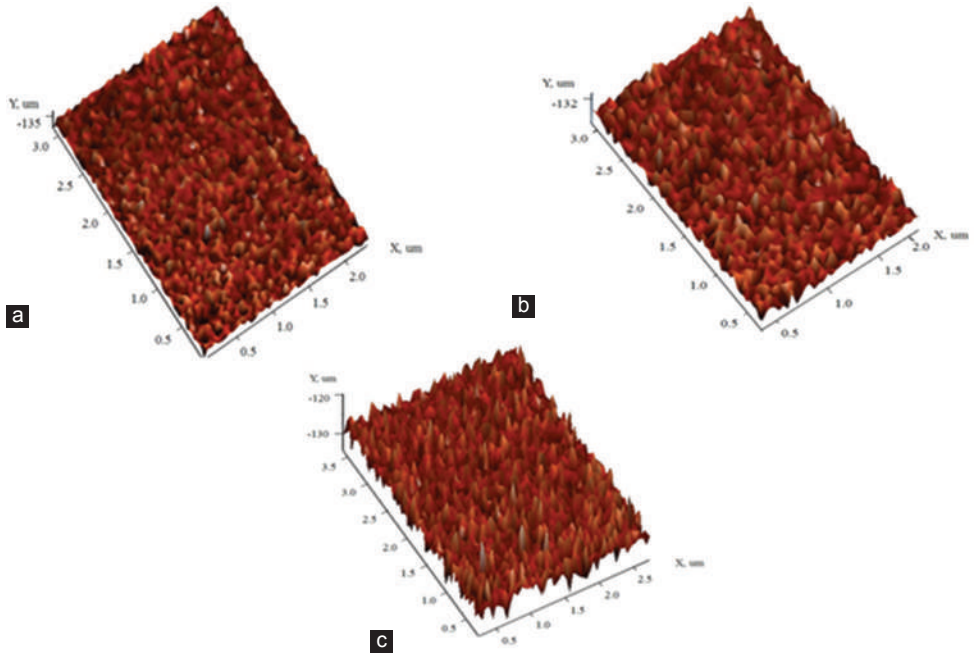

Fig. 3. Scanning tunneling microscopy images of copper oxide films deposited on polyimide substrate with different substrate temperatures (a) 250°C, (b) 275°C, and (c) 300°C.

with recently revealed information (Faraj, et al., 2014). XRD patterns of all the CuO thin films showed (110), (111), and (200) peaks planes corresponding to the face-centered cubic structure of CuO thin films. These XRD results confirm the proper phase formation of the CuO films.

The crystalline grain size (D) of the CuO films was determined with the Scherrer formula (Birks, 1946).

$$D = \frac{0.9\lambda}{\beta cos\theta} \quad (2)$$

Where β is the full width at half maximum (FWHM) of the peak, λ is the wavelength of the X-ray of 1.5406 Å, and θ is their peak position. Based on the line width of the (111) diffraction peak, the crystalline grain size for the CuO films with different substrate temperatures is shown in Fig. 2, where the grain size is increased with the increasing of substrate temperature, especially at 300°C. It was observed that the increase of the substrate temperature acts on increasing the diffraction peak intensity of (111) plane which resulted in an increase in crystallite size of the films. This behavior is a consequence of the decrease in density of nucleation centers as the substrate temperature increases. Under this condition, smaller numbers of nucleation centers start to grow, resulting in larger grains in agreement with previous reports using other deposition techniques (Abbas, et al., 2013).

STM images of CuO thin films deposited on PI plastic substrate are shown in Fig. 3. The root mean square (RMS) surface roughness of the films was 5.69, 8.28, and 10.78 for films at temperature in the range of 250–300°C at 25°C steps. It should be noted that the RMS surface roughness slightly increases with increasing substrate temperature (Haug, et al., 2001).

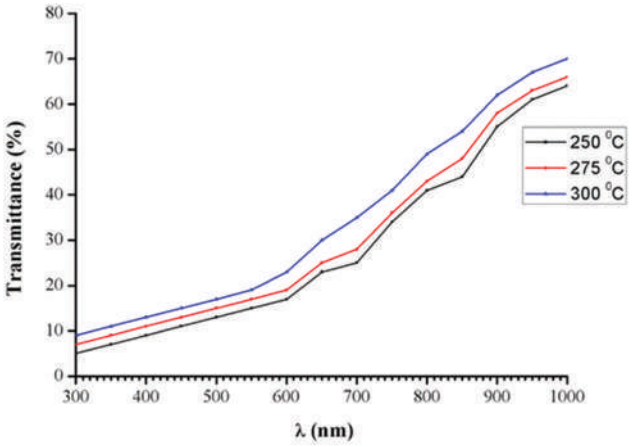

Fig. 4. Optical transmission spectra of copper oxide films deposited on polyimide substrate at different substrate temperatures.

B. Optical Properties

Fig. 4 shows the variation of the optical transmission as a function of wavelength from 300 mm to 1000 nm for the films deposited at different substrate temperatures. The transmission in the visible region is found to increase with increasing substrate temperature. An increase in substrate temperature improved the transmission of the CuO films. This improvement can be attributed to either the decrease in thickness or the improvement in perfection and stoichiometry of the films. Similar transmission profiles of CuO films have been previously reported (Hussein, et al., 2015).

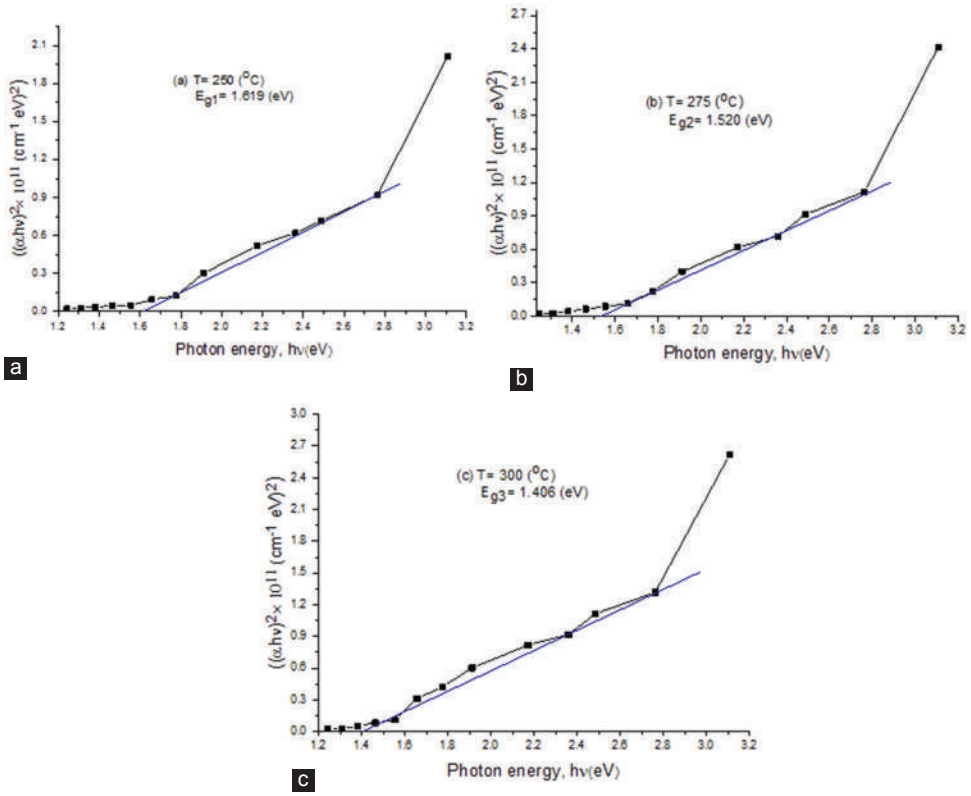

Fig. 5. (a-c) Plot of $(\alpha h\nu)^2$ against photon energy for copper oxide thin films deposited on polyimide substrate at different substrate temperatures.

TABLE I
Dependence of Electrical Resistivity and Carrier on the Temperature Substrates

T(°C)	Resistivity (Ω m)	Carrier concentration (cm^3)
250	77.4	6.3×10^{15}
275	63.5	8.5×10^{15}
300	52.7	10.1×10^{15}

The optical band gap (E_g) was determined by analyzing the optical data with the expression for the optical absorbance (α) and the photon energy (hv) using Tauc's equation (Tauc, 1974).

$$(\alpha hv) = k(hv - E_g)^n \quad (3)$$

Where n = ½ for allowed direct transition (for a direct band gap semiconductor), and k is a constant. The energy band gap was then estimated from the straight line of the plot $(\alpha hv)^2$ versus photon energy for CuO thin films, as shown in Fig. 5. Extrapolation of the linear portion of the graph to the energy axis at $\alpha = 0$ gives the band gap energy (E_g) (Muhammad, et al., 2017; Muhammad and Sulaiman, 2011). The results of E_g for the CuO films were estimated to be in the range from 1.619 to 1.406 eV with respect to various substrate temperatures (250, 275, and 300°C), respectively. These values were found to be close to the value of energy gap for bulk CuO (1.5 eV) (Valladares, et al., 2012).

C. Electrical Properties

Hall effect measurements showed that all the films are of p-type conductivity. The dependence of the electrical resistivity and the carrier concentration on the temperature substrates is shown in Table I. It is seen that the electrical resistivity of the films decreases with the substrate temperature and the carrier concentration increases from 6.3 × 1015 cm−3 to 10.1 × 1015 cm−3 with increasing temperatures. The increased bulk carrier concentration caused by increasing the substrate temperature reduced the grain boundary potential barrier. The decrease in resistivity can be ascribed to the increase in carrier concentration. This outcome concurs with recently revealed information (Mohamed, et al., 2016). The increase in the carrier concentration causes shrinkage in the gap and also due to the decrease in resistivity. This signifies that density of dislocation and density of grain boundaries decrease. Therefore, it could be related to an improvement of the crystallinity leading to a decrease of donor sites trapped at dislocations and grain boundaries (Lee and Park, 2004; Oztas, et al., 2006).

IV. Conclusion

CuO thin films were deposited on PI plastic substrates with chemical spray pyrolysis. The effects of substrate temperature (250, 275, and 300°C) on the structural, optical, and electrical properties of the films deposited were studied. XRD patterns confirm the proper phase formation of the CuO. The crystallite grain sizes for as-deposited CuO films were 49.3–81.2 nm at different temperatures ranging from 250 to 300°C in 25°C steps. It was observed that crystallite grain size increased with increasing film temperature. The RMS roughness of the films increased as the film temperatures increased. The transmittance increases with increasing of substrate temperature. The optical band gap was also found to vary from 1.619 to 1.406 eV. Depending on the substrate temperature, hall measurement showed that the electrical resistivity and the carrier concentration varied from 77.4 Ω cm to 52.7 Ω cm and 6.3×10^{15} cm^{-3} to 10.1×10^{15} cm^{-3}.

References

Abbas, S.Z., Aboud, A.A., Irfan, M., and Alam, S., 2013. Effect of substrate temperature on structure and optical properties of Co_3O_4 film prepared by spray pyrolysis technique. *IOP Conference Series Materials Science and Engineering*, 60, pp.012058.

Akkari, F.C., Kanzaria, M., and Rezig, B., 2007. Preparation and characterization of obliquely deposited copper oxide thin films. *European Physical Journal-Applied Physics*, 40, pp.49-54.

Amri, A., Duan, X.F., Yin, C.Y., Jiang, Z.T., Mahbubur, R.M., and Pryor, T., 2013. Solar absorptance of copper-cobalt oxide thin film coatings with nano-size, grain-like morphology: Optimization and synshrotron radiation XPS studies. *Applied Surface Science*, 275, pp.127-135.

Birks, L., 1946. Particle size determination from X-Ray Line Broadening. *Journal of Applied Physics*, 17, pp.687-692.

Chandrasekaran, S., 2013. A novel single step synthesis, high efficiency and cost effective photovoltaic applications of oxidized copper nano particles. *Solar Energy Materials and Solar Cells*, 109, pp.220-226.

Chaudhary, Y.S., Agrawal, A., Shrivastav, R., Satsangi, V.R., and Dass, S., 2004. A study on the photo electrochemical properties of copper oxide thin films. *International Journal of Hydrogen Energy*, 29, pp.131-134.

Dolai, S., Dey, R., Das, S., Hussain, S., Bhar, R., and Pal, A.K., 2017. Cupric oxide (CuO) thin films prepared by reactive d.c. magnetron sputtering technique for photovoltaic application. *Journal of Alloys and Compounds*, 724, pp.456-464.

Faraj, M.G., and Omar, H.D., 2014. The effect of substrate temperature on the structural properties of spray pyrolysed lead sulphide (PbS) thin films. Aro the Scientific Journal of Koya University, 2, pp.11-14.

Faraj, M.G., and Pakhuruddin, M.Z., 2015. Deposited lead sulfide thin films on different substrates with chemical spray pyrolysis technique. *International Journal of Thin Films Science and Technology*, 4, pp.215-217.

Faraj, M.G., and Taboada, P., 2017. Comparative studies of the properties of ZnO sprayed thin films on different polymer substrates for flexible solar cell applications. *Journal of Inorganic and Organometallic Polymers and Materials*, 27, pp.1405-1411.

Faraj, M.G., and Taboada, P., 2017. Structural and optical properties of ZnO thin films prepared by spray pyrolysis on PI plastic substrates at various temperatures for integration in solar cell. *Journal of Materials Science: Materials in Electronics*, 28, pp.16504-16508.

Faraj, M.G., Ibrahim, K., Eisa, M.H., and Alrajhi, M.A., 2014. Comparison of aluminium thin film deposited on different polymer substrates with thermal evaporation for solar cell applications. *Journal of Ovonic Research*, 10, pp.231-235.

Faraj, M.G., Pakhuruddin, M.Z., and Taboada, P., 2017. Effects of substrate temperature on structural and optical properties of spray pyrolyzed $Cu(Ga_{0.3}In_{0.7})Se_2$ thin films on polyimide plastic substrate. *Journal of Electronic Materials*, 46, pp.6745-6749.

Faraj, M.G., Pakhuruddin, M.Z., and Taboada, P., 2017. Structural and optical properties of cadmium sulfide thin films on flexible polymer substrates by chemical spray pyrolysis technique. *Journal of Materials Science: Materials in Electronics*, 28, pp.6628-6634.

Haug, F.J., Geller, Z.S., Zogg, H., Tiwari, A.N., and Vignali, C., 2001. Influence of deposition conditions on the thermal stability of ZnO: Al films grown by rf magnetron sputtering. *Journal of Vacuum Science and Technology*, A19, pp.171-174.

Hubner, M., Simion, C.E., Tomescu-Stanoiu, A., Pokhrel, S., Barsan, N., and Weimar, U., 2011. Influence of humidity on CO sensing with p-type CuO thick film gas sensors. *Sensors and Actuators B*, 153, pp.347-353.

Hussein, A.N., Muhammad, S.K., Mohsin, S.A., and Ajeel, F.N., 2015. Study on structure and optical properties of CuO thin films prepared by chemical spray pyrolysis. *Journal of Applied Physical Science International*, 4, pp.178-184.

Ismail, R.A., and Faraj, M.G., 2009. Study of optical and electrical properties of CdO prepared by chemical spray pyrolysis. *Journal of College of Education, AL-Mustansiriyah University*, 3, pp.532-539.

Lee, J.H., Park, B.O., 2004. Transparent conducting In_2O_3 thin films prepared by ultrasonic spray pyrolysis. *Surface and Coatings Technology*, 184, pp. 102-107.

Mariammal, R.N., Ramachandran, K., Kalaiselvan, G., Arumugam, S., Renganathan, B., and Sastikumar, D., 2013. Effect of magnetism on the ethanol sensitivity of undoped and Mn-doped CuO nanoflakes. *Applied Surface Science*, 270, pp.545-552.

Mohamed, J.R., Sanjeeviraja, C., and Amalraj, L., 2016. Influence of substrate temperature on physical properties of (111) oriented CdIn2S4 thin films by nebulized spray pyrolysis technique. *Journal of Asian Ceramic Societies*, 4, pp.191-200.

Morales, J., Sanchez, M., 2005. Use of low-temperature nanostructured CuO thin films deposited by spray-pyrolysis in lithium cells. *Thin Solid Films*, 474, pp.133-140.

Muhammad, F.F., and Sulaiman, K., 2011. Utilizing a simple and reliable method to investigate the optical functions of small molecular organic films Alq3 and Gaq3 as examples. *Measurement*, 44, pp.1468-1474.

Muhammad, F.F., Yahya, M.Y., Aziz, F., Rasheed, M.A., and Sulaiman, K., 2017. Tuning the extinction coefficient, refractive index, dielectric constant and optical conductivity of Gaq3 films for the application of OLED displays technology. *Journal of Materials Science: Materials in Electronics*, 28, pp.14777-14786.

Nalbant, A., Ertek, O., and Okur, I., 2013. Producing CuO and ZnO composite thin films using the spin coating method on microscope glasses. *Materials Science and Engineering*, 178, pp.368-374.

Oztas, M., Bedir, M., Kayalı, R., and Aksoy, F., 2006. Influence of the annealing conditions on the properties of InP thin films. *Materials Science and Engineering: B*, 131, pp.94-99.

Tauc, J., 1974. *Amorphous and Liquid Semiconductors*. Plenum Press, New York.

Valladares, L.D.L., Salinas, D.H., Bustamante, D.A., Acosta, N.D., Khondaker, S.I., Mitrelias, T., Barnes, C.H.W., Albino, J., and Y.M, 2012. Crystallization and electrical resistivity of Cu_2O and CuO obtained by thermal oxidation Cu thin films on SiO_2/Si substrates. *Thin Solid Films*, 520, pp.6368-6374.

L-Tryptophan as Fluorescent Probe for Determination of Folic Acid in Some Pharmaceutical Products

Tara F. Tahir[1], Aryan F. Qader[2], Musher I. Salih[2], Essa Q. Rashid[3]

[1]Department of Medical Microbiology, Faculty of Science and Health, Koya University, Koya KOY45, Kurdistan Region - F.R. Iraq

[2]Department of Chemistry, Faculty of Science and Health, Koya University, Koya KOY45, Kurdistan Region - F.R. Iraq

[3]Kurdistan Medical Control Agency, Kurdistan Region - F.R. Iraq

***Abstract*—A new fluorescent probe L-Tryptophan was reported for the determination of folic acid (FA), based on its quenching effect of the fluorescence intensity of L-Tryptophan. The concentration of FA was proportional to the quenched fluorescence intensity of L-Tryptophan at excitation and emission wavelengths of 281 nm and 365 nm, respectively, in Britton–Robinson buffer solution of pH 7. Optimized conditions of pH, reaction time, potential interferences, concentrations of L-tryptophan, and buffer were investigated. FA was determined in a linear range of 2.0–16.0 µg ml with a correlation coefficient R^2 0.9974. The limit of detection and limit of quantification values were 0.09 µg/ml and 0.27 µg/ml, respectively. Relative standard deviation values for five replicated measurements of 2, 8, and 16 µg/ml FA were between 0.23 % and 1.07%. This method is efficient for routine analysis and quality control assay as it is relatively interferences free.**

***Index Terms*—Folic acid, L-Tryptophan, Pharmaceutical tablet, Spectrofluorimetry.**

I. Introduction

Vitamins are crucial for the growth and normal development of living beings. Vitamin B_9 that belongs to water-soluble B-group vitamin is essential for human body and has different chemical forms, folic acid (FA) and folate (Nasser, et al., 2005; Catharino, et al., 2006; Zare, et al., 2011). Folate is the general formula of Vitamin B_9 existed in food (Krishnaswamy and Nair, 2001) whereas FA is the synthetic form of this vitamin in the supplements and fortified foods (Bailey, 2000). FA has the chemical formula N-[4-[[(2-amino-3,4-dihydro-4-oxo-6-pteridinyl)methyl]amino]benzoyl]-L-glutamic acid (Nagaraja, et al., 2002; Flores, et al., 2005; Deconinck, et al., 2011) (Fig. I). Human body is supplied with FA from its main dietary sources such as spinach, white beans, asparagus, dark-leaved vegetables, Brussels sprouts, soybean, oranges, and melons (Nasser, et al., 2005; Deconinck, et al., 2011). FA is vital for the formation and growth of red blood cells besides the prevention of anemia (Zhao, et al., 2006). This vitamin-like others cannot be synthesized by mammalian cells and must, therefore, be supplied in sufficient amounts in the diet (Aurora-Prado, et al., 2004).

Deficiency of Vitamin B_9 is resulted mainly from poverty, food preferences, drug use, and chronic alcoholism. In the case of the insufficient taking of Vitamin B_9, multivitamin supplements can be used to prevent the associated physiological problems (Aurora-Prado, et al., 2004; Deconinck, et al., 2011). FA limitation can lead to congenital malformations in the fetus (spina bifida, encephalocele, cleft palate, and hydrocephalus), as well as heart disease (Czeize and Dudas, 1992; Crane, et al., 1995; Oakley, et al., 1995).

FA is important for normal growth, reproduction (during gestation and lactation), and antibody formation. It functions as a coenzyme in the metabolism of amino acids (glycine), the synthesis of purines, pyrimidines, DNA, and RNA is crucial for cell division and protein synthesis. Its defect can modify DNA synthesis and induce chromosomal changes (Pacheco, et al., 2009). Lack of FA causes high risk for neural tube defects (Pacheco, et al., 2009). The extremity of these defects means; it is important to undertake genetic counseling, supplement diets with FA, and perform prenatal diagnosis of neural tube defects (Pacheco, et al., 2009).

Although FA is nontoxic, there is some concern that high doses may mask pernicious anemia. This result is only likely following ingestion of quantities >5 mg. Consuming medicines of FA levels above the approved value can be toxic to the patient (Kennedy, 2016). Therefore, there is a continuing necessity for the development of new analytical procedures for the determination of FA present in pharmaceutical formulations (Zhao, et al., 2006).

High-performance liquid chromatography (HPLC) is considered as a popular analytical technique for identification and quantification of FA in pharmaceutical formulations (Póo-Prieto, et al., 2006). In spite of the advantages of HPLC as it is a well-established technology in the pharmaceutical field, offering sensitivity and specificity, it has disadvantages include

ARO-The Scientific Journal of Koya University
Volume VII, No.2 (2019), Article ID: ARO.10557, 8 pages
DOI: 10.14500/aro.10557
Received 04 August 2019; Accepted 07 October 2019
Regular research paper: Published 10 December 2019
Corresponding author's e-mail: tara.fuad@koyauniversity.org

 http://dx.doi.org/10.14500/aro.10557

high operating costs, the need for large amounts of samples and solvents, and the generation of hazardous wastes such as organic solvents that are expensive to dispose of and can have remarkable environmental impacts (Deconinck, et al., 2011).

In the literature the reported methods for the determination of FA include hyphenated techniques of HPLC with different detectors (Aurora-Prado, et al., 2004; Nelson, et al., 2006; Chaudhary, et al., 2010), electrophoresis (Zhao, et al., 2006), electrochemical methods (Vaze and Srivastava, 2007; Prasad, et al., 2010; Ensafi and Karimi-Maleh, 2010), flow injection analysis (Nie, et al., 2000), and spectrophotometric methods (Pesce and Bodourian, 1986; Rao, et al., 1978).

The use of derivative spectrophotometry provides a simple and inexpensive solution for the determination of drugs in pharmaceutical formulations. Meanwhile, using zero-order spectrophotometry for the determination of FA in complex samples that contain large amounts of interferents has the disadvantage of prior extraction of the analyte and thus increasing the costs of routine analysis (Moura and Moita, 2012).

Molecular fluorescence has one of the most attractive characteristics, its inherent sensitivity, which is often one to three orders of magnitude better than absorption spectroscopy. Actually, single molecules of selected species have been detected by fluorescence spectroscopy under controlled conditions. Besides, the large linear concentration ranges of fluorescence methods, which are remarkably broader than linear concentration range in absorption spectroscopy. However, the smaller number of chemical systems that show appreciable fluorescence has been made fluorescence methods less widely applicable than absorption methods (Cruces, et al., 1994; Skoog, et al., 2013). The aim of the present work was, therefore, to use a simple, low cost but sensitive and selective analytical method as spectrofluorimetry for quantification of FA in pharmaceuticals based on its quenching to the fluorescence emission of L-Tryptophan (Fig. II). The results were compared with the recommended method described in the literature.

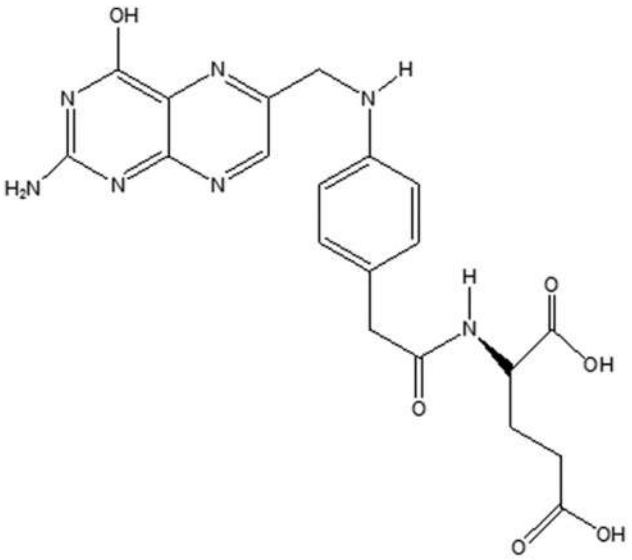

Fig. 1. Chemical structure of folic acid.

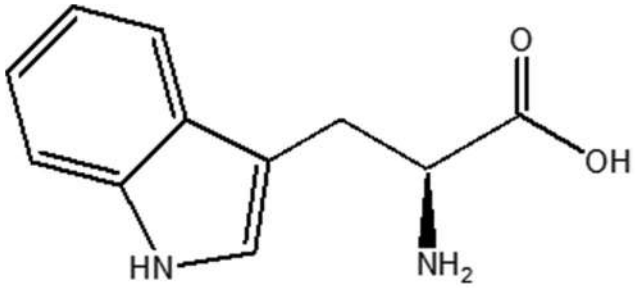

Fig. 2. Chemical structure of L-tryptophan.

II. Experimental

A. Apparatus

Fluorescence spectra measurements were carried out using Agilent Cary Eclipse Fluorescence Spectrophotometer, USA, with both slits width 5.0 nm and a quartz cell of 1.0 cm optimal path length. CyberScan pH 510 pH/mV meter was used for pH measurements of the solutions.

B. Material and Reagent

FA was obtained from Awamedica Pharmaceutical Company (Kurdistan Region-Iraq), used as received, the purity of which was 98%. A solution of 4.0×10^{-4} mol/L L-Tryptophan (from Sigma-Aldrich) was prepared by dissolving 0.0082 g of the solid in 50.0 ml of 0.1 mol/L NaOH solution. Different buffer solutions were prepared by mixing proper volumes of 0.1 mol/L sodium acetate (from Scharlau) and 0.1 mol/L acetic acid (from Scharlau) to prepare acetate buffer solution; 0.1 mol/L K_2HPO_4 (from Merck) and 0.1 mol/L KH_2PO_4 (from Sigma-Aldrich) to prepare phosphate buffer solution; and 0.04 mol/L phosphoric acid (from Merck), 0.04 mol/L boric acid (from Sigma-Aldrich), and 0.04 mol/L acetic acid (from Scharlau) to prepare Britton–Robinson (BR) buffer solution, respectively. A suitable volume of 0.2 mol/L sodium hydroxide (from Merck) was then added to adjust the pH using a pH meter.

C. Preparation of Standard and Sample Solution

A stock solution of standard FA (1.0 mg/ml) was prepared by dissolving 0.05 g in 40.0 ml of 0.1 mol/L NaOH with carefully stir, then completed to 50.0 ml with the same solvent and kept in a cool dark place. Working standard solutions were prepared daily by proper dilution of the stock standard solution with the same solvent.

All pharmaceutical products of FA in the local medical store are containing 5 mg and five different companies were used for the quantification; (Joriver, Jordan), (Wockhardt, UK), (Eipico, Egypt), (Actavis, US), and (Julphar, UAE). Ten tablets of FA were weighed and crushed for each pharmaceutical company, and then sample powder of the five companies was accurately weighed individually and placed in a 50.0 ml beaker and dissolved with 40.0 ml of 0.1 mol/L NaOH. The solution was stirred for 10 min to increase solubility. Insoluble excipient was removed by filtration using

Whatman No.41 membrane filter paper. The filtered solution was diluted to 50.0 ml with the same solvent.

D. Analytical Procedure

In 10.0 ml volumetric flask, 0.25 ml L-Tryptophan (4.0×10^{-4} mol/L), 0.8 ml BR buffer solution (pH 7.0), and adequate FA standard or sample 2.0–16.0 µg/L (0.2–1.6 ml) of 100 µg/L solution were added. This mixture was diluted to 10 ml with distilled water and mixed thoroughly for 10 min at 25 ± 2°C. The fluorescence intensity was measured against a blank with excitation wavelength at 281 nm and emission at 365 nm.

III. Results and Discussion

A. Optimization of Experiment

All parameters of the optimum conditions of fluorescence spectra of L-Tryptophan quenched by FA have been examined to obtain maximum sensitivity of the procedure. Different parameters such as pH, concentration of fluorescent probe L-Tryptophan, reaction time, and interferences were studied.

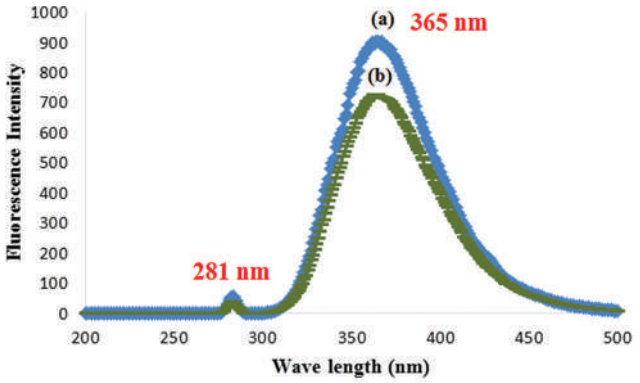

Fig. 3. Fluorescence excitation and emission spectra of (a) L-Tryptophan (4.0×10^{-4} mol/L), (b) L-Tryptophan (4.0×10^{-4} mol/L) with 5 µg/ml folic acid at pH 7.

Fluorescence emission spectra

The fluorescence spectrum of L-Tryptophan (4.0×10^{-4} mol/L) solution was recorded at excitation and emission wavelengths at 281 nm and 365 nm, respectively (Fig. IIIa). The intensity of the native fluorescence of L-Tryptophan marked quenches without any shift when 5 µg/ml FA was added to the solution containing (4.0×10^{-4} mol/L) L-Tryptophan. A new ion associated complex, produced during quenching of L-Tryptophan fluorescence (Fig. IIIb). Therefore, L-Tryptophan could be used as a fluorescent probe for FA.

pH buffer

Different buffer solutions of pH range (2–10) were examined for the reaction of 4.0×10^{-4} mol/L L-Tryptophan solution with 5 µg/ml FA. Acetate buffer, phosphate buffer, and BR buffer were carried out in the reaction, individually (Fig. IVa). It was observed that BR buffer of pH 7 has maximum intensity of quenched fluorescence spectrum of L-Tryptophan solution with FA due to the fact that FA acts as an acid and can quench the fluorescence spectrum of L-Tryptophan effectively in neutral medium. Therefore, this buffer was selected for next investigations.

To optimize the volume of BR buffer solution, different volumes (0.2, 0.4, 0.6, 0.8, 1.0, and 1.2 ml) were added to the solution of L-Tryptophan with FA where 0.8 ml solution of BR buffer showed the maximum intensity of quenched fluorescence spectrum (Fig. IVb).

L-Tryptophan concentration and reaction time

Different volumes (0.1–25 ml) of 4.0×10^{-4} mol/L L-Tryptophan reagent were investigated with fixed (5 µg/ml) concentration of FA and BR buffer solution (pH 7) to obtain the maximum intensity of fluorescence spectrum. Fig. V showed that 0.25 mL volume of L-Tryptophan has maximum ΔF intensity.

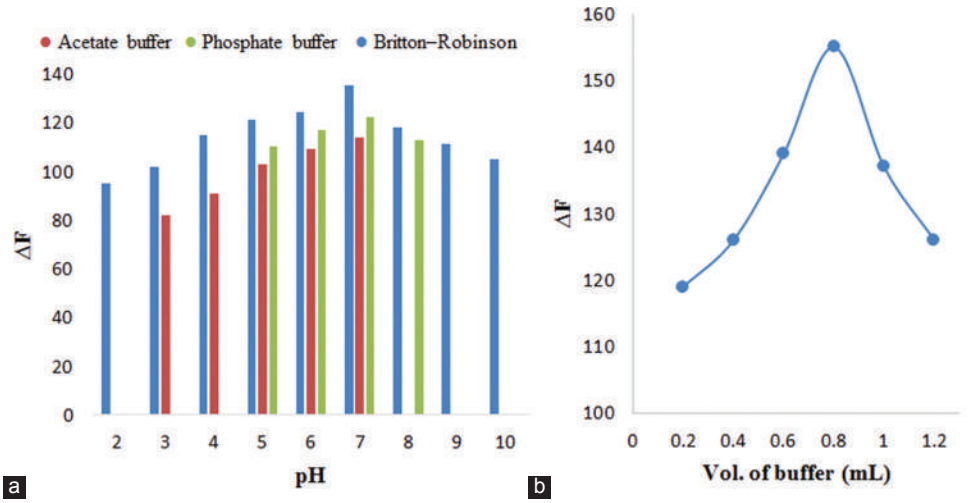

Fig. 4. (a) Effect of different pH buffer solutions on ΔF intensity of 4.0×10^{-4} mol/L L-Tryptophan solution with (5 µg/ml) folic acid; (b) different volumes of Britton–Robinson buffer versus ΔF intensity of L-Tryptophan solution with folic acid.

http://dx.doi.org/10.14500/aro.10557

The temperature had little influence on the fluorescence intensities of the system. The quenched fluorescence intensity (ΔF) slightly increased with temperature up to 20ºC and then remained constant up to 25°C. Therefore, room temperature (25°C) was selected for further study. The reaction time of mixing L-Tryptophan with FA at ambient temperature (25 ± 2°C) versus fluorescence intensity was also examined. It was found that quenching of the fluorescence intensity reached a maximum after 10 min from mixing the reagent with FA and remained constant for more than 100 min (Fig. VI).

Evaluation of selectivity

The excipients that are used in the pharmaceutical products in the form of tablets and capsules were used for selectivity assessment of FA under optimal experimental conditions (Manzoori, et al., 2011). The excipient solutions (500 µg ml) of lactose, fructose, glucose, starch, sucrose, and sodium chloride were mixed with 12 µg/ml FA in 10 ml of volumetric flask, individually. The spectra obtained were compared with the spectrum of (12 µg/ml) FA standard solution.

A level of interference was considered to be acceptable when the error is not higher than 3%. No significant levels of interferences were observed in the determination of FA in the presence of the common excipients (Table I).

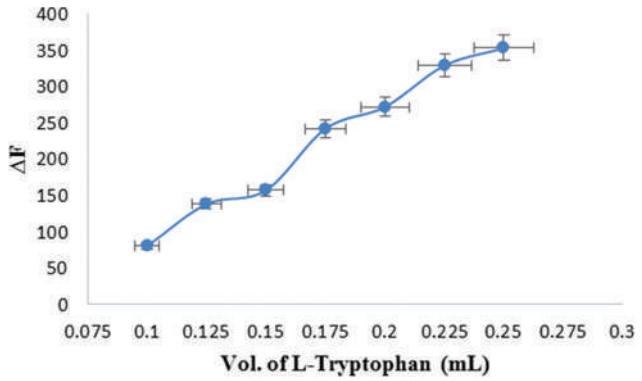

Fig. 5. Different volumes (0.1–25 ml) of 4.0 × 10^{-4} mol/L L-Tryptophan and fixed (5 µg/ml) folic acid versus ΔF intensity of the fluorescence.

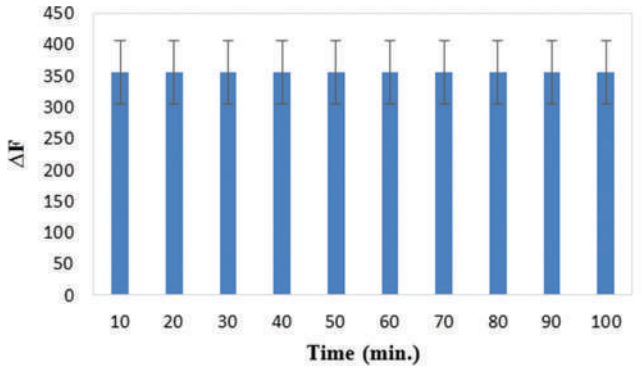

Fig. 6. Influence of reaction time of 4 × 10^{-4} mol/L L-Tryptophan with (5 µg/ml) folic acid at pH 7 on ΔF intensity of the fluorescence.

B. Analytical Figures of Merit

The determination of FA was investigated under optimum experimental conditions when the relative standard deviation (RSD%) was 1.07% as obtained from five replicated measurements of three different concentrations of FA. According to IUPAC guidelines of the validation of analytical method, the limit of detection (LOD) value = 3.3 SD/P and limit of quantification (LOQ) on value = 10 SD/P were adopted, in which SD is the standard deviation of five reagent blank measurements and P is the gradient of the calibration curve (Abd Ali, et al., 2019). The linear range was 2–16 µg/ml with correlation coefficient R^2 = 0.9974 and LOD 0.09 µg/ml (Fig. VII). The regression equation of standard solutions was ΔF = 40.119 C_{FA} + 140.2 in which C_{FA} is in µg/ml. The LOQ value of FA was 0.27 µg/ml.

The accuracy and precision of the proposed procedure was established by measuring the fluorescence intensity of three concentrations of standard FA in five replicates measurements (Table II). The values of RSD % and E % were between 1.10%–2.30% and −2.50%–1.10%, respectively, indicating that the method is valid and applicable.

C. Stoichiometry of the Reaction

The stoichiometry of the reaction between FA and L-Tryptophan was determined to adopt the limiting logarithmic method (Lakowicz, 2006). The proposed mechanism of the quenching reaction of FA and L-Tryptophan is the formation of an ion associated complex. Fig. VIII indicated a plot of log [FA] versus log ΔF at constant concentration of L-Tryptophan and log [L-Tryptophan] versus log ΔF at constant concentration of FA, respectively. Both plots were straight lines and depending on the gradients, the ratio of FA: L-Tryptophan complex is 1:1.

D. Quenching Mechanism of L-Tryptophan and FA

Fluorescence quenching is the decrease of the quantum yield of fluorescence from a fluorophore induced by a variety of molecular interactions, such as excited-state reactions, photoinduced electron transfer, fluorescence resonance energy transfer, ground-state complex formation, and collisional quenching (Bhattacharyya, et al., 1990). The physical origin of fluorescence quenching arising from the addition of a quenching agent, L-Tryptophan, to FA fluorescence can be

TABLE I
EVALUATION OF SELECTIVITY OF FA QUANTIFICATION USING L-TRYPTOPHAN TOWARDS SOME COMMON EXCIPIENTS PRESENTED IN THE PHARMACEUTICAL PRODUCTS

Coexisting materials	Allowance concentrations (µg/ml)	E %*
Lactose	500	2.10
Fructose	500	2.20
Glucose	500	1.80
Starch	500	−1.40
Sucrose	500	−2.10
Sodium chloride	500	−1.50

*Average of three determinations

interpreted in terms of the formation of ion-associated complex that enhanced fluorescence quenching. In this mechanism the fluorophore itself (FA) is fluorescent when the receptor site (amine group) is free. In the presence of L-Tryptophan, the fluorescence intensity is lowered due to the reaction between the carboxylic group of L-Tryptophan and receptor unit (amine group) of FA to form nonfluorescent ion-associated complex, and therefore, the net fluorescence is quenched. (Fig. IX).

Basically, this quenching process can be divided into two kinds of mechanisms: Static and dynamic quenching. Static and dynamic quenching can be distinguished by their different dependences on the temperature and excited-state lifetime. Dynamic quenching is diffusion controlled because the quencher (L-Tryptophan) must diffuse to the fluorophore (FA) during the lifetime of the excited state. Since high temperature will result in a large diffusion coefficient, the bimolecular quenching constants are expected to increase with temperature. Static quenching implies either the existence of a sphere of effective quenching or the formation of a ground-state nonfluorescent complex, whereas collisional or dynamic quenching involves the collision followed by the formation of a transient complex between an excited-state fluorophore (FA) and a ground-state quencher (L-Tryptophan).

TABLE II
PRECISION AND ACCURACY DATA OF THE PROPOSED METHOD

Contained amount (µg/ml)	Found by proposed method (µg/mL)	SD	RSD%	E%*
2	1.95	2.30	1.07	−2.50
8	8.09	1.10	0.24	1.10
16	16.08	1.80	0.23	0.50

*Average of five determinations

E. Application to the Pharmaceutical Tablets

The proposed procedure using L-Tryptophan as fluorescence probe for quantification of FA was applied to pharmaceutical tablets. The ingredients in the pharmaceutical tablets did not interfere in the quantification of FA. The applicability of the proposed procedure for the analysis of FA in pharmaceutical formulations was examined by investigating various pharmaceutical tablets, and the results are tabulated in Table III and were compared to the standard FA assay using HPLC method by means of t- and F-values at 95% confidence level. HPLC has the ability to separate and identify compounds that are present in any sample that can be

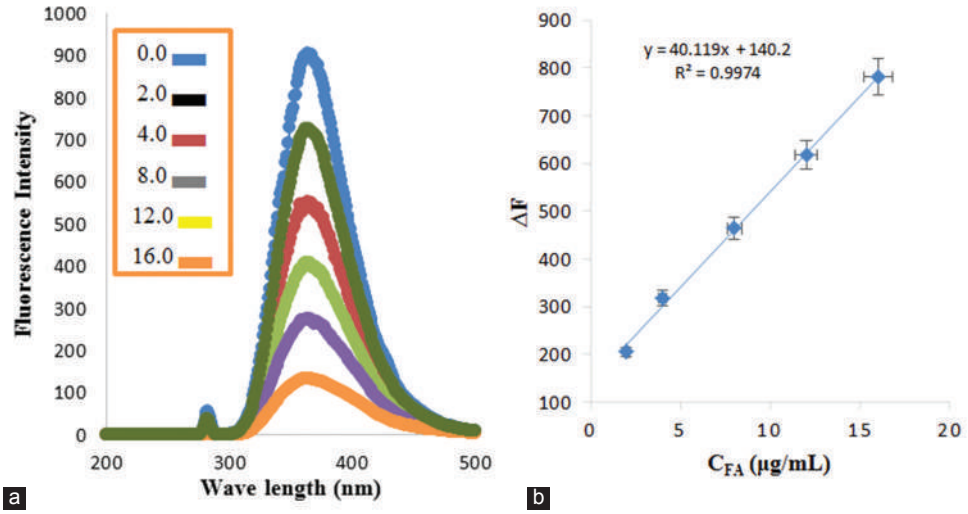

Fig. 7. (a) Different concentrations (2, 4, 8, 12, and 16 µg/ml) of folic acid versus fluorescence intensity of L-Tryptophan at pH 7. (b) Calibration curve of fluorometric quantitation of folic acid with L-Tryptophan under optimum condition.

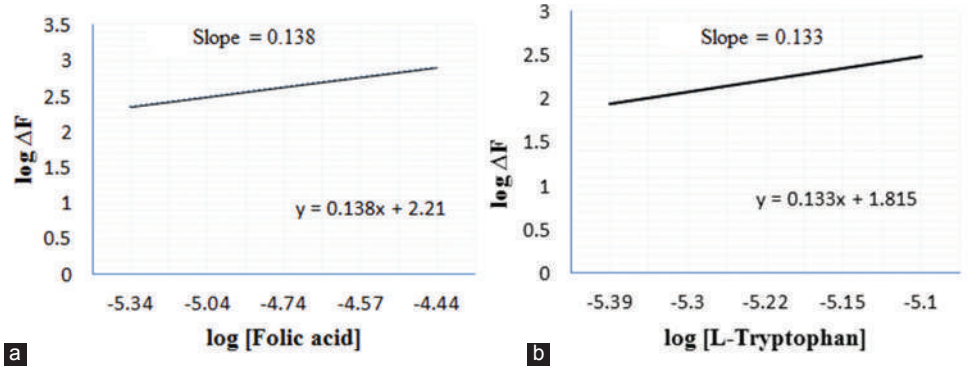

Fig. 8. Stoichiometric ratio of the fluorometric reaction of folic acid and L-Tryptophan reagent using a limiting logarithmic method. (a) Log[folic acid] versus log ΔF (b) Log [L-Tryptophan] versus log ΔF.

 http://dx.doi.org/10.14500/aro.10557

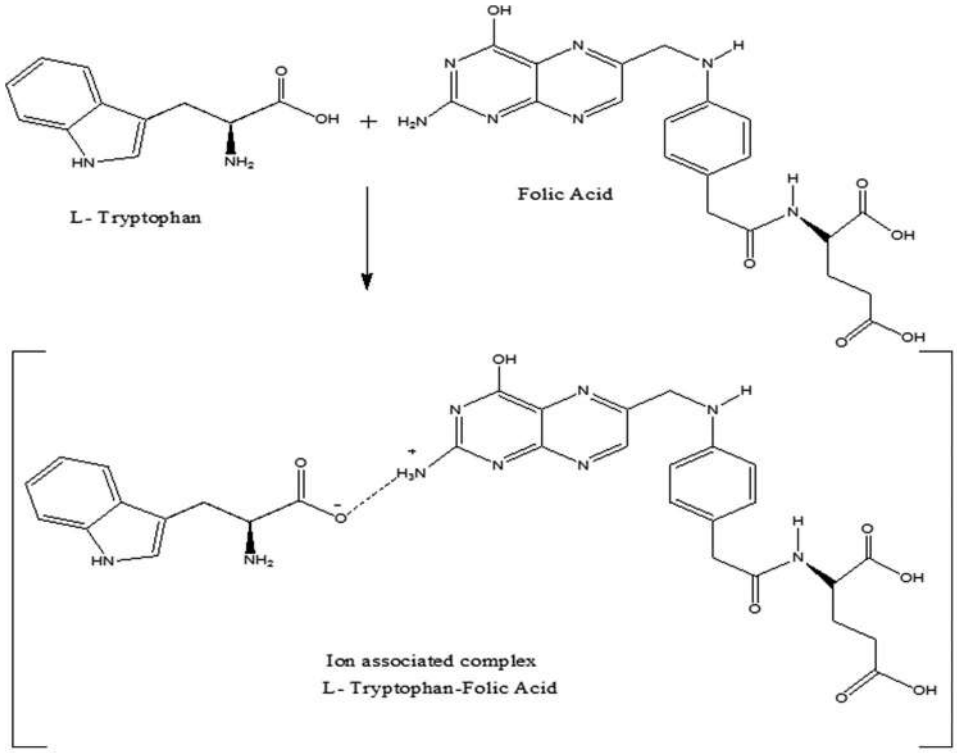

Fig. 9: Quenching mechanism of L-Tryptophan and folic acid due to the formation of ion associated complex.

TABLE III
Comparison of Fa Quantification in Pharmaceutical Tablets Using the Proposed Fluorometric L-Tryptophan Method and Standard Hplc Method

Pharmaceutical Tablets	Observed values (mg)	Values from proposed procedure	Values from HPLC	Recovery %	E %*	t and F values**
Joriver	5	4.86±0.19	4.98±0.02	97.6	−2.4	t=0.40, F=1.50
Wockhardt	5	5.10±0.12	5.01±0.10	101.8	1.8	t=1.95, F=1.00
Eipico	5	5.14±0.20	5.21±0.05	98.7	−1.3	t=0.73, F=2.20
Actavis	5	4.72±0.08	4.80±0.034	98.3	−1.7	t=0.80, F=1.07
Julphar	5	4.79±0.13	4.88±0.01	98.2	−1.8	t=0.23, F=3.20

*Average of five determinations. **Theoretical calculation of t and F at 95% confidence level (n=5) were 2.78 and 6.39 respectively

TABLE IV
Comparison of Determination of Folic Acid Using Different Analytical Techniques and the Proposed Method

Method's name	Ref.	LR	LOD	LOQ	pH
Spectrophotometer	Al-Araji, et al., 2017	0.75–10.50 µg/mL	0.159 µg/mL	0.531 µg/mL	11.0
Spectrofluorimeter	Manzoori, et al., 2011	0.01–1.10 mg/L	0.003 mg/L	-	6.2
Chromatography	Nelson, et al., 2006	0.02–73 ng	0.02 ng	0.06 ng	6.0
Electrochemistry	Mirmoghtadaie, et al., 2013	1.0×10^{-8}–1.0×10^{-6} mol/L	7.50×10^{-9} mol/L	-	12
HPLC	El-Leithy, et al., 2018	0.1–2 µg/mL	0.1 µg/mL	-	3.5–7.4
Proposed method	-	2.0–16.0 µg/mL	0.09 µg/mL	0.27 µg/ml	7.0

HPLC: High-performance liquid chromatography, LOD: Limit of detection, LOQ: Limit of quantification

dissolved in a liquid in trace concentrations as low as parts per trillion. The sample mixture or analyte is pumped with a solvent (mobile phase) in a column with chromatographic packing material (stationary phase) at high pressure. The sample is carried by a moving carrier gas stream of helium or nitrogen. Sample retention time will vary depending on the interaction between the stationary phase, the molecules being analyzed, and the solvent used. As the sample passes through the column it interacts between the two phases at different rates, primarily due to different polarities of analytes in the sample. Analytes that have the least amount of interaction with the stationary phase or the most amount of interaction with the mobile phase will exit the column faster. The HPLC system of Agilent 1100 controlled by ChemStation Data41 System and equipped with G 1311A quaternary pump and UV detector (VWD-G1314 A) was employed for the investigation. A reverse phase C18 column (Kromasil 100-5 Phenyl®, 300 mm × 4.6 mm, 5 µm) was used at 25°C. The experiment was run with mobile phase consisted of 0.1% v/v trifluoroacetic acid (TFA) and acetonitrile at ratio (80:20 v/v). It was injected with flow rate 1.5ml/min, and the elute was monitored at wavelength 290 nm.

In all cases, the average results obtained by the proposed procedure and standard method were statistically identical, and there were no significant differences between them at 95% confidence level. Therefore, the proposed methods are simple, sensitive, and reproducible and can be used for routine analysis of FA in pharmaceutical formulations.

Table IV shows the optimization results of the determination of FA using different analytical techniques and the proposed method. Although some analytical techniques have lower LOD value and wider linear range, the proposed method does not need pre-extraction of the sample besides the low cost of the technique compared with others such as HPLC.

IV. Conclusion

The proposed spectrofluorometry is simple, rapid, inexpensive, sensitive, and reproducible method for routine analysis of FA in pharmaceutical formulations without interference from common tablet excipients. The method has wide linear range with good accuracy and precision. The significance of the proposed method is direct measurement of FA in pharmaceutical formulations without need for pretreatment of the drug and extraction with organic solvent. Therefore, the method can be used successfully for quality control of FA in its dosage forms.

References

Abd Ali, L.I., Qader, A.F., Salih, M.I., and Aboul-Enein, H.Y., 2019. Sensitive spectrofluorometric method for the determination of ascorbic acid in pharmaceutical nutritional supplements using acriflavine as a fluorescence reagent. *Luminescence*, 34(2), pp.168-174.

Al-Araji, R.R., Mashkour, M.S., and Jaffar Al-Mulla, E.A., 2017. Spectrophotometric determination of vitamin folic acid B9 in some drugs using 1, 2-naphthoquine-4-sulphonate (NQS). *Nano Biomedicine and Engineering*, 9(3), pp.208-213.

Aurora-Prado, M.S., Silva, C.A., Tavares, M.F., and Altria, K.D., 2004. Determination of folic acid in tablets by microemulsion electrokinetic chromatography. *Journal of Chromatography A*, 1051(1), pp.291-296.

Bailey, L.B., 2000. New standard for dietary folate intake in pregnant women. *The American Journal of Clinical Nutrition*, 71(5), pp.1304-1307.

Bhattacharyya, M., Chaudhuri, U., Poddar, R.K., 1990. Evidence for cooperative binding of CPZ with hemoglobin. *Biochemical and Biophysical Research Communications*, 167, pp.1146-1153.

Catharino, R.R., Godoy, H.T., and Lima-Pallone, J.A., 2006. Analytical methodology for folate and folic acid determination in food. *Química Nova*, 29(5), pp.970-972.

Chaudhary, A., Wang, J., and Prabhu, S., 2010. Development and validation of a high-performance liquid chromatography method for the simultaneous determination of aspirin and folic acid from nano-particulate systems. *Biomedical Chromatography*, 24(9), pp.919-925.

Crane, N.T., Wilson, D.B., Cook, D.A., Lewis, C.J., Yetley, E.A., and Rader, J.I., 1995. Evaluating food fortification options: General principles revisited with folic acid. *American Journal of Public Health*, 85(5), pp.660-666.

Cruces, B.C., Segura, C.A., Fernández, G.A., and Román, C.M., 1994. Fluorometric determination of folic acid based on its reaction with the fluorogenic reagent fluorescamine. *Analytical Letters*, 27(7), pp.1339-1353.

Czeize, A.E., and Dudas, I., 1992. Prevention of the first occurrence of neural tube defects by perioconceptional vitamin supplementation. *The New England Journal of Medicine*, 327(226), pp.1832-1835.

Deconinck, E., Crevits, S., Baten, P., Courselle, P., and De Beer, J., 2011. A validated ultra-high pressure liquid chromatographic method for qualification and quantification of folic acid in pharmaceutical preparations. *Journal of Pharmaceutical and Biomedical Analysis*, 54(5), pp.995-1000.

El-Leithy, E.S., Abdel-Bar, H.M., and El-Moneum, R.A., 2018. Validation of high performance liquid chromatographic method for folic acid assay. *International Journal of Pharmaceutical Science Invention*, 7(1), pp.1-5.

Ensafi, A.A., and Karimi, M.H., 2010. Modified multiwall carbon nanotubes paste electrode as a sensor for simultaneous determination of 6-thioguanine and folic acid using ferrocenedicarboxylic acid as a mediator. *Journal of Electroanalytical Chemistry*, 640(1), pp.75-83.

Flores, J.R., Penalvo, G.C., Mansilla, A.E., and Gomez, M.J., 2005. Capillary electrophoretic determination of methotrexate, leucovorin and folic acid in human urine. *Journal of Chromatography B*, 819(1), pp.141-147.

Kennedy, D., 2016. B vitamins and the brain: Mechanisms, dose and efficacy a review. *Nutrients*, 8(2), p.68.

Krishnaswamy, K., and Nair, K.M., 2001. Importance of folate in human nutrition. *British Journal of Nutrition*, 85(2), pp.115-124.

Lakowicz, J.R., 2006. *Principles of Fluorescence Spectroscopy*. 3rd ed. New York: Springer. pp.277-330.

Manzoori, J.L., Jouyban, A., Amjadi, M., and Soleymani, J., 2011. Spectrofluorimetric determination of folic acid in tablets and urine samples using 1, 10-phenanthroline-terbium probe. *Luminescence*, 26, pp.106-111.

Mirmoghtadaie, L., Ensafi, A.A., Kadivar, M., Shahedi, M., and Ganjali, M.R., 2013. Highly selective, sensitive and fast determination of folic acid in food samples using new electrodeposited gold nanoparticles by differential pulse voltammetry. *International Journal of Electrochemical Science*, 8, pp.3755-3767.

Moura, J.I., and Moita, G.C., 2012. Simultaneous determination of olanzapine and fluoxetine hydrochloride in pharmaceutical formulations by derivative spectrophotometry. *Química Nova*, 35(3), pp.627-633.

Nagaraja, P., Vasantha, R.A., and Yathirajan, H.S., 2002. Spectrophotometric determination of folic acid in pharmaceutical preparations by coupling reactions with iminodibenzyl or 3-aminophenol or sodium molybdate pyrocatechol. *Analytical Biochemistry*, 307(2), pp.316-321.

Nasser, C., Nobre, C., Mesquita, S., Ruiz, J.G., Carlos, H.R., Prouvot, L., and Yacubian, M.T., 2005. Natural variation of folate in cowpea seeds. *Journal of Epilepsy and Clinical Neurophysiology*, 11(4), pp.199-203.

Nelson, B.C., Sharpless, K.E., and Sander, L.C., 2006. Quantitative determination of folic acid in multivitamin/multielement tablets using liquid chromatography/tandem mass spectrometry. *Journal of Chromatography A*, 1135(2), pp.203-211.

Nie, F., He, Y., and LU, J., 2000. An investigation of the chemiluminescence reaction in the sodium hypochlorite-folic acid-semicarbazide hydrochloride system. *Microchemical Journal*, 65(3), pp.319-323.

Oakley, G.P., Erickson, J.D., and Adams, M.J., 1995. Urgent need to increase folic acid consumption. *JAMA*, 274(21), pp.1717-1718.

Pacheco, S.S., Braga, C., Souza, A.I.D., and Figueiro, J.N., 2009. Effects of folic acid fortification on the prevalence of neural tube defects. *Revista de Saúde Pública*, 43(4), pp.565-571.

Pesce, M.A., and Bodourian, S.H., 1986. Evaluation of a fluorescence polarization immunoassay procedure for quantitation of methotrexate. *Therapeutic Drug Monitoring*, 8(1), p.115.

Póo-Prieto, R., Haytowitz, D.B., Holden, J.M., Rogers, G., Choumenkovitch, S.F., Jacques, P.F., and Selhub, J., 2006. Use of the affinity/HPLC method for quantitative estimation of folic acid in enriched cereal-grain products. *The Journal of Nutrition*, 136(12), pp.3079-3083.

Prasad, B.B., Tiwari, M.P., Madhuri, R., and Sharma, P.S., 2010. Development of a highly sensitive and selective hyphenated technique (molecularly imprinted micro-solid phase extraction fiber-molecularly imprinted polymer fiber sensor) for ultratrace analysis of folic acid. *Analytica Chimica Acta*, 662(1), pp.14-22.

Rao, G.R., Kanjilal, G., and Mohan, K.R., 1978. Extended application of folin-ciocalteu reagent in the determination of drugs. *Analyst*, 103(1230), pp.993-994.

Skoog, D.A., West, D.M., Holler, F.J., and Crouch, S.R., 2013. *Fundamentals of Analytical Chemistry*. 9th ed. Cengage Learning, Boston.

Vaze, V.D., and Srivastava, A.K., 2007. Electrochemical behavior of folic acid at calixarene based chemically modified electrodes and its determination by adsorptive stripping voltammetry. *Electrochimica Acta*, 53(4), pp.1713-1721.

Zare, H.R., Shishehbore, M.R., and Nematollahi, D., 2011. A highly sensitive and selective sensor on the basis of 4-hydroxy-2-(triphenylphosphonio) phenolate and multi-wall carbon nanotubes for electrocatalytic determination of folic acid in presence of ascorbic acid and uric acid. *Electrochimica Acta*, 58, pp.654-661.

Zhao, S., Yuan, H., Xie, C., and Xiao, D., 2006. Determination of folic acid by capillary electrophoresis with chemiluminescence detection. *Journal of Chromatography A*, 1107(1), pp. 290-293.

Aqra Anticline: A Growing Structure in the Iraqi Kurdistan Region

Ala A. Ghafur, Varoujan K. Sissakian, Hawkar A. Abdulhaq and Hassan O. Omer

Department of Natural Resources Engineering and Management, University of Kurdistan Hewler, Kurdistan Region - F.R. Iraq

***Abstract*— Aqra anticline is a doubly plunging anticline, oriented NW–SE with a steep southwestern limb and even overturned. Geomorphological features are interpreted using satellite images; as a result, it was found that the anticline shows clear geomorphological and structural features which indicate the lateral growth of the anticline. Among those features are water gaps, wind gaps, forked-shaped valleys, curved valleys, inclined valleys, and dislocated and abandoned alluvial fans. Some of the vague interpreted features were checked and confirmed in the field.**

***Index Terms*—Aqra anticline, En-echelon plunging, Lateral growth, Radial valleys, Water gap.**

I. Introduction

In tectonically active areas such as the Iraqi Kurdistan territory, which forms the Northeastern part of the Arabian plate, the lateral growth of anticlines is a very common phenomenon (Blanc, et al., 2003; Bennett, et al., 2005; Ramsey, et al., 2008). The existing anticlines in the region and associated main thrust faults within the anticlines are developed due to the exerted stress forces by the collision of the Arabian plate with the Iranian plate, with a convergent tectonic plate boundary (Alavi, 2004; Allen, et al., 2004). Moreover, mountain building and landscape evolution are controlled by interactions between river dynamics and tectonic forces. Indirect information on tectonic activity can be provided by landscape geomorphology and drainage patterns (Oberlander, 1985; Alvarez, 1999; Burbank and Pinter, 1999; Keller, et al., 1999; Keller and Pinter, 2002; Bretis, et al., 2011; Collignon, et al., 2016). The described geomorphic criteria of many researchers, for example, Keller, et al. (1999) and Keller and Pinter (2002) can be used for the evaluation of fold growth. Among the criteria are: (1) The deformation of progressively younger deposits or landforms, (2) the development of characteristic asymmetric drainage patterns, (3) the occurrence of a series of wind gaps with decreasing elevation in the propagation direction, (4) the development of water gaps (WG), (5) the presence of en-echelon plunges, and (6) the development of cross-shaped valleys, axial valleys, fork-shaped valleys, and curved valleys. However, the presence of one or two of the mentioned criteria does not mean they indicate lateral growth of a fold. Many of those criteria collectively and repeatedly should be present to indicate the lateral growth.

The studied area includes Aqra anticlines, which is located Northwest of Erbil city, near to Aqra town within the Iraqi Kurdistan Region (Fig. 1). It forms an outstanding continuous mountain range with Peris anticline (Mountain) toward the East and Shaikhan anticline toward the west.

The aim of the current study is to confirm the lateral growth of the Aqra anticline using geomorphological features which are developed in the anticline. The recognition of the features was done by the interpretation of high-quality satellite images and field investigation.

A. Previous Studies

Tectonic geomorphological studies are not common in the Kurdistan Region as a whole and particularly in the studied area and near surroundings; among them are:

Sissakian (2010) conducted a tectonic geomorphological study of the Derbendi Bazian gorge, which represents a wind gap and attributed to the development of the gorge to neotectonic activity. Sissakian and Abdul-Jabbar (2010) conducted a study about the transversal gorges, among them are Basara gorge, which represents a WG and concluded that the gorge developed due to neotectonic activity. Sissakian and Fouad (2014) and Sissakian, et al. (2019) updated the geological map of Erbil and the Mahabad Quadrangles at a scale of 1:250,000. Aqra anticline is located within.

The updated map and demonstrated the details of the structural features, but the lateral growth of the anticline was not mentioned. Sissakian, et al. (2014) conducted a geomorphological study of the high folded zone and attributed the developed gorges in Aqra anticline to the lateral propagation (growth) of the anticlines. Al-Kubaisi and Abdul Jab'bar (2015) conducted a morphotectonic study of three folds in the Kurdistan region and their effect on the drainage systems. They indicated high tectonic activity and low maturity of the drainage basins in the studied anticlines. Sissakian, et al. (2018)

ARO-The Scientific Journal of Koya University
Volume VII, No.2 (2019), Article ID: ARO.10535, 7 pages
DOI: 10.14500/aro.10535
Received 31 May 2019; Accepted 07 September 2019
Regular research paper: Published 10 December 2019
Corresponding author's e-mail: ala.abdulla@ukh.edu.krd

http://dx.doi.org/10.14500/aro.10535

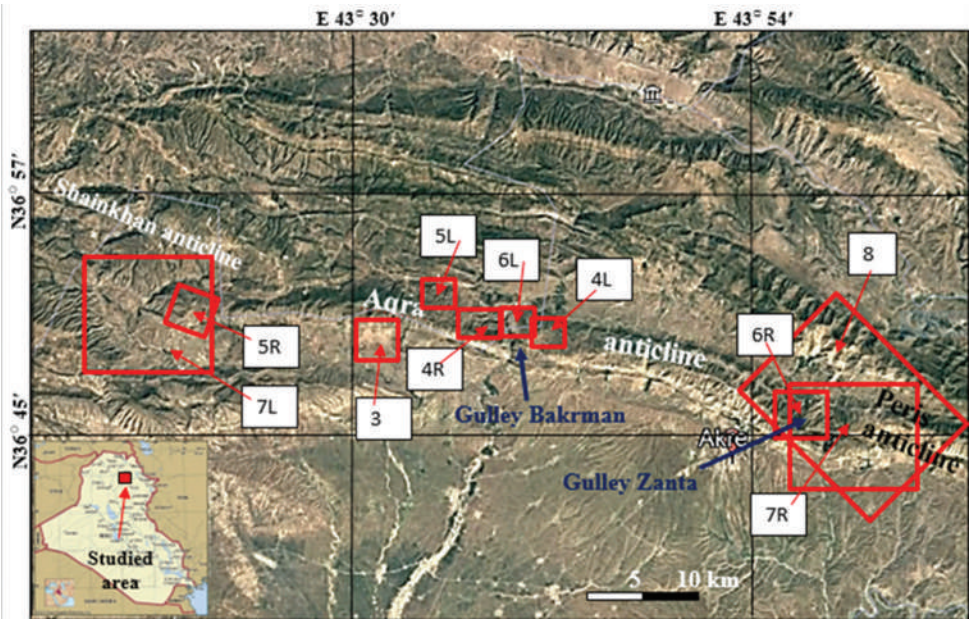

Fig. 1. Satellite image of the study area showing the Aqra anticline. Location of Figures 3-8 is identified in red boxes.

conducted a tectonic geomorphological study on the Qara Dagh anticline to indicate its lateral growth by means of the same geomorphological forms which are used in the current study.

Worldwide studies dealing with the concept of current study are very common; among them are: Cartwright, et al. (1995) conducted a geomorphological study to deduce the fault growth by segment linkage from the Canyonlands Grabens of SE Utah, USA. Bennett, et al. (2005) conducted a geomorphological study in South Rough Ridge, Central Otago, and New Zealand to deduce the lateral growth of a ridge along a blind fault. Mumipour and Najad (2011) and Mosavi and Arian (2015) conducted tectonic geomorphological studies in the Zagros Belt; Iran using geomorphological features to deduce the growth of anticlines.

II. Materials and Methods

To perform the current work and fulfill its aim, the following materials were used:

- Geological maps at a scale of 1:250,000
- Topographical maps at a scale of 1:100,000
- Satellite images of high quality to recognize geomorphological features
- Flied work was conducted to check the recognized geomorphological features.

To recognize geomorphological features which indicate the lateral growth of an anticline, the opinions of different researchers have been considered in the current study to indicate the lateral growth of the Aqra anticline, and to confirm the achieved conclusions from the current work. Among those researchers are Keller, et al. (1999), Keller and Pinter (2002), Ramsey, et al. (2008), and Collignon, et al. (2016).

Different geomorphological features were recognized by utilizing available topographical and geological maps of different scales, digital elevation model images, FLASH Earth, and software such as Global Mapper. The obtained features were used to signify the lateral growth of the Aqra anticline. Those indicated features were used to indicate the lateral growth of the Aqra anticline. Different geomorphological studies in the Zagros Range were reviewed to deduce the indication for the growth of anticlines, their evolution, and their current shapes. Different valley shapes which exist in the Aqra anticline and confirm its lateral growth, were recognized using many research prefects from: Keller, et al. (1999), Keller and Pinter (2002), Ramsey, et al. (2008), and Collignon, et al. (2016). The recognized geomorphological features in the networks of mountain belts are perhaps the most sensitive indicators of horizontal and vertical surface deformation, at least on Holocene time scale (Burbank and Anderson, 2001).

III. Geological Setting

The geological setting of the studied area is briefed hereinafter; including geomorphology, tectonics, and structural geology as well as stratigraphy.

Geomorphologically, the studied area is mountainous with very rugged cliffs and steep slopes. The main geomorphological forms are: Anticlinal ridges, abandoned alluvial fans, water and wind gaps, extensive karstification, and dissected slopes. The studied area is located in the high folded zone where the Aqra anticline forms the beginning of the high folded zone in the studied area; whereas its southern plain represents the low folded zone. The high folded zone belongs to the Outer Platform of the Arabian plate (Fouad, 2012) and is a part of the Zagros Fold-Thrust Belt (Alavi, 2004, Ramsey, et al., 2008). The Aqra anticline is a doubly plunging anticline trending NW–SE, with a very steep southwestern limb which exhibits vertical dipping and even overturned beds for long distances. The length and width of the anticline are 55 km and 6 km,

respectively. The Southeastern plunge forms an en-echelon plunge with the Peris anticline, whereas the Northwestern plunge is complicated and truncated by many faults which are developed in the carbonates of the Pila Spi Formation, causing wide coverage area for the exposures; accordingly, hindering the normal plunge shape of the anticline (Fig. 2). The exposed formations in the studied area are briefly described hereinafter, from the older to younger. Only those formations which are exposed in Aqra anticlines (Fig. 2) are briefed (Sissakian and Al-Jiburi, 2014 and Sissakian and Fouad, 2014).

Qamchuqa formation (lower cretaceous)

The formation is exposed only in the core of the Aqra anticline at Al-Khazir river gorge and Gulley Zanta. The formation consists of massive limestone, dolomitic limestone, and dolomite, usually dark gray and light brown in color. The exposed thickness of the formation is about 200 m.

Bekhme formation (upper cretaceous)

The formation is exposed widely in the Aqra anticline and forms the carapace of Aqra mountain. The formation consists of well-bedded limestone and dolostone, locally bituminous, coralline and recrystallized, very hard, and light gray in color. The thickness is 700 m; however, it decreases in then direction.

Shiranish formation (upper cretaceous)

The formation is exposed to both limbs of the anticline. The formation consists of thinly well-bedded marly and chalky limestone, white, and grayish white in color, followed (upward) by thinly bedded or papery marl, blue, and gray in color with presence of marly limestone beds too. The thickness of the formation is around 180 m.

Kolosh formation (Paleocene)

The formation is exposed on both limbs of the anticline as a thin belt. It consists of black shale, claystone, sandstone, and siltstone; some very thin layers of limestone may occur too. The thickness of the formation is 20 m.

Gercus formation (Paleocene-lower Eocene)

The formation is exposed on both limbs of the anticline as a thin belt, consists of red, claystone, sandstone, and siltstone; some very thin layers of limestone, conglomerate, and very rare gypsum beds may occur too. The thickness of the formation is 40 m.

Pila Spi formation (Eocene)

The formation is exposed on both limbs of the anticline as a thin belt and is very widely exposed in the Northwestern plunge area. It consists of well-bedded carbonate rocks. The thickness of the formation is about 85 m.

IV. Results and Interpretations

Geomorphological features which can be used as markers such as wind gaps and WGs (or transverse streams) have been extensively used to define the style of deformation and to quantify both the rate and the direction of propagation (or the lateral growth) of fault and fold segments (Burbank and Pinter, 1999; Keller, et al., 1999; Delcailleau, et al., 2006; Vergés, 2007; Ramsey, et al., 2008; Bretis, et al., 2011). WGs represent valleys that are developed by carving the exposed rocks during fold growth and that still host a flowing stream, whereas wind gaps constitute of similar valleys that are presently dry; witnessing previous WG, and the rate of the river incision is less than the rate of the fold growth.

The rate of rock and surface uplift, which shapes landscapes are controlled by deformation, climate, and rock properties. Understanding the interaction between these parameters and how they determine the formation of wind gaps, is a question with direct implications for predicting the release of sediments in local basins and at the outlet of fluvial basins (Collignon, et al., 2016). To understand the development of WGs and their changes (locally) to wind gaps, and the radial valleys, the opinion of Ramsey, et al. (2008) is adopted in the current study.

Abandoned alluvial fans are also good indicators for active tectonics in the area, where such fans occur. Among the active tectonics is the lateral growth and the uplift of folds (Skilodimou, et al., 2014); however, the climate change for the existence of abandoned alluvial fans cannot be ignored. Fig. 3 shows a large alluvial fan with two phases; an abandoned fan followed by an active fan.

Axial valleys and cross-shaped valleys on top of elevated areas are good indications for active tectonics (Cannat, et al., 1999). Fig. 4 shows the axial valley and cross-shaped valley at the Aqra anticline, indicating the lateral growth of the anticline.

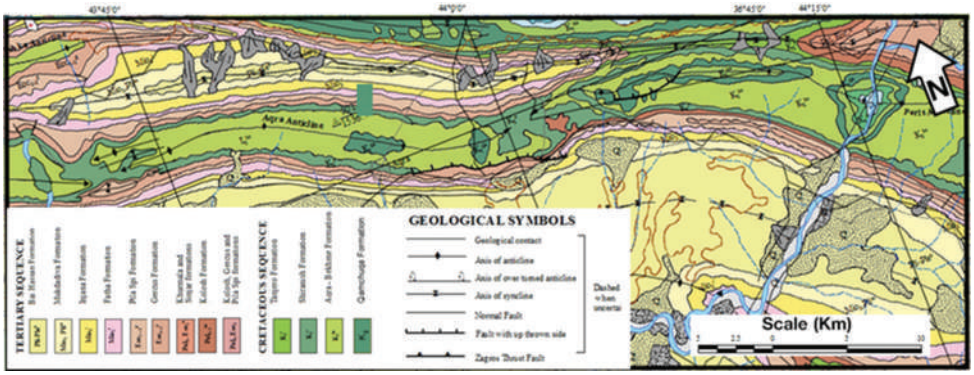

Fig. 2. Geological map of the studied area (after Sissakian, et al., 2019).

Fork-shaped valleys and radial valleys are also good indicators for the lateral growth of folds (Keller and Pinter, 2002; Ramsey, et al., 2008). Both types of valleys are very common along both limbs of the Aqra anticline (Fig. 5) indicating the lateral growth of the anticline.

Water and wind gaps are also excellent indications for the lateral growth of any fold in which these phenomena are developed (Ramsey, et al., 2008; Collignon, et al., 2016). At the Aqra anticline two WGs (Gulley Bakrman and Gulley Zanta) and one wind gap are developed (Fig. 6).

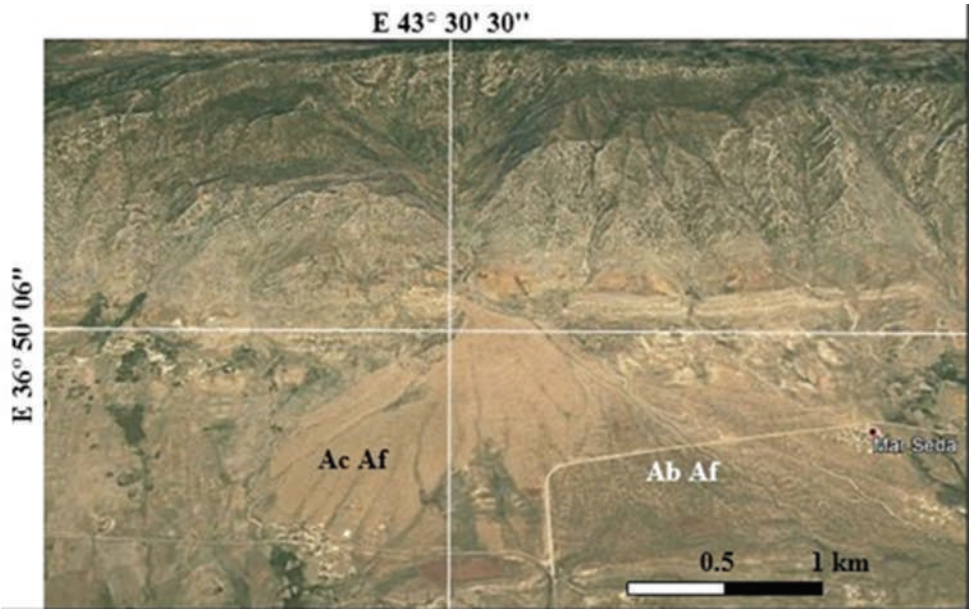

Fig. 3. Satellite image of an alluvial fan West of Aqra town. Abandoned alluvial fan (Ab Af) and an active alluvial fan (Ac Af).

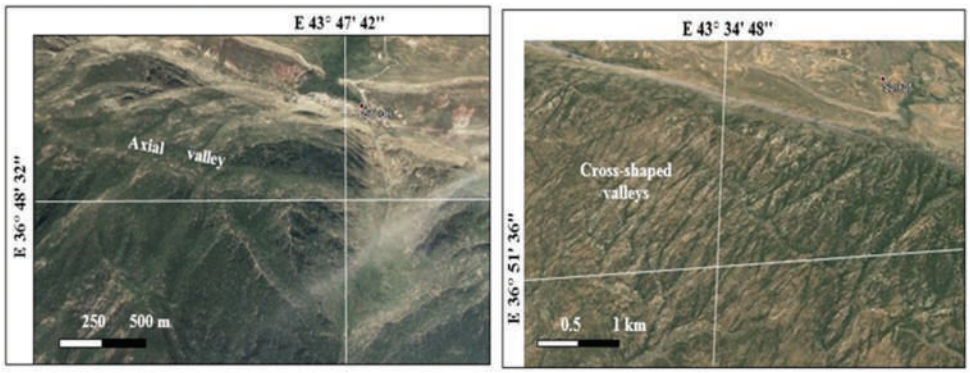

Fig. 4: (Left) Satellite image facing South. (Left) axial valley, (Right) cross-shaped valleys.

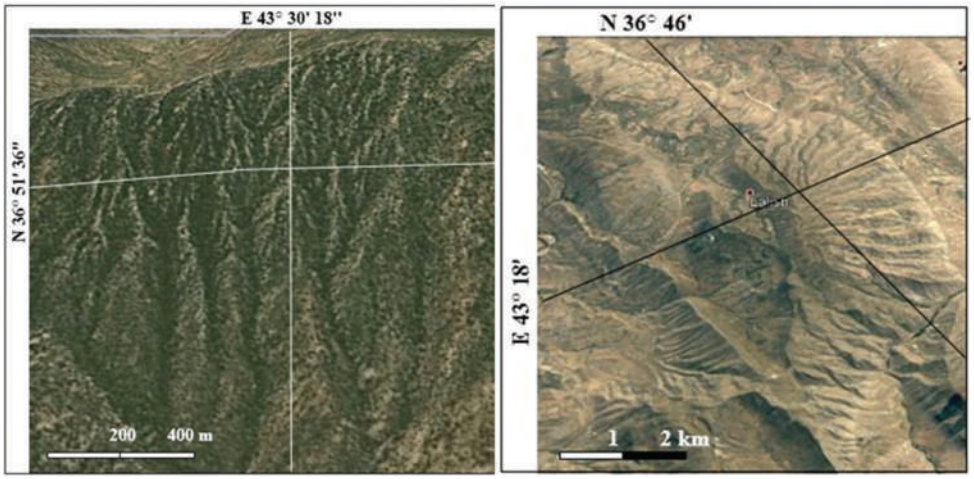

Fig. 5. (Left) Satellite image facing South showing fork-shaped valleys, (Right) Satellite image facing Southwest showing radial valleys.

En-echelon plunges of folds are also an indication for the lateral fold growth (Collignon, et al., 2016). The Aqra anticline is a doubly plunging anticline trending NW–SE. The Southeastern plunge with the Peris anticline is of en-echelon type (Fig. 7 Right). Whereas, the Northwestern plunge is highly complicated and faulted (Sissakian, et al., 2019); therefore, it is not so clear (Fig. 7 Left).

V. Discussion

Aqra anticline exhibits lateral growth mainly toward the Southeast as indicated by en-echelon plunging (Fig. 7, Right) as well as the presence of other indications; like abandoned alluvial fan (Fig. 3), axial valleys (Fig. 4, Left), cross-shaped valleys (Fig. 4, Right), fork-shaped valleys (Fig. 5, Left), radial valleys (Fig. 5, Right), and WGs (Fig. 6). The rate of stream incision is more than the growth rate of the Aqra anticline, as indicated by the presence of two WGs (Fig. 6). Moreover, the growth rate of the Peris anticline is more than that of the Aqra anticline as indicated from the en-echelon plunges, for both anticlines (Fig. 7, Right and Fig. 8). The Northwestern plunge of the Peris anticline is pushing more than that of Aqra anticline. This is indicated by the closure of the Northern part of a WG, which was present in the extreme Southeastern part of the Aqra anticline. The relic of the WG is present as a valley which is dissected into many parts. Formerly, it was flowing from A–B–C–D (Fig. 8). A landslide (near point A, Fig. 8) has blocked the entrance of the WG.

The continuous growth of the Peris anticline with a rate of more than that of the Aqra anticline is causing the blockage of the WG represented by Gulley Zanta (Fig. 6, Right and Fig. 8). Moreover, the small and low ridge (point E at Fig. 8) will disappear causing the merging of both valleys C–D and F–G. After the blockage of Gulley Zanta (WG, Fig. 8), the accumulated water in Nahleh Stream will start carving the previously existing WG, near the Northwestern plunge of the Peris anticline starting from point A (Fig. 8) and continue carving, to release the previously existing WG. However, this is controlled by the rate of the lateral growth of both anticlines and the incision rate of the streams, which depends mainly on the amount of rainfall and snowfall.

The Northwestern plunge of the Aqra anticline shows strange behavior exhibiting a wide coverage area, which is mainly covered by the carbonates of the Pila Spi Formation (Fig. 2). The exposures show dipping beds in different directions, hindering the normal shape of a plunging anticline. This is attributed most probably to the rate of upward growth and is more than the rate of the lateral growth. It is worth mentioning that the plunge area is highly deformed, faulted, and faces many adjacent anticlines (Northwest wards, North wards, and Southwest wards).

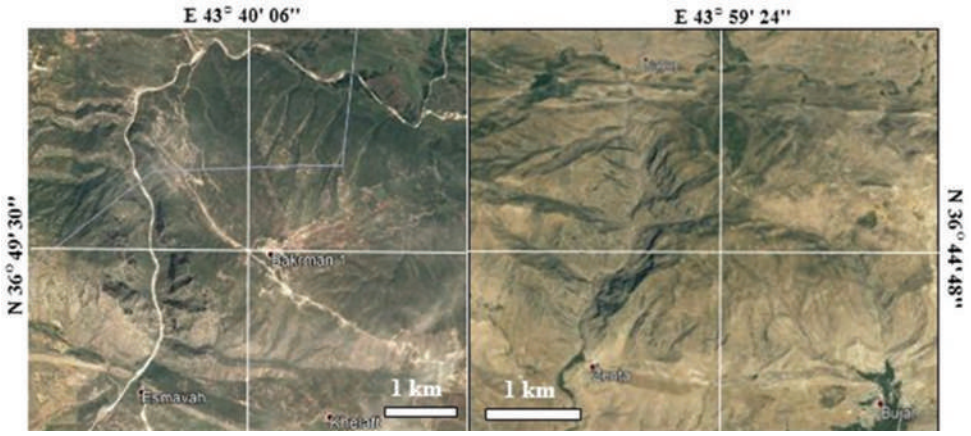

Fig. 6. Satellite image of two water gaps, (Left) Gully Bakrman, (Right) Gulley Zanta.

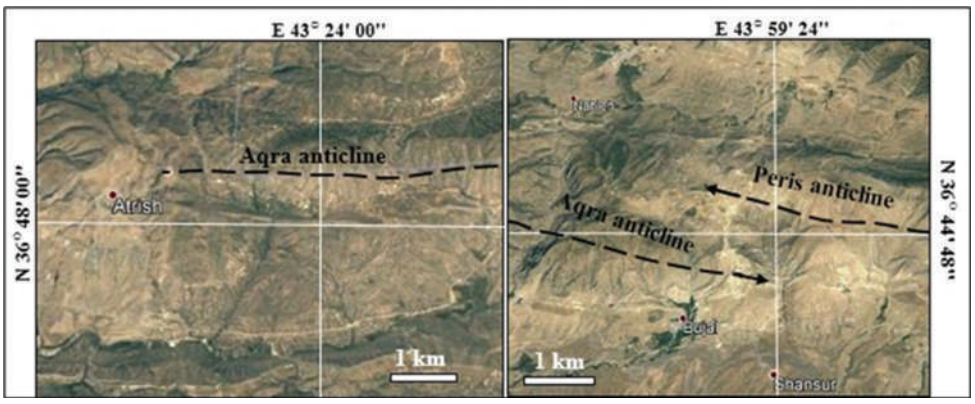

Fig. 7. Satellite image of Aqra anticline. (Left) The Northwestern plunge, note the complicated plunge due to faulting, (Right) En-echelon plunge of Aqra and Peris anticlines.

http://dx.doi.org/10.14500/aro.10535

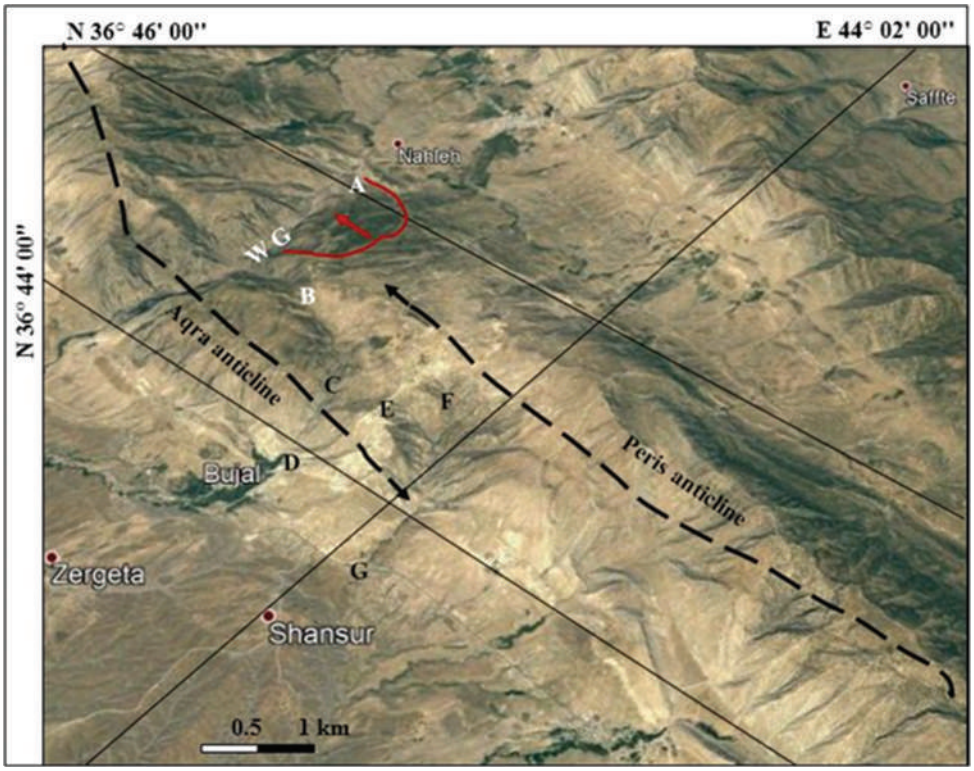

Fig. 8. Satellite image facing northeast, showing plunges of the Aqra and Peris anticlines.

VI. Conclusion

The Aqra anticline is exhibiting lateral growth toward the southeast, as indicated by many geomorphological features such as WGs, abandoned alluvial fan, cross-shaped valleys, radial valleys, axial valleys, and fork-shaped valleys. The rate of the incisions of the streams is more than the rate of the lateral growth of the anticline. However, the rate of the lateral growth of the Peris anticline is more than that of the Aqra anticline, which is pushing toward Northwest, and its continuous growth will cause the blockage of Galley Zanta. The Northwest plunge area exhibits abnormal forms of very wide outcrops of the Pila Spi Formation. The plunge area of Aqra anticline is highly deformed and hinders the normal plunge form.

VII. Acknowledgment

The authors express their thanks to the authorities of the University of Kurdistan-Hewler for presenting the required logistics for performing the current research.

References

Alavi, M., 2004. Regional stratigraphy of the zagros fold thrust belt of iran and its proforeland evolution. *American Journal of Science*, 304, pp.1-20.

Al-Kubaisi, M.S., and Abdul, J.M.F., 2015. Effect of lateral propagation of selected folds on streams, Sulaimaniyia Area, NE Iraq. *Iraqi Bulletin of Geology and Mining*, 11(1), p.95-124.

Allen, M., Jackson, J., and Walker, R., 2004. Late Cenozoic reorganisation of the Arabia Eurasia collision and the comparison of short-term and long-term deformation rates. *Tectonics*, 23, p.TC2008.

Alvarez, W., 1999, Drainage on evolving fold-thrust belts: A study of transverse canyons in the Apennines. *Basin Research*, 11, pp.267-284.

Bennett, E., Youngson, J., Jackson, J., Norris, R., Raisbeck, G., Yiou, F., and Fielding, E., 2005. Growth of South Rough Ridge, Central Otago, New Zealand: Using *in situ* cosmogenic isotopes and geomorphology to study an active, blind reverse fault. *Journal of Geophysics Researches*, 110, p.B02404.

Blanc, E.J.P., Allen, M.B., Inger, S., and Hassani, H., 2003. Structural styles in the Zagros simple folded zone, Iran. *Journal of Geological Society*, 160, pp.401-412.

Bretis, B., Bartl, N., and Graseman, B., 2011. Lateral fold growth and linkage in the Zagros fold and thrust belt (Kurdistan, NE Iraq). *Basin Research*, 23, pp. 615-630.

Burbank, D.W., and Anderson, R.S., 2001. *Tectonic Geomorphology*. Blackwell Science Malden, MA, USA.

Burbank, D.W., and Pinter, N., 1999. Landscape evolution: The interactions of tectonics and surface processes. *Basin Research*, 11, pp. 1-6.

Cannat, M., Rommevaux-Jestin, C., Sauter, D., Deplus, C., and Mendel, V., 1999. Formation of the axial relief at the very slow spreading Southwest Indian Ridge (49° to 69°E). *Journal of Geophysical Research: Solid Earth, American Geophysical Union*, 104(B10), pp.22825-22843.

Cartwright, J.A., Trudgill, B., and Mansfield, C.S., 1995. Fault growth by segment linkage: An explanation or scatter in maximum displacement and trace length data from the Canyon lands Grabens of SE Utah. *Journal of Structural Geology*, 17, pp.1319-1326.

Collignon, M., Yamato, P., Castelltort, S., and Boris, K.B., 2016. Modelling of wind gap formation and development of sedimentary basins during fold growth: Application to the Zagros Fold Belt, Iran. *Earth Surface Processes and Landforms*, 41(11), p.1521-1535.

Delcailleau, B., Carozza, J.M., and Laville. E., 2006. Recent fold growth and drainage development: The Janauri and Chandigarh anticlines in the Siwalik foothills, Northwest India. *Geomorphology*, 76, pp. 241-256.

Fouad, S.F., 2012. *Tectonic Map of Iraq, Scale 1: 1000 000*. 3rd ed. Iraq Geological Survey Publications, Baghdad, Iraq.

Keller, E.A., and Pinter, N., 2002. *Active Tectonics, Earthquakes, Uplift and Landscape*. 2nd ed. Prentice Hall, Upper Saddle River, pp.362.

Keller, E.A., Gurrola, L., and Tierney, T.E., 1999. Geomorphic criteria to determine direction of lateral propagation of reverse faulting and folding. *Geology*, 27(6), p.515-518.

Mosavi, E.J., and Arian, M., 2015. Tectonic geomorphology of Atrak River, NE Iran. *Open Journal of Geology*, 5, p.106-114.

Mumipour, M., and Najad H.T., 2011. Tectonic geomorphology setting of khayiz anticline derived from GIS processing, Zagros mountain, Iran. *Asian Journal of Earth Sciences*, 4(3), p.1711-1782.

Oberlander, T.M., 1985. Origin of drainage transverse to structures in orogens. In: Morisawa, M., Hack, J.T., editors. *Tectonic Geomorphology, the Binghampton Symposia in Geomorphology*. Vol. 15. Allen and Unwin, Boston. pp.155-182.

Ramsey, L.A, Walker, R,T., and Jackson, J., 2008. Fold evolution and drainage development in the Zagros Mountains of Fars Province, SE Iran. *Basin Research*, 20, pp.23-48.

Sissakian, V.K., 2010. Neotectonic movements in Darbandi Bazian Area, southwest of Sulaimaniyah city, NE Iraq. *Iraqi Bulletin of Geology and Mining*, 6(2), pp.57-69.

Sissakian, V.K., Ameen, R.M., and Mohammed, J.G., 2018. Lateral growth of qara dagh anticline, South of Sulaimaniyah city, NE Iraq: A structural geomorphological study. *Iraqi Bulletin of Geology and Mining*, 14(2), pp.9531-9547.

Sissakian, V.K., and Abdul-Jabbar, M.F., 2010. Morphometry and genesis of the main transversal gorges in North and Northeast Iraq. *Iraqi Bulletin of Geology and Mining*, 6(1), pp.95-120.

Sissakian, V.K., and Al-Jiburi, B.M., 2014. Stratigraphy. In: *Geology of the High Folded Zone*. Iraqi Bulletin of Geology and Mining, Iraqi. pp.73-161.

Sissakian, V.K., and Fouad, S.F., 2014. *Geological Map of Erbil Quadrangle, Scale 1: 250000*. 3rd ed. Iraq Geological Survey Publications, Baghdad, Iraq.

Sissakian, V.K., Fouad, S.F., Abdulhaq, H.A., and Omer, H.O., 2019. Geological *Map of Erbil and Mahabad Quadrangles, Scale 1: 250000*. 3rd ed. Iraq Geological Survey Publications, Baghdad, Iraq.

Sissakian, V.K., Kadhum, T.H., and Abdul Jab'bar, M.F., 2014. Geomorphology. In: *The Geology of the High Folded Zone*. Iraqi Bulletin of Geology and Mining, Iraqi. pp.7-56.

Skilodimou, H.D., Bathrellos, G.D., Maroukian, H., and Gaki-Papanastassiou, H.K., 2014. Late quaternary evolution of the lower reaches of ziliana stream in South Mt. Olympus (Greece). *Geografia Fisica e Dinamica Quaternaria*, 37(1), pp.43-50.

Vergés, J., 2007. Drainage responses to oblique and lateral thrust ramps: A review. In: Nichols, G., Paola, C., and Williams, E.A., editors. *Sedimentary Processes, Environments and Basins: A Tribute to Peter Friend*. International Association of Sedimentologists, Blackwell Publishing, Hoboken, New Jersey. pp.29-47.

http://dx.doi.org/10.14500/aro.10574

High-Performance Ultra-Compact Dual-Band Bandpass Filter for Global System for Mobile Communication-850/Global System for Mobile Communication-1900 Applications

Abbas Rezaei[1] and Salah I. Yahya[2,3]

[1]Department of Electrical Engineering, Kermanshah University of Technology, Kermanshah, Iran

[2]Department of Software Engineering, Faculty of Engineering, Koya University, Koya KOY45, Kurdistan Region – F.R. Iraq

[3]Department of Communication and Computer Engineering, Cihan University-Erbil, Erbil, Kurdistan Region – F.R. Iraq

***Abstract*—This work presents a novel microstrip dual-band bandpass filter (BPF) using meandros spirals and patch cells, which is proposed for the 1st time by this work. It occupies a very compact size of 0.0017 λg^2. The proposed filter is designed to operate at F_{o1} = 0.85 GHz and F_{o2} = 1.85 GHz for Global System for Mobile Communication (GSM)-850/GSM-1900 applications. In addition to the small size, it has several advantages in terms of wide fractional bandwidths, low insertion losses, and high return losses at both channels. The simulated insertion losses at the lower and upper passbands are 0.05 dB and 0.1 dB, respectively. Another advantage of the proposed BPF of this work is the attenuated harmonics, where it is able to suppress the 1st, 2nd, 3rd, and 4th harmonics (4.11 F_{o1}) with −20 dB maximum harmonic level.**

***Index Terms*—Bandpass, Compact, Dual band, Filter, Global system for mobile communications, Microstrip.**

I. Introduction

Due to having planar structures, microstrip filters are widely demanded by modern radiofrequency communication systems, especially small structures with high performance. With the development of multiband systems, dual-band bandpass filters (BPFs) are a must and commonly used. A well-designed microstrip filter must be compact with low loss and flat channels. Several structures have been utilized to obtain the microstrip dual-band BPFs (Hayati et al., 2012; Murmu and Das, 2015; Avinash and Rao, 2017; Hasan et al., 2017; Rezaei and Noori, 2017; Khani et al., 2019; Sarkar and Moyra, 2019). However, all of them are very large with high insertion losses. A microstrip circular ring (Murmu and Das, 2015), star-shaped structure (Avinash and Rao, 2017), folded stepped-impedance resonator and an etched ground structure (Sarkar and Moyra, 2019), coupled open-loop resonators (Hasan et al., 2017; Hayati et al., 2012; Rezaei and Noori, 2017), and bended microstrip lines, rectangular resonators, and stepped-impedance resonator (Khani et al., 2019) have been utilized to design dual-band BPFs. Eun and Lee (2017) proposed a novel method for designing dual-band BPF which consists of open-loop ring resonator and stepped-impedance resonator. Wen et al. (2018) designed a compact dual-band BPF using a pair of composite resonators. In Chen et al., 2018, novel dual-band BPF is proposed using a compact microstrip quint-mode multi-stub-loaded resonator. A high-performance filter must be able to attenuate the harmonics. Nevertheless, the proposed filters by Murmu and Das (2015), Avinash and Rao (2017), Sarkar and Moyra (2019), and Hayati et al. (2012) could not suppress the harmonics. Another important point of the filter design is creating flat passbands with low group delays (GDs). However, the designers Avinash and Rao (2017), Hasan et al. (2017); Khani et al., (2019); Hayati et al. (2012); Murmu and Das (2015); Rezaei and Noori (2017); and Sarkar and Moyra (2019) did not pay attention to this problem, whereas the reported filters by Sarkar and Moyra (2019); Hasan et al. (2017); Hayati et al. (2012); and Khani et al. (2019) have two narrow channels.

In this work, a microstrip dual-band BPF is proposed for global system for mobile communications (GSM), that is, GSM-850 and GSM-1900 (Personal Communications Service) which are used in most of North, South, and Central America. It is designed based on a novel compact structure. In comparison with the previous reported filters, our filter has

ARO-The Scientific Journal of Koya University
Volume VII, No.2 (2019), Article ID: ARO.10574, 4 pages
DOI: 10.14500/aro.10574
Received 20 October 2019; Accepted 27 November 2019
Regular research paper: Published 10 December 2019
Corresponding author's e-mail: a.rezaee@kut.ac.ir

the most compact size, the lowest insertion losses, and good return losses at both passbands. Meanwhile, it can attenuate the harmonics with a maximum harmonic level of −20 dB. Furthermore, the proposed dual-band BPF has two wide flat channels.

II. Filter Design and Structure

For designing a resonator, we need a structure with its *LC* equivalent circuit. To miniaturize the size, the spiral cells with inductance features are a good option because they can save the size totally. We know that the large width microstrip cells have capacitance features. Moreover, patch cells are compact with capacitance properties. On the other hand, the coupling between microstrip cells provides small capacitors (named as coupling capacitors). Accordingly, a combination of coupled spirals attached to filled microstrip cells would be a good choice. As a result, we select our proposed resonator as presented in Fig. 1a. An approximated equivalent *LC* model of the proposed resonator is presented in Fig. 1b, where the spiral cell is replaced by inductor L_s and patch feed lines are replaced by capacitors C_p. In this approximated model, we ignored the effect of steps since they are considered only at the frequencies higher than 10 GHz.

Some information about the resonator behavior can be extracted from the *ABCD* matrix. Therefore, at an angular frequency ω, the *ABCD* matrix of the proposed resonator is calculated as follows:

$$T=\begin{bmatrix} A & B \\ C & D \end{bmatrix}=\begin{bmatrix} 1 & \dfrac{2}{j\omega C_p}+j\omega L_s \\ 0 & 1 \end{bmatrix} \quad (1)$$

To decrease the loss, a perfect impedance matching is needed. If the reflection coefficient (Γ) becomes near zero, the matching will be improved. Therefore, the condition of perfect matching will be obtained as follows:

$$\Gamma=\frac{A+B-C-D}{A+B+C+D}=0\Rightarrow \frac{\dfrac{2}{j\omega_p}+j\omega_s}{\dfrac{2}{j\omega_p}+j\omega_s+2}=0\Rightarrow\omega=\sqrt{\frac{2}{L_sC_p}} \quad (2)$$

The perfect matching will be obtained at the angular resonance frequency ω. This frequency can be tuned in accordance with Equation (2) easily. Therefore, the resonance frequency is flexible by changing the values of L_s and C_p. From Equation (1), the input impedance of the proposed resonator is:

$$Zin=\frac{2-\omega^2C_pL_s}{j\omega_p} \quad (3)$$

Thus, it is a single-mode resonator with only a resonance frequency for Z_{in} = 0. For a pre-determined angular resonance frequency of ω, the proposed resonator can be miniaturized according to Equation (2) by choosing a small value for L_s. Fig. 2 depicts the layout configuration of our filter with its corresponding dimensions in mm. As shown in Fig. 2, the designed filter has a symmetric structure consisting of coupled spiral cells. To create additional capacitors, in some places, the width of the device is increased. When these capacitors are added to the inductors of the spiral structures, the passbands will be created.

III. Results and Discussion

The simulation results are obtained by the electromagnetic simulator of advanced design system software. To extract the simulation results, a dielectric substrate of RT/Duroid 5880 with ε_r = 2.2, h = 31 mil, and tanδ = 0.0009 is used. The proposed filter is well miniaturized with an overall size of 14.2 mm × 7.7 mm = 0.0017 λg^2, where λg is the guided wavelength calculated at 0.85 GHz. The simulated frequency response of the designed dual-band BPF is depicted in Fig. 3a. The results show that the first passband is from 0.69 GHz up to 1 GHz with an operational center frequency of F_{o1} = 0.85 GHz. The second resonance frequency is located at F_{o2} = 1.85 GHz with −3 dB cutoff frequencies of 1.75 GHz and 2 GHz. The introduced filter has two fractional bandwidths (FBWs) of FBW1 = 36% and FBW2 = 13.5% for the lower and upper passbands, respectively. The simulated insertion losses at the first and second passbands are 0.05 dB and 0.1 dB, respectively, whereas at both passbands, the return losses

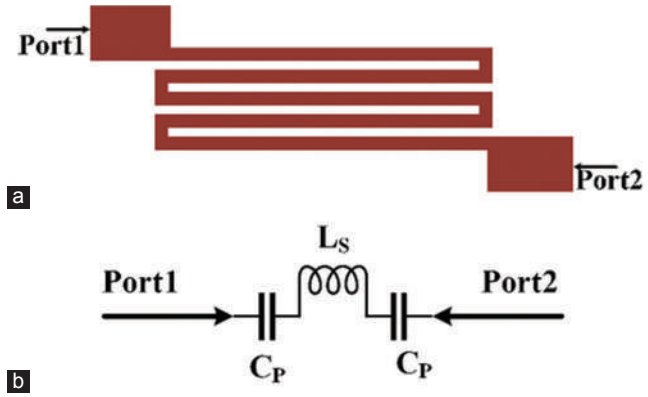

Fig. 1. Proposed resonator: (a) Layout, (b) approximated *LC* model.

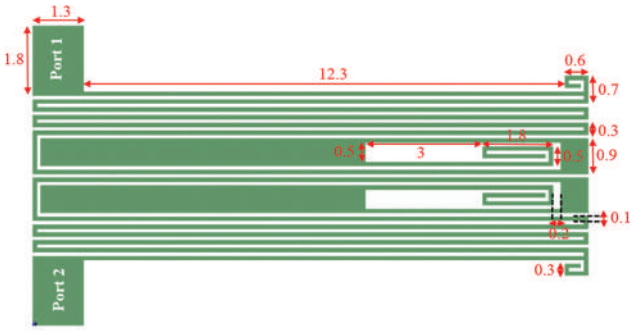

Fig. 2. Proposed bandpass filter.

http://dx.doi.org/10.14500/aro.10574

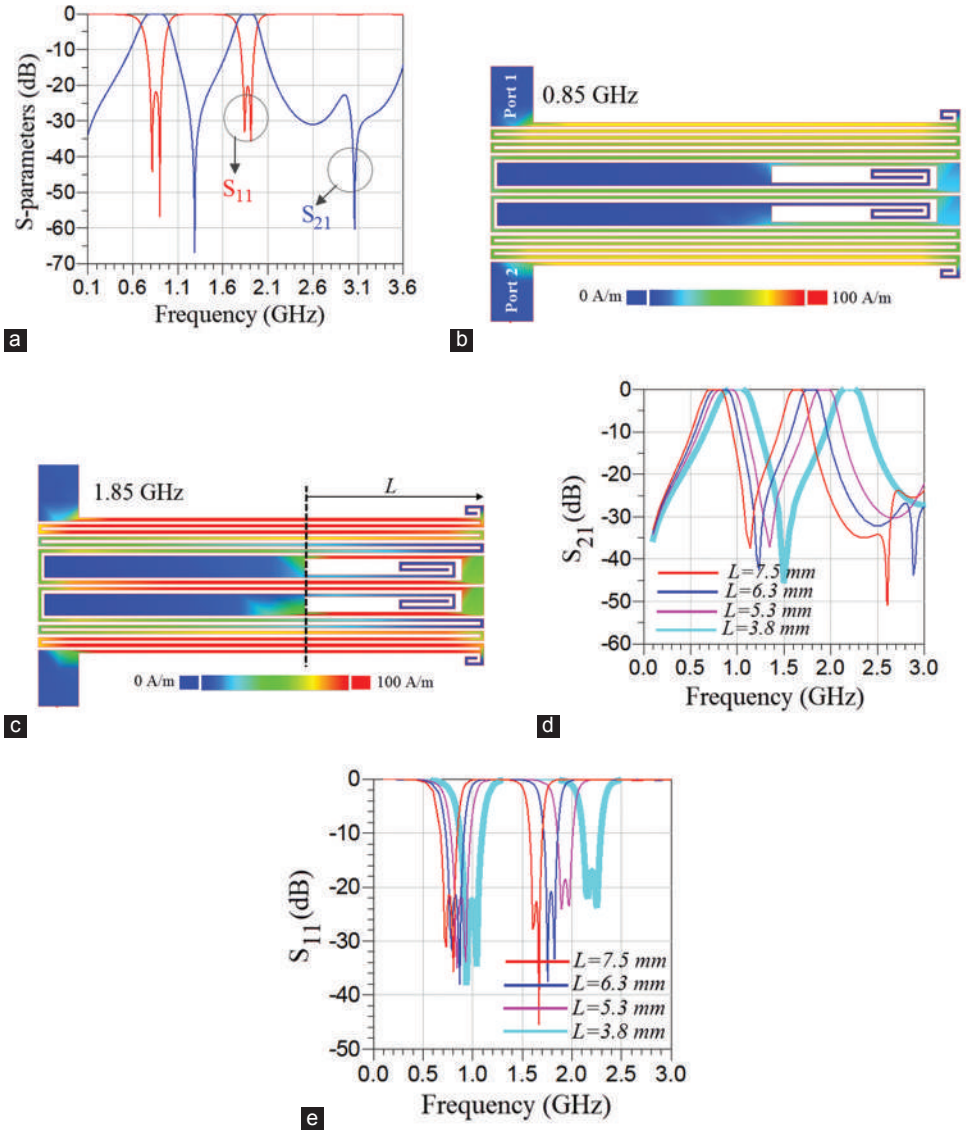

Fig. 3. (a) Frequency response of the designed dual-band bandpass filter, (b) Current density distribution at 0.85 GHz, (c) Current density distribution at 1.85 GHz, (d) S_{21} as a function of the physical length L, (e) S_{11} as a function of the physical length L.

TABLE I
COMPARISON BETWEEN THIS WORK AND PREVIOUS DUAL-BAND BANDPASS FILTERS (IL_1, IL_2: INSERTION LOSSES AT THE LOWER AND UPPER PASSBANDS, RL_1, RL_2: RETURN LOSSES AT THE LOWER AND UPPER PASSBANDS)

References	F_{o1}, F_{o2} (GHz)	IL_1, IL_2 (dB)	RL_1, RL_2 (dB)	FBW1%, FBW2%	Harmonic suppression	Size (λg^2)
This work	0.85, 1.85	0.05, 0.1	21.7, 20	36, 13.5	Up to 1.89 F_{o2}	0.0017
Murmu and Das,2015	2.38, 5.2	0.2, ---	19, ---	44, 15.3	No	---
Avinash and Rao, 2017	4.13, 4.26	1.78, 1.97	21, 27	7.26, 5.38	Up to 1.2 F_{o2}	---
Sarkar and Moyra, 2019	2.4, 3.5	0.7, 0.7	---	4.2, 2	Up to 1.7 F_{o2}	---
Hasan et al., 2017	2.4, 4.3	---	---	---	Up to 2.5 F_{o2}	0.096
Hayati et al., 2012	2.4, 5.2	0.53, 0.59	10, 13.4	---	Up to 1.7 F_{o2}	0.037
Rezaei and Noori, 2017	2.39, 5.7	0.1, 0.4	21.3, 16.6	10.8, 7.9	Up to 1.9 F_{o2}	0.025
Khani et al., 2019	3.6, 5.7	0.53, 0.67	25, 24.7	---	Up to 1.9 F_{o2}	0.02

FBW: Fractional bandwidth

are better than 20 dB. The proposed filter can attenuate the harmonics from the second passband to 3.5 GHz with −20 dB maximum harmonic level. Accordingly, it can suppress the harmonics up to 4.11 F_{o1} and 1.89 F_{o2}. Fig. 3b and c show the current density distribution of the proposed BPF at 0.85 GHz and 1.85 GHz, respectively. As shown in these figures, the length L is one of the most effective dimensions on the frequency response. The effect of physical length L on the frequency response is presented in Fig. 3d and e. As it can be seen, the resonance frequency is a function of the length L, whereby increasing the length L both resonance frequencies shift to the left.

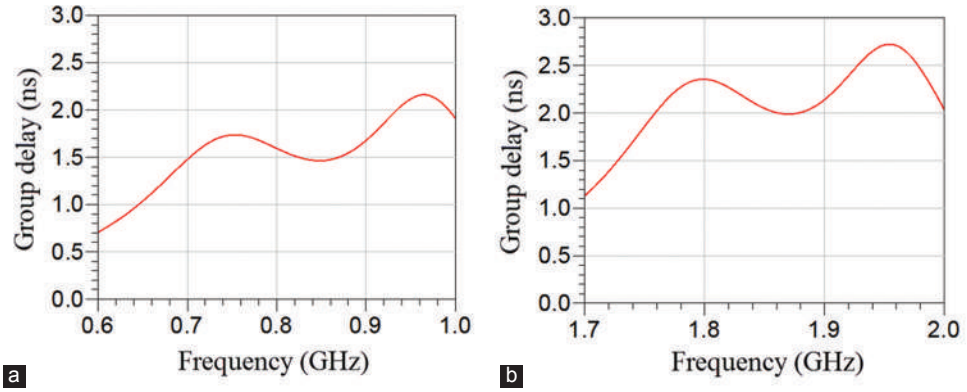

Fig. 4. Group delay of the designed dual-band bandpass filter at the (a) first passband, (b) second passband.

To show the advantages of this work, we compared the proposed BPF with the previous reported BPFs, as shown in Table I. As depicted in Table I, the lowest insertion losses and the most compact size are achieved by this work. On the other hand, in comparison with the previous works, the return losses, FBWs, and harmonic suppression are good. Only the proposed filter by Murmu and Das (2015) has wider bandwidths than the bandwidths of our proposed BPF. However, it could not attenuate harmonics.

The last important parameter in the filter design is the GD. A passband with high GD is subjected to time distortion. Despite this fact, the other reported filters mentioned in this work did not pay attention to this problem. The GD of the proposed filter at the lower and upper passbands is illustrated in Fig. 4a and b, respectively. As presented in these figures, the GDs at the first and second passbands are better than 2.2 ns and 2.7 ns, respectively.

IV. Conclusion

An ultra-compact microstrip dual-band BPF with an overall size of 0.0017 λg^2 is designed in this work. The proposed filter is suitable for GSM applications. The proposed design is based on a novel structure consisting of coupled spiral cells. Our introduced filter has two FBWs of 36% and 13.5% with the return losses better than 20 dB at both passbands. The other advantages of this work are the suppressed harmonics and the lowest insertion losses at both passbands. Altogether with the comparison, results show that our proposed filter has a high performance, the most compact size, and a novel structure.

References

Avinash, K.G., and Rao, I.S., 2017. Compact dual-mode microstrip bandpass filters with transmission zeros using modified star shaped resonator. *Progress in Electromagnetics Research C*, 71, pp.177-187.

Chen, C.F., Wang, G.Y., and Li, J.J., 2018. Compact microstrip dual-band bandpass filter and quad-channel diplexer based on quint-mode stub-loaded resonators. *IET Microwaves, Antennas and Propagation*, 12, pp.1913-1919.

Eun, J.W., and Lee, J.H., 2017. A microstrip dual-band bandpass filter using feed line with SIR. *IEICE Electronics Express*, 14, pp.1-8.

Hasan, M.F., Jalal, A.S., and Ahmed, E.S., 2017. Compact dual-band microstrip band pass filter design based on stub loaded resonator for wireless applications. In: *Progress in Electromagnetics Research Symposium-Spring (PIERS)*. IEEE, St Petersburg, Russia, pp.22-25.

Hayati, M., Noori, L., and Adinehvand, A., 2012. Compact dual-band bandpass filter using open loop resonator for multimode WLANs. *IET, Electronic Letters*, 48, pp.573-574.

Khani, S., Danaie, M., and Rezaei, P., 2019. Miniaturized microstrip dual-band bandpass filter with wide upper stop-band bandwidth. *Analog Integrated Circuits and Signal Processing*, 98, pp.367-376.

Murmu, L., and Das, S., 2015. A dual-band bandpass filter for 2.4 GHz bluetooth and 5.2 GHz WLAN applications. *Progress in Electromagnetics Research Letters*, 53, pp.65-70.

Rezaei, A., and Noori, L., 2017. Tunable microstrip dual-band bandpass filter for WLAN applications. *Turkish Journal of Electrical Engineering and Computer Sciences*, 25, pp.1388-1393.

Sarkar, D., and Moyra, T., 2019. A compact and high selective microstrip dual-band bandpass filter. *Progress in Advanced Computing and Intelligent Engineering*, 713, pp.475-481.

Wen, P., Ma, Z., Liu, H., Zhu, Sh., Ren, B., Wang, X., and Ohira, M., 2018. A miniaturized dual-band bandpass filter using composite resonators with flexible frequency ratio. *IEICE Electronics Express*, 15(5), pp.1-6.

 http://dx.doi.org/10.14500/aro.10538

Pollution Problems in Koya City due to Private Electrical Generators

Hayder H. Abbas, Fakhri H. Ibraheem and Ahmed A. Maaroof

Department of Chemical Engineering, Faculty of Engineering, Koya University,
Koya KOY45, Kurdistan Region – F.R. Iraq

***Abstract*— Koya city, like any other city in the world, faces a critical environmental problem which is global warming and the increase in the rate of production of gaseous pollutants. This research is involved with the negative effects of private Electrical Power Generators (EPGs) on the environment in Koya City. The environmental pollutants resulted from EPGs were investigated by performing an actual study on land for the number of (EPGs), types, and distribution. Koya city is divided into 18 quarters. The investigation covers a period from 2009 to 2017, included. The production of power was increased due to the increase in the number of generators and supplying hours. The power production in 2009 was 23,850 megawatt (MW) whereas it was 49,635 MW in 2017. The amount of fuel consumed in 2009–2017 was relatively increased from 30,000 to 62,500 barrel/year. The total amount of pollutants was increased by about 108% during the period 2009–2017. The results showed that the most significant increase in pollutants was carbon dioxide (CO_2). The annual amount of (CO_2) emitted in 2009 was 6588 tons whereas it has increased in 2017–13710 tons. The conclusion of this study was that the highest pollution occurred in the center of Koya City in Nabeel quarter, which represented 22% of the whole pollutants.**

***Index Terms* — Air pollution, Diesel power generator, Emission, Environment, Pollutants.**

I. Introduction

The current work was conducted to collect data on the number of private power generators that are in use in Koya city to estimate the type of pollutants, and to analyze the impact of their emission on the community. Koya city is one of the oldest districts in the Kurdistan region of Iraq. It is considered a bridge between the Governorate of Erbil and Sulemani. The city is surrounded by five sub-districts (Taq Taq, Shoresh, Ashti, Sktan, and Segrdkan) and it is located 620 m above sea level (Iraq, n.d.). In general, there are two means for supplying public electrical power to residential areas in both Iraq and Kurdistan region including Koya city. It is either supplied from national local public generators or by private generators. Many of the private generators are old and emit considerable amounts of hazardous pollutants. This study divides Koya city to 18 quarters, as shown in Fig. 1. The number of local generators in each district is different as a result of different population density in each quarter (Ali, et al., 2015). Electricity is a major requirement for sustainable development (Dorji, 2015).

The operational status of private generators varies depending on their lifetime and their degradation. Quantities and types of liberated polluting gases depend on the operational status of these generators and the quality of fuel used (Faiz, et al., 1995: Faiz, et al., 1996: Faiz, et al., 1997). The more efficient the burning process inside the generator chamber, the better power production is as well as the low quantities of liberated toxic gases, especially carbon monoxide (CO). Some generators use heavy and light diesel as fuel and some are depending on benzene. The generator which uses low fuel density liberates low amount of polluting gases. The amount of sulfur in fuel leads to a higher concentration of sulfur oxides (SO_x). The higher accumulated concentrations of polluting gases in limited areas like Koya City have a bad impact on the public health of people. The use of non-clean fuel increases the amount of carbon particulate in the environment which causes respiratory diseases. In general, the fuel specifications are not stable due to different suppliers. It is shown from the investigations that the use of light diesel oil is common. Estimation of the amount of pollutants depends on the standard fuel emission factor (EF) from the internal combustion engine (Criteria Air Pollutant and Greenhouse Gas Emission Factors, 2014).

The main pollutants' emissions from local electrical power generators (EPGs) are: Carbon dioxide (CO_2), CO, SO_x, nitrogen oxides (NO_x), carbon black (CB), and mass particulate (MP).

The controlling of the combustion process leads to minimize the emissions (Larsen, 1966: Krebs, 1971: Faiz, et al., 1995).

Globally, electrical power generation emits approximately 10 billion tons of CO_2 per year. Since the Industrial Revolution, the concentration of CO_2 in the atmosphere has risen by approximately 40% due to fossil fuel combustion. CO_2 has been declared a health risk to humans and scientific research indicates that it is the leading cause of climate change and rising temperatures on the planet (Spadaro, et al.,

ARO-The Scientific Journal of Koya University
Volume VII, No.2 (2019), Article ID: ARO.10538, 9 pages
DOI: 10.14500/aro.10538
Received 12 June 2019; Accepted 02 December 2019
Regular research paper: Published 20 December 2019
Corresponding author's e-mail: Ahmed.maaroof@koyauniversity.org

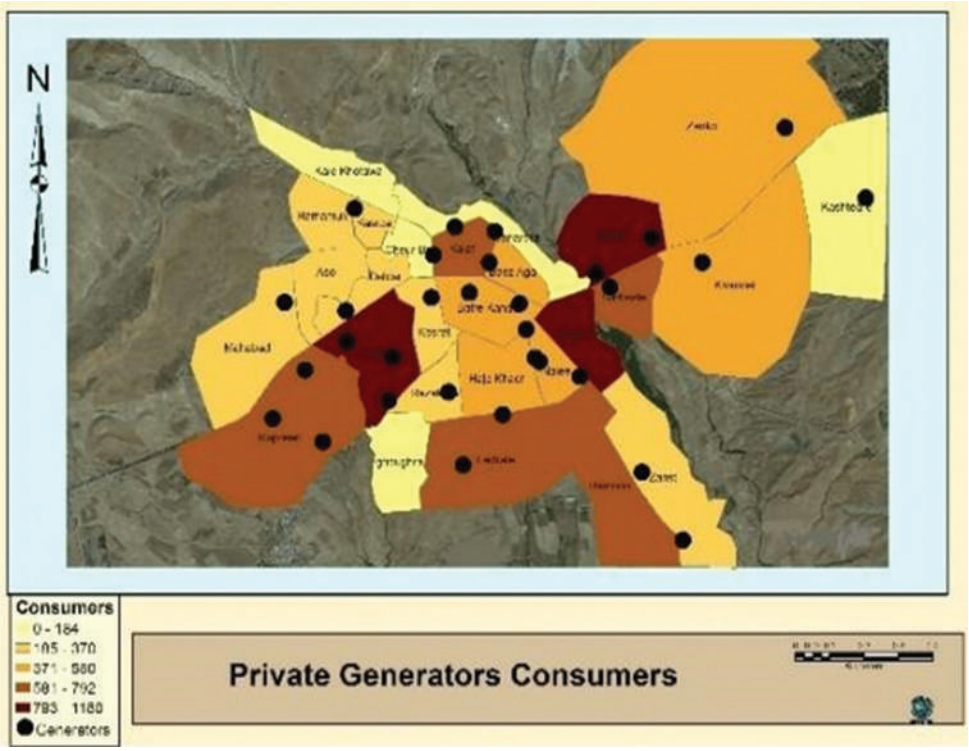

Fig. 1. Koya city quarters and the distribution of electrical diesel generators (Erbil Governorate, 2018).

2000: Mishra, 2004: Pulles and Appelman, 2008: Ou, et al., 2011).

The bad effect of emissions from burning fossil fuel on the environment is a big problem. For instance, inhalation of air containing high levels of sulfates in combination with certain other emissions can accelerate the probability of premature death. In combination with water, sulfur dioxide forms acids which have a corrosive effect on a variety of materials (Ball, and Frei, 1999: Rashad and Hammad, 2000: Holdren, et al., 2000: Baxter, 2001: Demin, 2002).

Pollution due to increasing numbers of power generators in Erbil, indicating an increase in the number of used generators by 76.1% for 10 years between 2003 and 2012 (Jassim, et al., 2013), whereas the pollutants amount due to electrical generators in whole of Iraq has doubled during the period from 2005 to 2014 (Jassim, et al., 2016).

II. EPGs in Koya City

The distribution of private generators across Koya quarters depends on their population, as shown in Table I. The amount of electrical power generation in Koya city has doubled during the period 2009–2016, according to Table II. The system of supplying power was modified gradually for the second half of 2016–12 h/day. In 2017, major of Koya quarters used the modified supplying system, which has led to increase the productivity, as shown in Fig. 2. The amount of fuel required to fulfill the extra operative hours was also increased to double, as shown in Fig. 3.

The power factor for the used generator is between 0.9 and 0.8; it is considered 0.8 due to the bad generator condition.

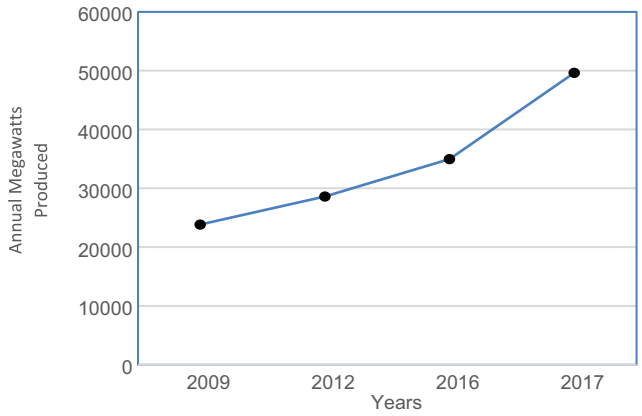

Fig. 2. Rate of increase of produced power during the period 2009–2017.

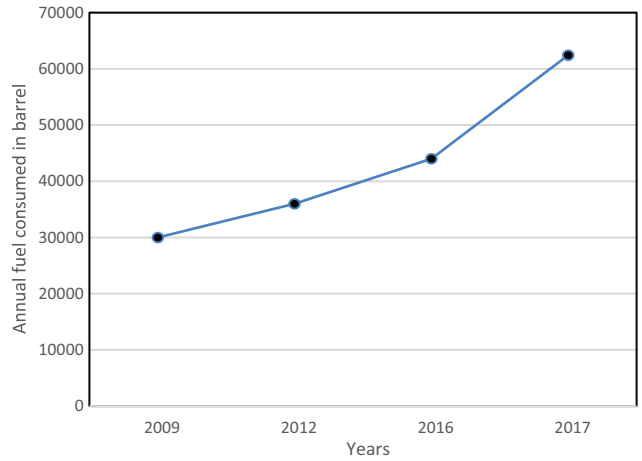

Fig. 3. Rate of increase of diesel fuel during the period 2009–2017.

 http://dx.doi.org/10.14500/aro.10538

Therefore, the total power produced in 2009 is 13920 × 0.8 = 11136 Kwt, and similarly for 2016 is 13762 Kwt. The generators in 2009 to mid-year 2016 are working 6 h/day, whereas it is increased gradually during the second half of 2016. In 2017, most of the generators were put on work for 12 h daily. The average fuel consumption is 0.2 l for each Kwt. Table II shows the annual power production in megawatt and the fuel consumption in barrel per year.

Fig. 2 shows the annual rate of increase of power in megawatt (MW). Fig. 3 shows the rate of increase of fuel demand.

TABLE I
Distribution of Power Generators Over Koya Quarters in 2009 and 2016

Quarter name	Generators in 2009			Generators in 2016		
	Number	Generator capacity KVA	Total KVA	Number	Generator capacity KVA	Total KVA
Mahabad	1	450	450	1	450	450
Deldar	1	250	250	1	250	250
Rapreen	1	250	550	1	350	1050
	2	150		2	350	
Kosrat	1	300	800	1	300	800
	2	250		2	250	
Kakon	1	250	1090	1	250	2540
	2	150		2	350	
	3	180		3	330	
	0	0		4	150	
Bafre	1	250	945	1	250	945
Kandel	2	250		2	250	
	3	65		3	65	
Razkare	1	300	300	1	300	300
Kasra	1	315	315	1	315	315
Faderale	1	500	1000	1	500	1000
	2	250		2	250	
Zinast	1	250	600	1	350	1950
	2	175		2	350	
	0	0		3	300	
Zanko	1	250	250	1	250	250
Khandel	1	275	275	1	275	275
Kashteary	1	250	250	1	250	250
Kalat	1	260	1610	1	260	1610
	2	300		2	300	
	3	250		3	250	
Azadi	1	500	1100	1	500	1100
	2	300		2	300	
Sarbaste	1	550	550	1	550	550
Nalee	1	192	3317	1	192	3317
	2	650		2	650	
	3	275		3	275	
	4	250		4	250	
Harmota	1	250	250	1	250	250
Total	52		13,920	59		17,202

TABLE II
Amount of Electrical Power Generation in Koya City through the Period 2009–2016 (Erbil Governorate, 2018)

Year	Power produced in MW	Fuel consumed in barrel/Year
2009	23850	30000
2012	28620	36000
2016	34984	44000
2017	49635	62434

MW: Megawatt

Fig. 4 shows the increase in demand of power distributed over Koya city quarters for the period from 2009 to 2017.

III. Pollutants' Emissions from EPGs

Several different rules regulate emissions criteria of pollutants and hazardous air pollutants (HAP) from fuel-burning systems. The applicability and specific emission limit in each regulation is generally a function of system thermal size (million British thermal units [MBTU] per hour) of heat input (MBTU/h) or MW of electricity output, fuel type, combustor design. A major source of HAP is defined as any stationary source or group of stationary sources located within a contiguous area. Most EF data were provided in units of pound (lb) of emissions per volume of fuel for gas or liquid fuels and in units of lb of emissions per ton of fuel for solid fuels. Lower heating values (LHVs) were used to convert these EF to a lb/MBTU basis. Table III shows the EF used for diesel fuel type based on LHV. The specification of diesel oil that is used to determine this EF is different from our diesel oil specification especially for sulfur content; it contains from 0.1% to 0.5%, whereas Iraqi diesel standard specification limit is high, it is 1% maximum for Grade A and 2.5% for Grade B. The actual EF in Koya city was determined according to actual sample tests.

More than 50 generators were investigated in this study; they were distributed over 18 quarters. The EF was estimated according to lb/MBTU (Criteria Air Pollutant and Greenhouse Gas Emission Factors, 2014). Each MBTU = 0.293 MW/H, therefore, it is easy to estimate the amount of MBTU produced for years 2009–2017. As a sample for estimation for 2009, the amount of power produced was 23850 MW, therefore the amount of MBTU produced = 23850/0.29 = 82241, and so on for other years. Table IV shows the amount of MBTU produced during the period 2009–2017.

The estimation of CO_2 pollutant in 2009, for example = 82241 MBTU × 176.6 (lb/MBTU) × (0.4536 (Kg/lb) /1000 (Kg/ton)) pollutant of CO_2 = 6536 tons, and so on for other pollutants.

TABLE III
Diesel – Fueled Turbine Emission Factors (lb/MBTU)

Pollutants	lb/MBTU
CO_2	176.6
NO_x	0.558
SO_2	0.1215
CO	0.00431
Particulates	0.534
CB	0.092

CO_2: Carbon dioxide, CO: Carbon monoxide, SO_2: Sulfur dioxide, CB: Carbon black, MBTU: Million British thermal units

TABLE IV
Amount of MBTU Produced through the Period 2009 –2017

Year	MBTU/Year
2009	82241
2012	98689
2016	120634
2017	171154

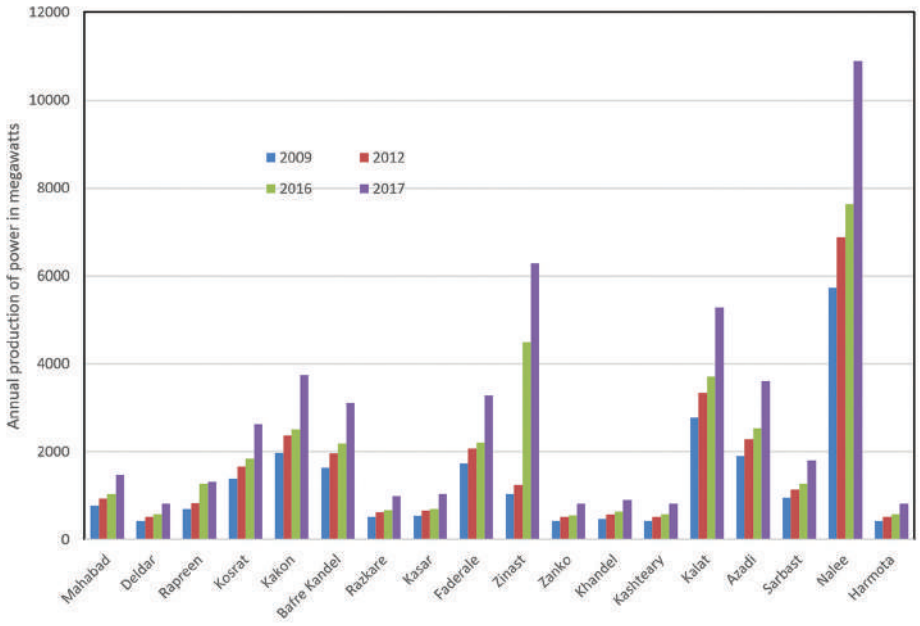

Fig. 4. Power produced in Koya city quarters through the period 2009–2017.

TABLE V
Diesel Oil Test Results

No.	Date	Sulfur content mass %	Specific gravity sp. gr.	Flash point (Closed Pensky-Martens) °C	Water content vol. %	Sediment content vol. %
1	January 17	0.6437	0.836	58	0.0053	0.0241
2		0.8791	0.826	58	0.009	0.0294
3		0.5547	0.815	55	0.0055	0.0265
4	February 17	0.8771	0.832	58	0.0066	0.0147
5		0.8619	0.83	57	0.0095	0.0103
6		0.6003	0.827	61	0.0073	0.0365
7		1.4614	0.823	46	0.0088	0.0317
8		0.7484	0.832	60	0.0073	0.0201
9		0.8665	0.835	60	0.0132	0.0337
10		0.8447	0.841	59	0.0044	0.0184
11	March 17	0.8243	0.836	62	49	0.021
12		0.879	0.839	58	0.0069	0.0197
13		0.7242	0.834	59	0.0044	0.0176
14		0.5659	0.819	52	0.0033	0.008
15		1.0303	0.837	58	0.0088	0.0044
16		0.5245	0.825	62	0.0027	0.0066
17		0.7893	0.822	61	0.0044	0.0057
18	April 17	1.0613	0.835	62	0.0033	0.009
19		0.7782	0.821	62	0.0055	0.0072
20		0.8532	0.822	60	0.0097	0.022
21	May 17	0.7721	0.82	60	0.0033	0.0115
22		0.5419	0.828	57	0.0046	0.0334
23		0.6382	0.825	58	0.0088	0.0232
24		0.7705	0.82	60	0.0088	0.0555
25	June 17	0.5608	0.824	60	0.0044	0.034
26		1.0129	0.831	61	0.0176	0.0414
27		0.8104	0.819	57	0.023	0.031
28		0.852	0.819	50	0.0084	0.0141
29	July 17	0.6414	0.812	58	0.0154	0.0147
30		0.6801	0.823	60	0.0044	0.0265
31		0.7003	0.814	63	0.0066	0.0088
32	August 17	0.6216	0.802	58	0.0144	0.0176
33		0.712	0.808	64	0.0066	0.0117
34		0.8437	0.811	58	0.0055	0.0066
Average		0.7802	0.825	58.59	0.0078	0.0205
Standard deviation		0.221	0.0074	3.9953	0.0026	0.0101

http://dx.doi.org/10.14500/aro.10538

IV. Practical Lab Tests Data

More than 30 samples of diesel fuel that is actually used in private electrical generators were tested. The samples distributed over 8 months from January 2017 to August 2017. The tests include sulfur content as mass percent, specific gravity, flash point to determine its burning efficiency, water, and sediment content as volume percent. Table V shows the test results.

The standard deviation (б) of the results shows that there is no big tolerance between the data through 8 months except flash point which it reaches about 4 and this is normal due to rough mixing the diesel by volatile material to improve burning efficiency. The complete fuel burning means oxidizing occurs to all pollutant elements such as sulfur, nitrogen, and carbon. The low value of б means the average value can be accepted as a real actual number.

TABLE VI
Annual Pollutants Emitted in Koya City through the Period 2009–2017

Year	CO_2 tons/year	NO_x tons/year	SO_2 tons/year	Particulates tons/year	CB tons/year	CO kg/year	Total
2009	6588	21	62.8	20	3.4	161	6695
2012	7906	25	75.4	24	4.1	193	8034
2016	9663	31	92.1	29	5.0	236	9821
2017	13710	43	130.7	41	7.1	335	13933

CO_2: Carbon dioxide, CO: Carbon monoxide, SO_2: Sulfur dioxide, CB: Carbon black

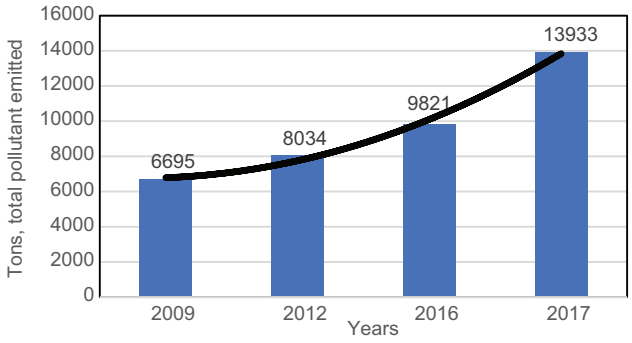

Fig. 5. Rate of increase of emitted pollutants in Koya city between 2009 and 2017.

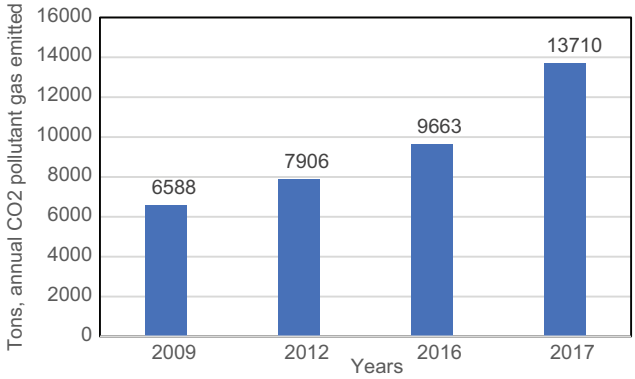

Fig. 6. Rate of increase of carbon dioxide pollutants emitted in tons during the period 2009–2017.

The equipment used for the tests are:

- X-ray sulfur meter, TANAKA, model RX-360 SH, energy dispersive X-ray fluorescence method, which is an accurate, non-destructive, economical and yet quick method prescribed in ISO 8754 and ASTM D4294-03
- Flash point by Pensky-Martens closed cup Automatic by TANAKA AGT 7 and manually
- Hydrometer set kit for determining the density
- Centrifugal separator, according to ASTM D1796, ASTM D4007 to determine water and sediment content and certified using high-precision separating funnel.

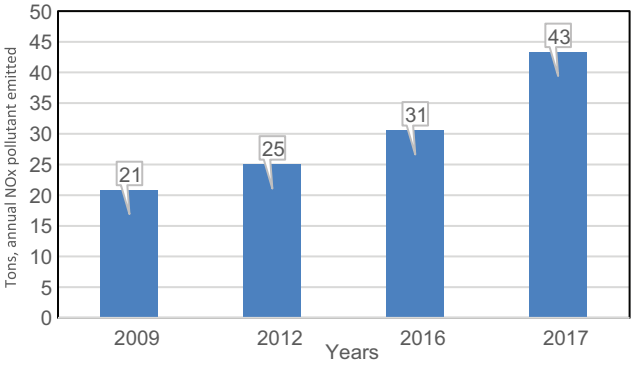

Fig. 7. Rate of increase of nitrogen oxides pollutants emitted in tons during the period 2009–2017.

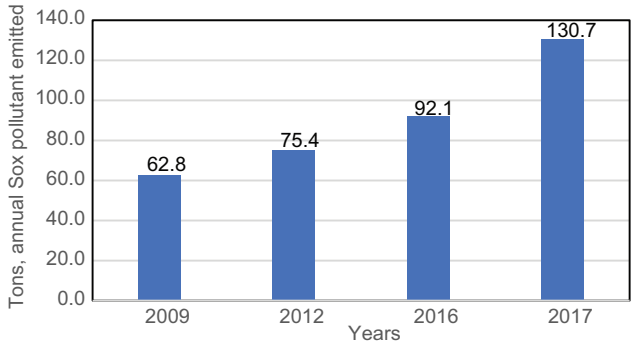

Fig. 8. Rate of increase of SO_2 pollutant emitted in tons during the period 2009–2017.

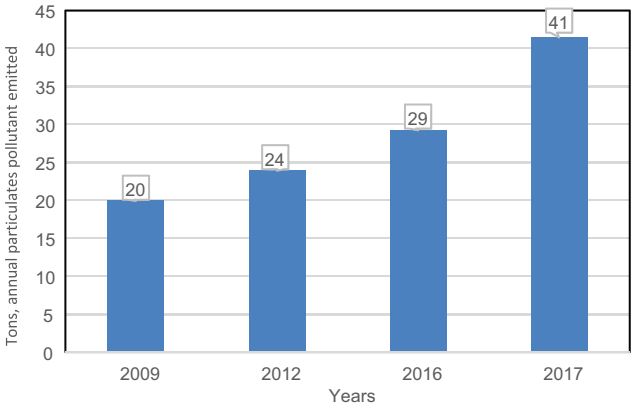

Fig. 9. Rate of increase of particulates emitted in tons during the period 2009–2017.

To determine the actual amount of SO_x liberated, consider the average value of sulfur content 0.7802% in 1-l fuel is combusted completely:

$S+O_2 \rightarrow SO_2$, which means one mole of sulfur (32 g atomic weight) reacted with 1 mole of oxygen (32 g molecular weight) to produce one mole of sulfur dioxide gas SO_2 (64 g of Sulfur dioxide).

The actual average fuel consumption in Koya generators are 0.2 l for 1 KWH.

It is known that each MBTU = 0.293 MW/h, therefore, to produce 0.29 MW/h (290 KW) in Koya city, it is required 0.2 × 290 = 58 l diesel fuel, which is equal to 58 × 0.825 (average sp. gr.) = 47.85 kg diesel fuel. The actual amount of sulfur in fuel = 47.85 × (0.7802/100) = 0.373 kg which is equal to 11.7 gmole. Most of the sulfur is oxidized to SO_2. Referring, to the chemical equation, 11.7 gmole of SO_2 is liberated which is equal to 749 g (1.684 lb); therefore, the actual EF value for SO_2 is 1.684 lb for each MBTU.

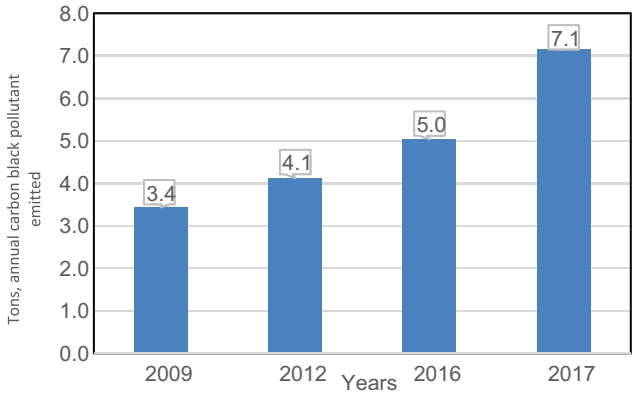

Fig. 10. Rate of increase of carbon black pollutant emitted in tons during the period 2009 – 2017.

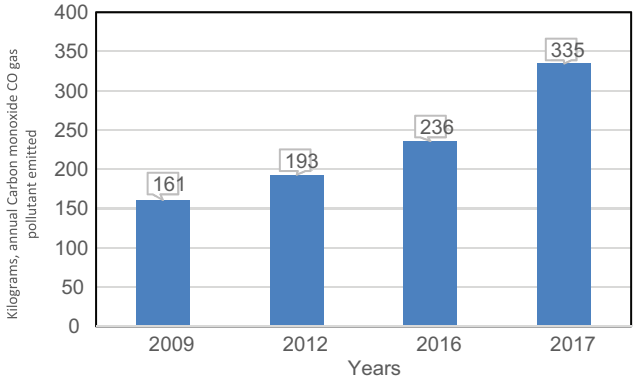

Fig. 11. Rate of increase of carbon monoxide poison gas pollutant emitted in kilograms during the period 2009–2017.

V. Main Contribution and Results

The amount of different kinds of pollutants emitted from local generators during the period 2009–2017 is shown in Table VI. It is clear that the pollutants' emissions were increased considerably since 2009 especially the CO_2 emissions, where it has jumped from 5452 tons in a year to more than a double in 2016, and in 2017 it reached 24,900 tons.

According to Fig. 5, the rate of pollutant emissions between 2009 and 2017 (9 years) is doubled. The amount of produced power was doubled compared to 2009.

Fig. 6 shows the rate of increase in the CO_2 during the 9 years. It has increased from 6588 to 13,710 tons, which represents 108%.

Fig. 7 shows the rate of increase in the NO_x during the 9 years. It has increased from 21 to 43 tons, which represents 105%.

Fig. 8 shows the rate of increase in SO_2 during the 9 years. It has increased from 21 to 43 tons, which represents 105%.

Fig. 9 shows the rate of increase of particulates pollutant emitted during the 9 years. It has increased from 62.8 to 130.7 tons, which represents 109%.

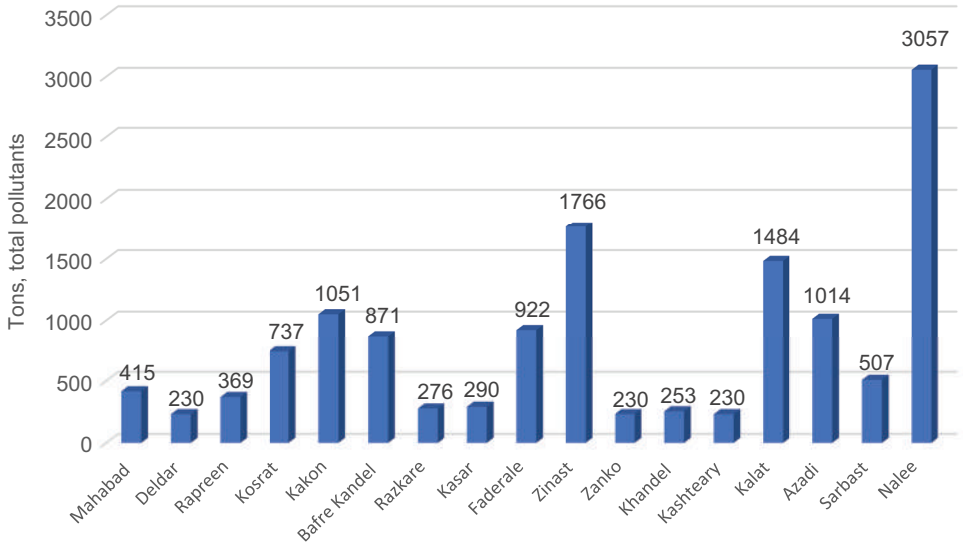

Fig. 12. Total pollutants amount in tons distributed over all quarters in 2017.

 http://dx.doi.org/10.14500/aro.10538

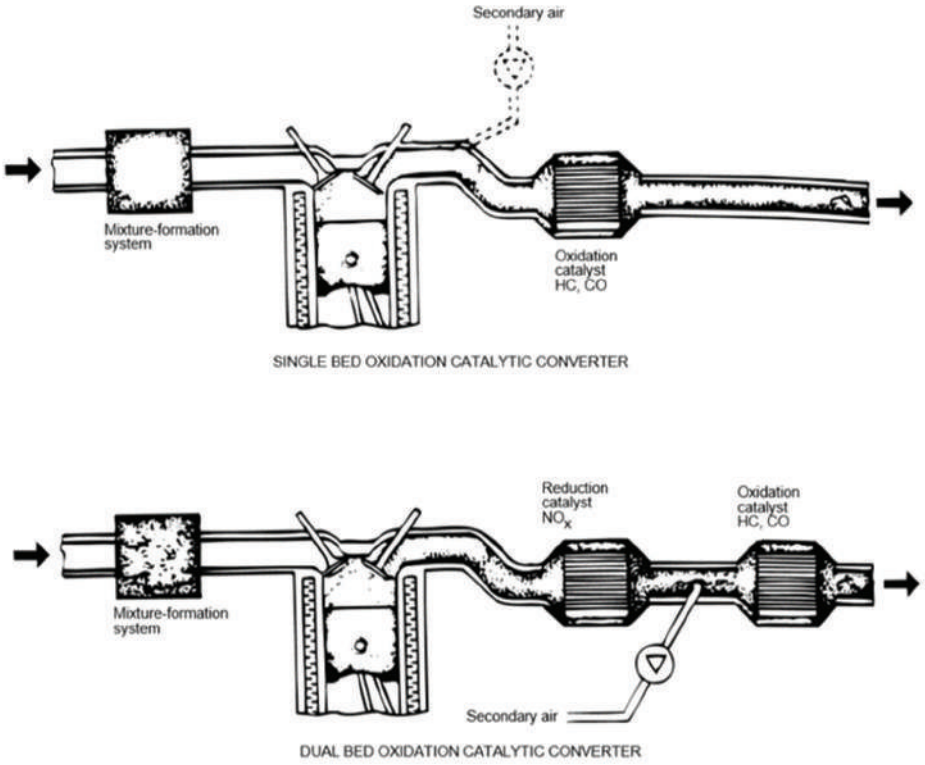

Fig. 13. Single and double bed oxidation catalytic convertor.

TABLE VII
Pollutants Amount Distribution Over Koya City Quarters in 2017

Quarter	MW	CO_2 tons/year	NO_x tons/year	SO_2 tons/year	Particulates tons/year	CB tons/year	CO kg/year	Total (tons/year)
Mahabad	1477	408	1.29	3.89	1.23	0.21	9.96	415
Deldar	821	227	0.72	2.16	0.69	0.12	5.53	230
Rapreen	1313	363	1.15	3.46	1.10	0.19	8.85	369
Kosrat	2627	726	2.29	6.92	2.19	0.38	17.71	737
Kakon	3743	1034	3.27	9.86	3.13	0.54	25.23	1051
Bafre Kandel	3103	857	2.71	8.17	2.59	0.45	20.92	871
Razkare	985	272	0.86	2.59	0.82	0.14	6.64	276
Kasar	1034	286	0.90	2.72	0.86	0.15	6.97	290
Faderale	3283	907	2.87	8.65	2.74	0.47	22.13	922
Zinast	6290	1737	5.49	16.57	5.25	0.91	42.40	1766
Zanko	821	227	0.72	2.16	0.69	0.12	5.53	230
Khandel	903	249	0.79	2.38	0.75	0.13	6.09	253
Kashteary	821	227	0.72	2.16	0.69	0.12	5.53	230
Kalat	5286	1460	4.61	13.92	4.42	0.76	35.63	1484
Azadi	3612	998	3.15	9.51	3.02	0.52	24.35	1014
Sarbast	1806	499	1.58	4.76	1.51	0.26	12.17	507
Nalee	10890	3008	9.50	28.69	9.10	1.57	73.42	3057
Harmota	821	227	0.72	2.16	0.69	0.12	5.53	230

MW: Megawatt, CO_2: Carbon dioxide, CO: Carbon monoxide, SO_2: Sulfur dioxide, CB: Carbon black

Fig. 10 shows the rate of increase of CB pollutants emitted during the 9 years. It has increased from 3.4 to 7.1 tons, which represents 109%.

Fig. 11 shows the rate of increase of CO poison gas emitted during the 9 years. It has increased from 161 to 335 kg, which represents 108%.

In 2017, the total amount of pollutants distributed over all Koya city quarters is shown in Fig. 12.

It is shown that the worst environmental condition is in Nalee, whereas the lowest pollutant is in Deldar, Zanko, and Kashteary. Table VII shows the amount of each pollutant distributed over all Koya city quarters in 2017.

VI. Conclusions

This research has come up with conclusions that the amount of electrical power produced has increased rapidly during the 9 years from 2009 to 2017. After midyear of 2016, a modified generator operating system was applied gradually

which lead to higher production. Most of the generators use diesel fuel. The power production in 2009 was 23,850 MW whereas it was 49,635 MW in 2017. The total amount of pollutants has increased rapidly as a result of the increase in the production of electrical energy. It was 6695 tons in 2009 whereas its increased to 13,933 tons in 2017, which is 108% increase. The amount of fuel consumed in 2009–2017 has relatively increased from 30,000 to 62,500 barrel/year. The amount of different pollutants was estimated according to EF from diesel internal combustion engines. The pollution rate can be graded into the following pollutants CO_2, NO_x, SO_2, CO, solid particulates, and CB. The percent of sulfur content in Iraqi diesel is 1% maximum for Grade A and 2.5% maximum for Grade B which is higher by 3–10 times than what is used in Europe (0.1% – 0.3%). The actual EF is depending on determining the SO_2 pollutant amount. CO_2 was the major pollutant due to its highest EF. The annual amount of (CO_2) emitted in 2009 was 6588 whereas it has increased in 2017–13,710 tons. The solid pollutants such as MP and CB annual amount have increased from 20 and 3.4 tons in 2009 to 41 and 7.1 tons in 2017, respectively. The gaseous pollutant such as NO_x, SO_x, and CO annual amount liberated has increased from 21 tons, 62.8 tons, and 161 kg in 2009 to 43 tons, 130.7 tons, and 335 kg in 2017, respectively. The area of distribution for pollutants can be categorized into three sectors. The highest one was in the center of Koya City (Nalee quarter) which represents 22% of the whole pollutants amount. The second sector includes the quarters that emitted about 10% of the whole pollutants amount such as Zinast and Kalat. The third sector includes the quarter that emitted not more than 7% of the whole pollutants amount.

VII. Recommendations

We can advise the following recommendations:

a. The physical types of pollutants that liberated from burning fuels are gases such as SO_x, NO_x, CO_x, and solid like carbon particulate. The electrostatic precipitator can capture the particles only to specified size, whereas the liberated gases amount can be reduced using single or dual bed oxidation catalytic converter, as shown in Fig. 13 (Faiz, et al., 1997)
b. The burning fuel gases pollutant and warming of the environment are global problems. International conferences in Paris 2014 and Poland 2019 have discussed this problem in details and some rules were agreed to put on in front of big industrial countries to stop gradually the activities that lead to pollutants. The alternative sources of energy such as solar, large capacity fuel cells stacks, and geothermal were encouraged by global loans
c. Starting effective collaboration between environmental protection organizations and involved directorates and academic persons to submit limits for exhaust pollutants. The monitoring of diesel oil properties is required to control fuel specification and pollutant content. Reducing the sulfur content by installing desulfurization unit in petroleum refinery factories
d. It is known that clean fuel liberates low pollutant amounts; therefore, a cooperation between the petroleum organizations and private sector are required to modify the generators or replaced them gradually to generators that are fueled by gas like liquefied petroleum gas instead of diesel fuel
e. Increasing the green areas inside Koya city, specially the populated ones, is important to enhance better environmental conditions.

References

Ali, J.A., Abbas, H.H. and Khodakarami, L., 2015. Gas pipeline network design for Koya city: Case study. *International Journal of Energy Engineering*, 5(2), pp.17-24.

Ball, D. and Frei, C., 1999. *Health and Environmental Impacts of Electricity Generation Systems*. International Atomic Energy Agency, Vienna, Austria.

Baxter, M., 2001. Health and environmental impacts of electricity generation systems: Procedures for comparative assessment: International atomic energy agency, technical reports series No. 394, IAEA, Vienna, December, 1999 (STI/DOC/010/394 TRS 394), 193pp., price 630 Austrian Schillings (45.78 EUR) paperback, ISBN 92-0-102999-3. *Journal of Environmental Radioactivity*, 1(53), pp.121-122.

Criteria Air Pollutant and Greenhouse Gas Emission Factors., 2014. Eastern Research Group for Incorporation in GREET. *Systems Assessment Group Energy Systems Division*. Argonne National Laboratory, Illinois.

Demin, V.F., 2002. Health and environmental impacts of electricity generation systems: Procedures for comparative assessments. *Atomnaya Tekhnika za Rubezhom*, 4, pp.16-19.

Dorji, G., 2015. *Environmental Aspect of Electric Energy Generation*. Available from: https://www.researchgate.net/publication/296672956_Environmental_aspect_of_electric_energy_generation. [Last accessed on 2019 Feb 23].

Faiz, A., Gautam, S. and Burki, E., 1995. Air pollution from motor vehicles: Issues and options for Latin American countries. *Science of the Total Environment*, 169(1-3), pp.303-310.

Faiz, A., Weaver, C.S. and Walsh, M.P., 1996. *Air Pollution from Motor Vehicles: Standards and Technologies for Controlling Emissions*. The World Bank, Washington, DC.

Faiz, A., Weaver, C.S., Walsh, M., Gautam, S. and Chan, L., 1997. *Air Pollution from Motor Vehicles: Standards and Technologies for Controlling Emissions* (No. WB-0554/XAB). World Bank Group, Washington, DC, United States.

Holdren, J.P., Smith, K.R., Kjellstrom, T., Streets, D., Wang, X. and Fischer, S., 2000. *Energy, the Environment and Health*. United Nations Development Program, New York.

Koysinjaq|Unbelievable Kurdistan-Official Tourism Site of Kurdistan. Available from: http://www.bot.gov.krd/erbil-province/koysinjaq. [Last accessed on 2018 Jan 14].

Jassim, H.M., Fakhri, H.I., Hayfaa, A.J., 2016. Environmental impact of electrical power generators in Iraq. *International Journal of Engineering Technology, Management and Applied Sciences*, 4(3), pp.122-134.

Jassim, H., Kurdi, Y.A.A. and Al-Nidai, F.H.I., 2013. Environmental issues in Erbil city. *International Journal of Engineering Trends and Technology*, 4(8), 3509-3515.

Krebs, L.J., 1971. *Method and Means to Control air Pollution from Motor Vehicles and Motor Vehicle Engines*. U.S. Patent, No. 3,618,314.

Larsen, R.I., 1966. Air pollution from motor vehicles. *Annals of the New York Academy of Sciences*, 136(12), pp.277-301.

Mishra, U.C., 2004. Environmental impact of coal industry and thermal power

plants in India. *Journal of Environmental Radioactivity*, 72(1-2), pp.35-40.

Ou, X., Xiaoyu, Y. and Zhang, X., 2011. Life-cycle energy consumption and greenhouse gas emissions for electricity generation and supply in China. *Applied Energy*, 88(1), pp.289-297.

Pulles, T. and Appelman, W., 2008. *Air Pollution from Electricity-generating Large Combustion Plants*. EEA Technical Report.

Rashad, S.M. and Hammad, F.H., 2000. Nuclear power and the environment: Comparative assessment of environmental and health impacts of electricity-generating systems. *Applied Energy*, 65(1-4), pp.211-229.

Spadaro, J.V., Langlois, L. and Hamilton, B., 2000. Greenhouse gas emissions of electricity generation chains: Assessing the difference. *IAEA Bulletin*, 42(2), pp.19-28.

Docking Study to Predict the Efficacy of Phosphatidylinositol 3-Kinase α Inhibitors

Mahmoud A. Chawsheen[1], Hazem A. Al-Bustany[2]

[1]Department of General Sciences, Faculty of Education, Soran University, Erbil, Kurdistan Region – F.R. Iraq

[2]Department of Basic Science, College of Medicine, Hawler Medical University, Erbil, Kurdistan Region – F.R. Iraq

***Abstract*—The phosphatidylinositol 3-kinase (PI3K) family comprises lipid kinases that cross-link signals between living cells and their surroundings. PI3Ks are classified into several groups and isoforms with specific characteristics and functions. Genes encoding PI3Ks are mutated in several types of cancer, and their isoforms have varying capacity in promoting cell signaling and cancer progression. Many compounds have been introduced as PI3Kα inhibitors, but not all of them have the same inhibitory effects. For successful PI3K-related biomedical experiments, it is vital to select the most specific and potent compounds with the highest inhibitory effects for targeting this kinase. In this study, we investigate 28 well-recognized PI3Kα inhibitors through predicting their specificity and potency using the docking software AutoDock Vina. Our data showed that PF 05212384 had the highest docking score (−9.2 kcal/mol), and 3-methyladenine had the lowest docking score (−4.8 kcal/mol). Our data also showed different types of interactions and bonds formed between the inhibitors and protein residues. In conclusion, PF 05212384 and AZD 6482 compounds are the best candidates for targeting PI3Kα. In addition to hydrophobic interactions in the PI3Kα binding pocket, the formation of hydrogen bonds between these inhibitors and binding pocket residues was confirmed.**

***Index Terms*—AutoDock Vina, Cancer cell, Cell signaling, Docking, Phosphatidylinositol 3-kinase, Phosphatidylinositol 3-kinase α.**

I. Introduction

The phosphatidylinositol 3-kinase (PI3K) family is a group of lipid kinases that interlink signals between living cells and their surroundings. These kinases affect downstream targets that modulate signaling pathways involved in cell proliferation, growth, survival, vesicle transport, cytoskeletal rearrangement, motility, and metabolism (Vivanco and Sawyers, 2002; Luo, et al., 2003; Engelman, et al., 2006; Liu, et al., 2009; Hancock, 2010). PI3Ks are activated in response to growth factors and cytokines through cell surface receptors (Peso, et al., 1997; Laurino, et al., 2005; Dudu, et al., 2012). After activation, PI3Ks generate phosphatidylinositol-3,4,5-trisphosphate (PIP3) through the addition of a phosphate group to phosphatidylinositol-4,5-bisphosphate (PIP2), and this process is an important step in initiating activation of their downstream targets (Whitman, et al., 1988; Auger, et al., 1989). Phosphatase and tensin homolog acts as a negative regulator of PI3K by dephosphorylating PIP3 to PIP2 (Chalhoub and Baker, 2009; Hollander, et al., 2011). Depending on the characteristics of their structure and specificity toward substrates, PI3Ks are classified into three groups: Class I PI3K, Class II PI3K, and Class III PI3K (Fruman, et al., 1998; Katso, et al., 2001). Class I, which we are mostly interested in, is subdivided into IA and IB. Class IA PI3Ks are heterodimers with the catalytic subunit p110 of one of the following isoforms: p110α, p110β, or p110δ. These isoforms are encoded by the PIK3CA, PIK3CB, and PIK3CD genes, respectively (Engelman, et al., 2006; Katso, et al., 2001). PI3K Class IA members also have the regulatory subunit p85 of the p85α, p55α, p50α, p85β, or p85γ isoform. The first three isoforms are encoded by PIK3R1 and are generated by differential splicing, and the last two isoforms are products of the PIK3R2 and PIK3R3 genes, respectively (Songyang, et al., 1993; Vanhaesebroeck, et al., 2001). Class IB PI3Ks are also heterodimers, but unlike Class IA, their catalytic subunit is the p110γ subunit integrated with regulatory isoforms p101 and p87. The p110γ subunit is encoded by the PIK3CG gene, and the p101 and p87 subunits are encoded by the PIK3R5 and PIK3R6 genes, respectively (Ueki, et al., 2002; Okkenhaug and Vanhaesebroeck, 2003; Amzel, et al., 2008). PIK3CA is frequently mutated in different types of cancer (Samuels and Waldman, 2010; Mangone, et al., 2012; Wang, et al., 2013; Schmidt, et al., 2018). Anomalies in p110α are associated with increased enzymatic activity of PI3K and promote oncogenesis in affected cells (Bader, et al., 2005; Echeverria, et al., 2015). Due to their roles in promoting cancer cell survival, transformation, proliferation, and migration, PI3Ks are considered promising targets in cancer therapy (Vivanco and Sawyers, 2002; Hausler, et al., 1998; Vanhaesebroeck, et al., 2010). Since different PI3K

ARO-The Scientific Journal of Koya University
Volume VII, No.2 (2019), Article ID: ARO.10565, 6 pages
DOI: 10.14500/aro.10565
Received 10 September 2019; Accepted 08 December 2019
Regular research paper: Published: 20 December 2019
Corresponding author's e-mail: mahmoud.hassan@soran.edu.iq

isoforms have diverse capacities in cellular signaling and cancer progression, applying inhibitors that target individual isoforms may produce better therapeutic outcomes in treating cancer (Vanhaesebroeck, et al., 2010: Wang, et al., 2015). Many compounds have been introduced as PI3Kα inhibitors, but not all of them have the same antitumor effects. It is convenient – especially for pre-clinical and clinical studies – to distinguish the most specific and potent chemical that delivers the highest inhibitory effect. Accordingly, in this study, we tried to uncover the best commercially available inhibitor(s) for targeting PI3Kα through predicting their specificity and potency using the docking software AutoDock Vina. This could help to improve treatment drugs in the future by cutting down the list of available ones to save more time, resources, and lives.

II. Computational Methods

A. Preparation of Phosphoinositide 3-kinase and Inhibitors

The crystal structure of PI3Kα was retrieved from the RCSB Protein Data Bank (PDB) with the code PDB-ID of 2RD0 (Gilliland, et al., 2000). There were four sections of missing residues in the 2RD0 crystal structure. Templates for the missing sections were adopted from the following PDB-ID entries: 3HHM, 3HIZ, 3ZIM, and 4JPS. All of the non-standard amino acid residues were removed separately from these structures, and PI3Kα was prepared as the receptor and the inhibitors as ligands using Discovery Studio 4.1 (Dassault Systèmes, 2010). The overall PI3K model was built by the homology modeling module with Modeller 19.9 (Sali and Blundell, 1993). Molecular Graphics Laboratory (MGL) Tools 1.5.6 were used to prepare the protein structure for molecular docking. Polar hydrogens were added to the protein structure and saved in the "PDBQT" file format (MGLTools, 2017). In the present study, a total of 28 PI3K inhibitors were investigated (Table I). The inhibitors were selected based on their specificity for PI3Kα and were obtained from the suppliers Tocris Bioscience (www.tocris.com) and Sigma-Aldrich (www.sigmaaldrich.com). They can also be tracked using their unique compound identification number through the PubChem website (https://pubchem.ncbi.nlm.nih.gov) (Kim, et al., 2019). Some of the two-dimensional (2D) structures were constructed by ChemDraw Pro 12.0 software and were saved in the "mol" file format (PerkinElmer, 2009). The 2D structures of the inhibitors were converted to three-dimensional structures using Discovery Studio 4.1. Finally, all of the structures were converted to the "PDBQT" file format with the Open Babel graphical user interface (O'Boyle, et al., 2011).

B. AutoDock Vina

The inhibitor docking site on PI3Kα was defined by establishing a cube that covered the area of the docking stage. The established cube was mainly defined through the manipulation of a colored box at the X, Y, and Z axes. The volume of the cube can be as large or as small as required; however, there is an exponential increase in computation time as the volume of the box increases. For this study, we used the dimensions of 25 Å × 25 Å × 25 Å to cover the inhibitor binding site with a grid point with 1.0 Å spacing and center grid boxes of 60.127, 62.455, and 114.509 in the X, Y and Z axes, respectively. Once the docking area was introduced, the coordinates of the grid box were written in a configuration file (a text document file) which fed into AutoDock Vina 1.1.2 software through a command line (Trott and Olson, 2010). The configuration file also specified the inhibitor (ligand) molecule and the PI3K (receptor) docking, and the broadness of the search can be set between 1 and 8, where 8 is the most comprehensive search. AutoDock Vina was run on the Microsoft Windows 8.1 operating system with four central processing units (1.7 GHz), and all PI3Kα inhibitors were docked into the PI3Kα (PDB-ID: 2RD0) protein (Trott and Olson, 2010). Three runs were performed for every single inhibitor.

III. Results

To validate our methodology, the PI3Kα protein structure (receptor) (PDB-ID: 2RD0) was matched with the PI3Kα isomers (ligands) (PDB-IDs: 3HHM, 3ZIM, 4FAD, and 4FA6)

TABLE I
List of Verified PI3Kα Inhibitors

S. No.	PI3Kα inhibitors	CID	S. No.	PI3Kα inhibitors	CID
1.	KWT (3HHM) (Mandelker, et al., 2009)	5288678	15	LTURM 36	122705988
2.	KKR (3ZIM) (Nacht, et al., 2013)	70699406	16	LY 294002 hydrochloride	11957589
3.	OTA (4FA6) (Le, et al., 2012)	59258964	17	LY 303511	3971
4.	0TB (4FAD) (Le, et al., 2012)	59259014	18	PF 04691502	25033539
5.	3-Methyladenine	135398661	19	PF 05212384	44516953
6.	A66	42636535	20	PI 103 hydrochloride	9884685
7.	AS 252424	11630874	21	PI 828	25181195
8.	AS 605240	5289247	22	PI 3065	24937012
9.	AZD 6482	44137675	23	PP 121	24905142
10.	BAG 956	24882589	24	Quercetin	5280343
11.	CZC 24832	42623951	25	STK16-IN-1	58525066
12.	ETP 45658	25229608	26	TG 100713	17751063
13.	GSK 1059615	23582824	27	TGX 221	9907093
14.	KU 0060648	11964036	28	Wortmannin	3003565

CID: Compound identification number, PI3K: Phosphatidylinositol 3-kinase

using the UCSF Chimera program version 1.10.1 (http://www.cgl.ucsf.edu/chimera/) (Pettersen, et al., 2004). The observed root-mean-square deviation values for these matchings were 0.904, 0.907, 1.174, and 1.174 Å, respectively (Fig. 1).

After successfully completing the docking protocol, the PI3Kα isomers described above were docked with the PI3Kα protein. Our data showed that different energy requirements were needed to perform successful docking. In this regard, KKR was the least energy-demanding chemical, and 0TA was the highest energy-demanding chemical (Table II).

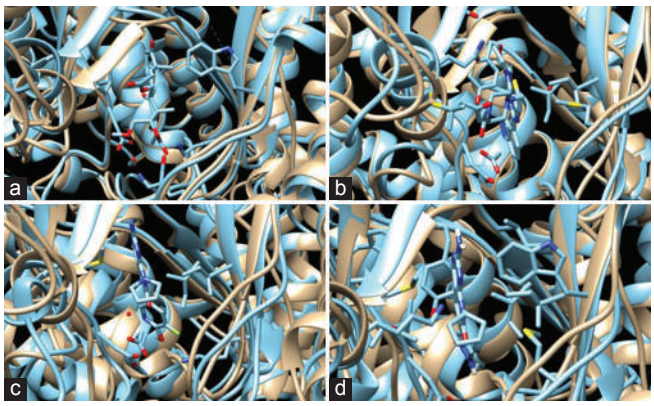

Fig. 1. (a-d) Superimposed structures of PI3Kα proteins and their root-mean-square deviation (RMSD) values for their matchings with PI3Kα protein. (a) 2RD0 (Gold) and 3HHM (Aqua) with RMSD: 0.904 Å; (b) 2RD0 (Gold) and 3ZIM (Aqua) with RMSD: 0.907 Å; (c) 2RD0 (Gold) and 4FAD (Aqua) with RMSD: 1.174 Å; (d) 2RD0 (Gold) and 4FA6 (Aqua) with RMSD: 1.174 Å.

TABLE II
Average Docking Scores of PI3Kα Isomers (Ligands) Docked to PI3Kα Protein

S. No.	PI3Kα inhibitor	1st run	2nd run	3rd run	Av.
1.	KKR	−8.3	−8.3	−8.4	−8.3
2.	KWT	−7.3	−7.3	−7.3	−7.3
3.	OTB	−7.2	−7.2	−7.2	−7.2
4.	0TA	−6.4	−6.4	−6.4	−6.4

PI3Kα: Phosphatidylinositol 3-kinase α

After that, each one of the remaining chemicals (24 inhibitors) was docked onto the PI3Kα protein. Docking scores (kcal/mol) for the inhibitors and the average of three runs were sorted from lowest-energy poses (maximum docked energy in negative) to highest-energy poses (minimum docked energy in negative), as shown in Table III. Our data revealed that the studied inhibitors exhibited different affinities toward the targeted protein. PF 05212384 gave the highest docking score (−9.2 kcal/mol), 3-methyladenine gave the lowest docking score (−4.8 kcal/mol), and the others placed between these two values (Tables III).

IV. Discussion

In this study, the type and potency of interactions between PI3Kα inhibitors and PI3Kα residues were predicted using the AutoDock Vina software. We used AutoDock Vina because it has been previously used in protein-ligand interactions and produced effective docking results (Perryman, et al., 2014: Jaghoori, et al., 2016). Inhibitors' orientation and their conformation were among the most important requirements to fulfill successful fitting between PI3Kα binding sites and the studied inhibitors. In this regard, optimal interactions and best docking scores were considered criteria to understand the fittest conformation among those generated by AutoDock Vina for the studied inhibitors.

The results of docking PI3Kα isomers with the PI3Kα protein recognized KKR as the most potent inhibitor compared with others that are recognized as typical PI3Kα inhibitors (Table II). During the docking of KKR into the PI3Kα binding site (Fig. 2), the formation of hydrogen bonds with SER802, LYS830, and GLN887 and carbon-hydrogen interactions with SER801 was observed. Hydrophobic interactions were also detected between the inhibitor and PI3Kα, causing alkyl interaction formation between protein residues MET800, MET886, VAL878, and MET950 and the inhibitor. The results obtained from the KKR-PI3Kα docking were used later on as a reference to choose the most potent and selective inhibitor(s) from the PI3Kα inhibitors list (Table III). When PF 05212384 docked into the PI3Kα binding site (Fig. 3), it formed

TABLE III
Docking Scores (kcal/mol) for Chemicals Recommended as PI3Kα Inhibitors. Data were obtained through AutoDock Vina 1.1.2 Software

S. No.	PI3Kα Inhibitor	1st run	2nd run	3rd run	Av.	S. No.	PI3Kα Inhibitor	1st run	2nd run	3rd run	Av.
1.	PF 05212384	−9.3	−9.0	−9.2	−9.2	15.	PI 103 hydrochloride	−7.3	−7.4	−7.3	−7.3
2.	AZD 6482	−8.4	−8.4	−8.3	−8.4	16.	LY 294002	−7.2	−7.3	−7.3	−7.3
3.	KKR	−8.3	−8.3	−8.4	−8.3	17.	OTB	−7.2	−7.2	−7.2	−7.2
4.	PI 3065	−8.1	−8.4	−8.2	−8.2	18.	Wortmannin	−7.1	−7.1	−7.1	−7.1
5.	GSK 1059615	−8.1	−8.1	−8.1	−8.1	19.	ETP 45654	−7.1	−7.0	−7.1	−7.1
6.	KU 0060648	−8.0	−8.0	−8.0	−8.0	20.	Quercetin	−7.0	−7.0	−7.0	−7.0
7.	AS 252424	−7.9	−7.9	−7.9	−7.9	21.	A66	−6.9	−6.9	−6.9	−6.9
8.	PP 121	−7.8	−7.8	−7.8	−7.8	22.	TGX 221	−6.9	−6.9	−6.9	−6.9
9.	CZC 24832	−7.8	−7.7	−7.7	−7.7	23.	LY 303511	−6.8	−6.8	−6.9	−6.8
10.	LTURM 36	−7.6	−7.6	−7.6	−7.6	24.	STK16-IN-1	−6.8	−6.8	−6.9	−6.8
11.	TG 100713	−7.6	−7.6	−7.6	−7.6	25.	PI 828	−6.7	−6.7	−6.7	−6.7
12.	AS 605240	−7.4	−7.4	−7.4	−7.4	26.	BAG 956	−6.4	−6.4	−6.4	−6.4
13.	PF 04691502	−7.6	−6.9	−7.6	−7.4	27.	0TA	−6.4	−6.4	−6.4	−6.4
14.	KWT	−7.3	−7.3	−7.3	−7.3	28.	3-Methyladenine	−4.8	−4.8	−4.8	−4.8

PI3Kα: Phosphatidylinositol 3-kinase α

http://dx.doi.org/10.14500/aro.10565

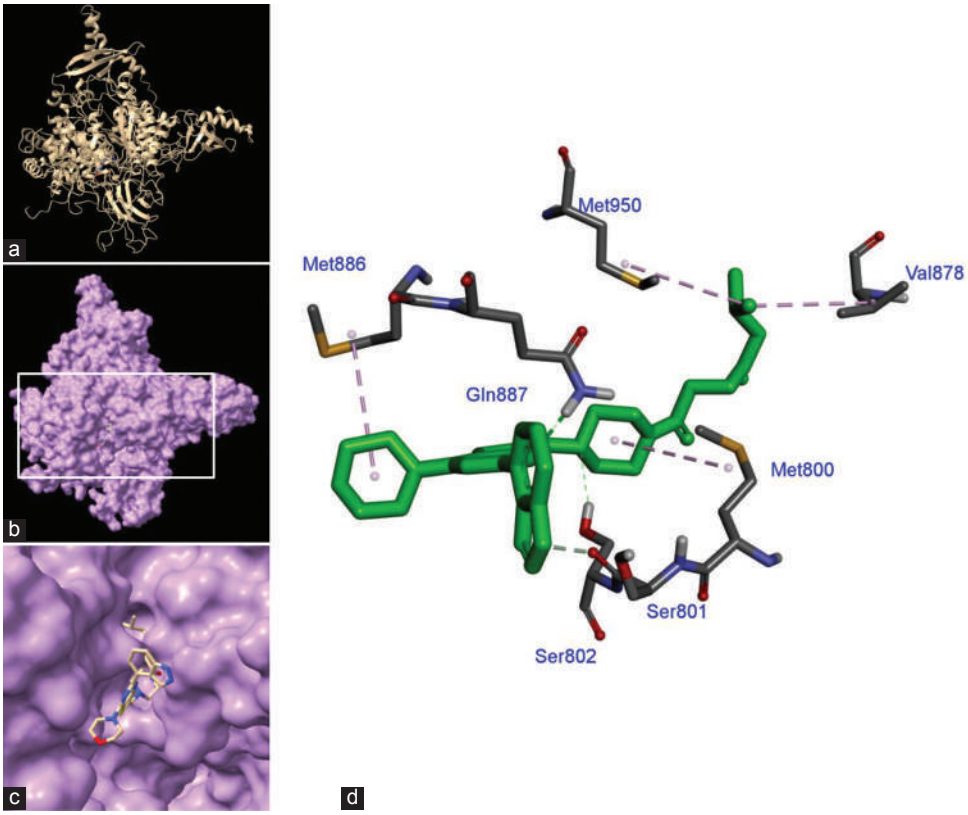

Fig. 2. KKR inhibitor docked to phosphatidylinositol 3-kinase α protein, (a) the protein as ribbons, (b and c) molecular surface and the inhibitor in active site, and (d) protein residues that interact with inhibitor.

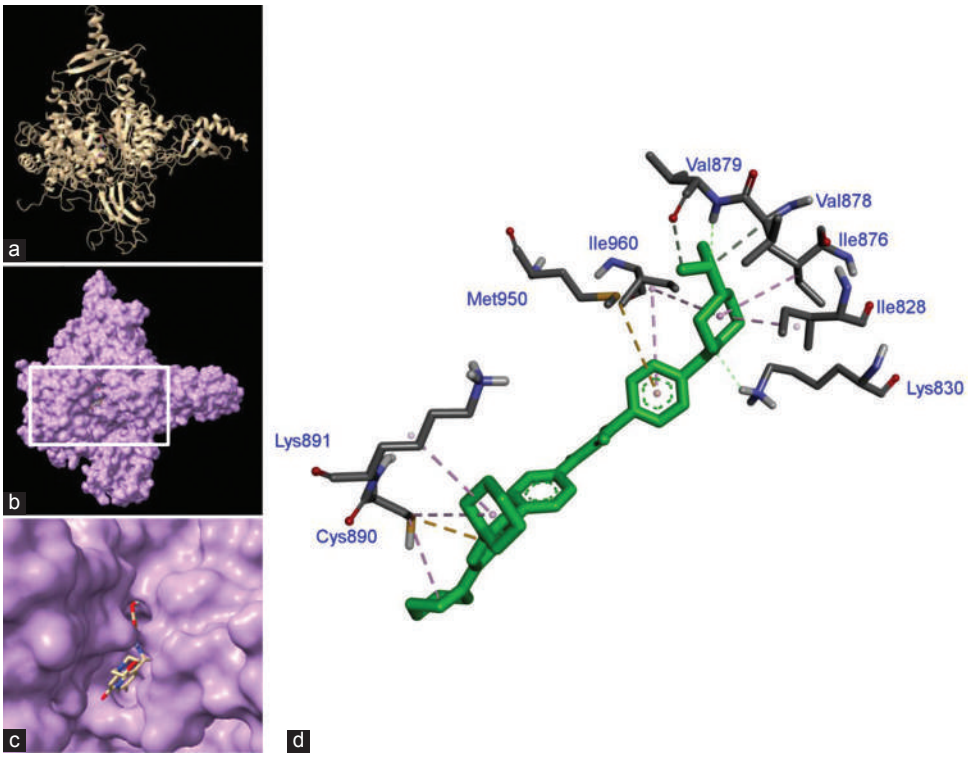

Fig. 3. Inhibitor PF 05212384 (19) docked with phosphatidylinositol 3-kinase α protein, (a) the protein as ribbons, (b and c) molecular surface and the inhibitor in active site, and (d) protein residues that interact with inhibitor.

hydrogen bonds with VAL879 and LYS830. Other non-bonded (pi-sulfur) interactions were formed between sulfur in CYS890 and MET950. Hydrophobic alkyl interactions were also observed between residues ILE828, ILE876, CYS890, LYS891, and ILE960 and the inhibitor. Moreover, a pi-alkyl interaction with ILE960 was also detected.

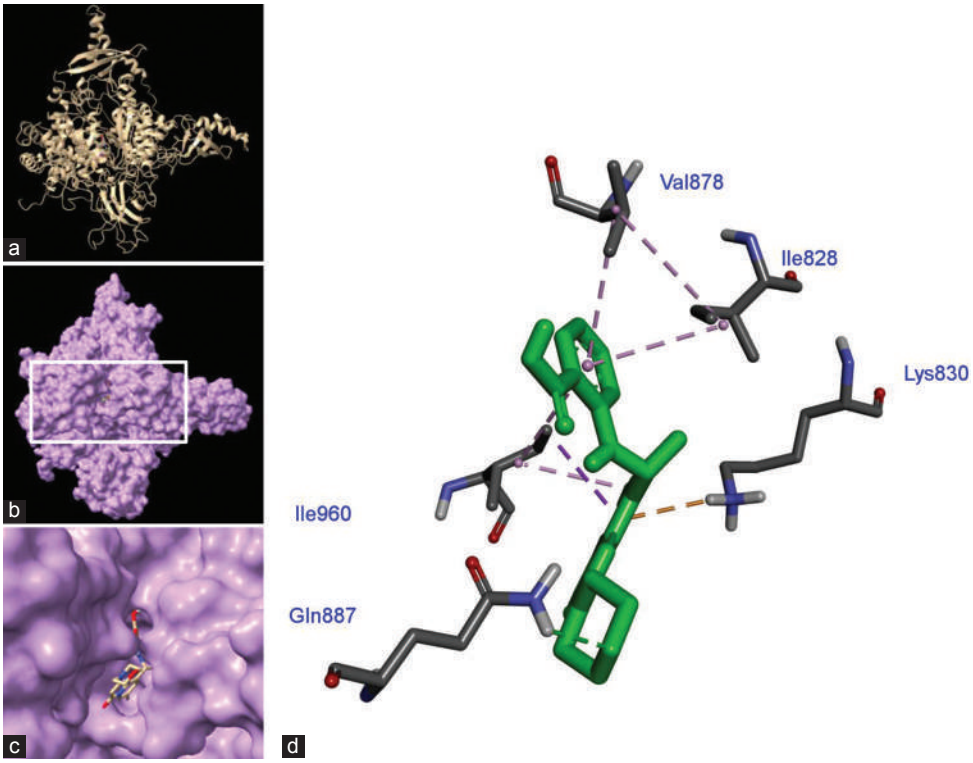

Fig. 4. Inhibitors AZD 6482 (9) docked to phosphatidylinositol 3-kinase α protein, (a) the protein as ribbons, (b and c) molecular surface and the inhibitor in active site, and (d) protein residues interacting residues with inhibitor.

Last but not the least, the inhibitor with the second lowest-energy pose was AZD 6482 (Fig. 4). This inhibitor formed hydrogen bonds with GLN887, an electrostatic interaction with LYS830, and hydrophobic interactions, including alkyl, pi-alkyl, and pi-sigma with ILE960 and pi-alkyl with ILE828 and VAL878.

Previously, other studies were carried out to predict the efficacy of PI3K inhibitors, but our results are not identical to theirs. This is more likely due to their use of different inhibitors and docking software (Sabbah, et al., 2010; Sabbah, et al., 2012; Singh and Bast, 2013; Kawade, et al., 2018).

V. Conclusions

Our analysis showed that among the studied PI3Kα inhibitors, the PF 05212384 and AZD 6482 compounds are the best candidates for targeting PI3Kα. Interaction studies also confirm that these inhibitors interact with PI3Kα by building hydrogen bonds with binding pocket residues in addition to hydrophobic interactions. *In vitro* and *in vivo* studies are needed to confirm our results in regard to the impact of candidate inhibitors on cancer cell survival and migration and their potential toxicity. It is also important to conduct molecular dynamic simulations to reach precise information regarding the dynamic behaviors and stability of the predicted complexes.

References

Amzel, L.M., Huang, C.H., Mandelker, D., Lengauer, C., Gabelli, S.B. and Vogelstein, B., 2008. Structural comparisons of class I phosphoinositide 3-kinases. *Nature Reviews Cancer*, 8(9), pp.665-669.

Auger, K.R., Serunian, L.A., Soltoff, S.P., Libby, P. and Cantley, L.C., 1989. PDGF-dependent tyrosine phosphorylation stimulates production of novel polyphosphoinositides in intact cells. *Cell*, 57(1), pp.167-175.

Bader, A.G., Kang, S., Zhao, L. and Vogt, P.K., 2005. Oncogenic PI3K deregulates transcription and translation. *Nature Reviews Cancer*, 5(12), pp.921-929.

Chalhoub, N. and Baker, S.J., 2009. PTEN and the PI3-Kinase Pathway in Cancer. *Annual Review of Pathology: Mechanisms of Disease*, 4(1), pp.127-150.

Dassault Systèmes., 2016. *Discovery Studio Modeling Environment* (*Version 4.1*). Dassault Systèmes, San Diego.

Dudu, V., Able, R.A. Jr., Rotari, V., Kong, Q. and Vazquez, M., 2012. Role of epidermal growth factor-triggered PI3K/Akt signaling in the migration of medulloblastoma-derived cells. *Cellular and Molecular Bioengineering*, 5(4), pp.502-413.

Echeverria, I., Liu, Y., Gabelli, S. B. and Amzel, L.M., 2015. Oncogenic mutations weaken the interactions that stabilize the p110alpha-p85alpha heterodimer in phosphatidylinositol 3-kinase alpha. *FEBS J*, 282(18), pp.3528-3542.

Engelman, J.A., Luo, J. and Cantley, L.C., 2006. The evolution of phosphatidylinositol 3-kinases as regulators of growth and metabolism. *Nature Reviews Genetics*, 7, p.606.

Fruman, D.A., Meyers, R.E. and Cantley, L.C., 1998. Phosphoinositide kinases. *Annual Review of Biochemistry*, 67, pp.481-507.

Gilliland, G., Berman, H.M., Weissig, H., Shindyalov, I.N., Westbrook, J., Bourne, P.E. and Feng, Z., 2000. The protein data bank. *Nucleic Acids Res*, 28(1), pp.235-242.

Hancock, J.T., 2010. *Cell Signalling*. 3rd ed. Oxford University Press, Oxford, New York.

Hausler, P., Papoff, G., Eramo, A., Reif, K., Cantrell, D.A. and Ruberti, G., 1998. Protection of CD95-mediated apoptosis by activation of phosphatidylinositide 3-kinase and protein kinase B. *European Journal of Immunology*, 28(1), pp.57-69.

Hollander, M.C., Blumenthal, G.M. and Dennis, P.A., 2011. PTEN loss in the continuum of common cancers, rare syndromes and mouse models. *Nature Reviews Cancer*, 11(4), pp.289-301.

Jaghoori, M.M., Bleijlevens, B. and Olabarriaga, S.D., 2016. 1001 Ways to run autodock vina for virtual screening. *Journal of Computer-Aided Molecular Design*, 30(3), pp.237-249.

Katso, R., Okkenhaug, K., Ahmadi, K., White, S., Timms, J. and Waterfield, M.D., 2001. Cellular function of phosphoinositide 3-kinases: Implications for development, homeostasis, and cancer. *Annual Review of Cell and Developmental Biology*, 17, pp.615-675.

Kawade, V.S., Satpute, P.S., Dhulap, S.A. and Gurjar, S., 2018. Therapeutic potential of PI3K/Akt/mTOR signalling pathway: Effective combination therapy for cancer. *Indian Journal of Pharmaceutical Sciences*, 80(4), pp.

Kim, S., Chen, J., Cheng, T., Gindulyte, A., He, J., He, S. and Bolton, E.E., 2019. PubChem 2019 update: Improved access to chemical data. *Nucleic Acids Res*, 47(D1), pp.D1102-D1109.

Laurino, L., Wang, X.X., de la Houssaye, B.A., Sosa, L., Dupraz, S., Cáceres, A., Quiroga, S., 2005. PI3K activation by IGF-1 is essential for the regulation of membrane expansion at the nerve growth cone. *Journal of Cell Science*, 118(16), pp.3653-3662.

Le, P.T., Cheng, H., Ninkovic, S., Plewe, M., Huang, X., Wang, H. and Zhang, E., 2012. Design and synthesis of a novel pyrrolidinyl pyrido pyrimidinone derivative as a potent inhibitor of PI3Kalpha and mTOR. *Bioorganic and Medicinal Chemistry Letters*, 22(15), pp.5098-5103.

Liu, P., Cheng, H., Roberts, T.M. and Zhao, J.J., 2009. Targeting the phosphoinositide 3-kinase pathway in cancer. *Nature Reviews Drug Discovery*, 8(8), pp.627-644.

Luo, J., Manning, B.D. and Cantley, L.C., 2003. Targeting the PI3K-Akt pathway in human cancer: Rationale and promise. *Cancer Cell*, 4(4), pp.257-262.

Mandelker, D., Gabelli, S.B., Schmidt-Kittler, O., Zhu, J., Cheong, I., Huang, C.H. and Amzel, L.M., 2009. A frequent kinase domain mutation that changes the interaction between PI3Kalpha and the membrane. *Proceedings of the National Academy of Sciences of the United States of America*, 106(40), pp.16996-17001.

Mangone, F.R., Bobrovnitchaia, I.G., Salaorni, S., Manuli, E. and Nagai, M.A., 2012. PIK3CA exon 20 mutations are associated with poor prognosis in breast cancer patients. *Clinics*, 67(11), pp.1285-1290.

MGLTools., 2017. *Molecular Graphics Laboratory Tools*. Available from: http://www.mgltools.scripps.edu. [Last accessed on 2017 Aug 01].

Nacht, M., Qiao, L., Sheets, M.P., St Martin, T., Labenski, M., Mazdiyasni, H. and Singh, J., 2013. Discovery of a potent and isoform-selective targeted covalent inhibitor of the lipid kinase PI3Kalpha. *Journal of Medicinal Chemistry*, 56(3), pp.712-721.

O'Boyle, N.M., Banck, M., James, C.A., Morley, C., Vandermeersch, T. and Hutchison, G.R., 2011. Open Babel: An open chemical toolbox. *Journal of Cheminformatics*, 3(1), p.33.

Okkenhaug, K. and Vanhaesebroeck, B., 2003. PI3K in lymphocyte development, differentiation and activation. *Nature Reviews Immunology*, 3, p.317.

PerkinElmer., 2009. *ChemDraw Professional*. Available from: http://www.cambridgesoft.com/Ensemble_for_Chemistry/ChemDraw/ChemDrawProfessional/Default.aspx. [Last accessed on 2017 Jul 01].

Perryman, A.L., Santiago, D.N., Forli, S., Santos-Martins, D. and Olson, A.J., 2014. Virtual screening with autodock vina and the common pharmacophore engine of a low diversity library of fragments and hits against the three allosteric sites of HIV integrase: Participation in the SAMPL4 protein ligand binding challenge. *Journal of Computer-Aided Molecular Design*, 28(4), pp.429-441.

Peso, L.D., González-García, M., Page, C., Herrera, R. and Nuñez, G., 1997. Interleukin-3-induced phosphorylation of BAD through the protein kinase akt. *Science*, 278(5338), pp.687-689.

Pettersen, E.F., Goddard, T.D., Huang, C.C., Couch, G.S., Greenblatt, D.M., Meng, E.C. and Ferrin, T.E., 2004. UCSF Chimera--a visualization system for exploratory research and analysis. *Journal of Computational Chemistry*, 25(13), pp.1605-1612.

Sabbah, D.A., Simms, N.A., Brattain, M.G., Vennerstrom, J.L. and Zhong, H., 2012. Biological evaluation and docking studies of recently identified inhibitors of phosphoinositide-3-kinases. *Bioorganic and Medicinal Chemistry Letters*, 22(2), pp.876-880.

Sabbah, D.A., Vennerstrom, J.L. and Zhong, H., 2010. Docking studies on isoform-specific inhibition of phosphoinositide-3-kinases. *Journal of Chemical Information and Modeling*, 50(10), pp.1887-1898.

Sali, A. and Blundell, T.L., 1993. Comparative protein modelling by satisfaction of spatial restraints. *Journal of Molecular Biology*, 234(3), pp.779-815.

Samuels, Y. and Waldman, T., 2010. Oncogenic mutations of PIK3CA in human cancers. *Current Topics in Microbiology and Immunology*, 347, pp.21-41.

Schmidt, H., Kulasinghe, A., Allcock, R.J.N., Tan, L.Y., Mokany, E., Kenny, L. and Punyadeera, C., 2018. A Pilot study to non-invasively track PIK3CA mutation in head and neck cancer. *Diagnostics*, 8(4), p.79.

Singh, P. and Bast, F., 2013. Multitargeted molecular docking study of plant-derived natural products on phosphoinositide-3 kinase pathway components. *Medicinal Chemistry Research*, 23(4), pp.1690-1700.

Songyang, Z., Shoelson, S.E., Chaudhuri, M., Gish, G., Pawson, T., Haser, W.G., King, F., Roberts, T., Ratnofsky, S. and Lechleider, R.J., 1993. SH2 domains recognize specific phosphopeptide sequences. *Cell*, 72(5), pp.767-778.

Trott, O. and Olson, A.J., 2010. Autodock vina: Improving the speed and accuracy of docking with a new scoring function, efficient optimization, and multithreading. *Journal of Computational Chemistry*, 31(2), pp.455-461.

Ueki, K., Fruman, D.A., Brachmann, S.M., Tseng, Y.H., Cantley, L.C. and Kahn, C.R., 2002. Molecular balance between the regulatory and catalytic subunits of phosphoinositide 3-kinase regulates cell signaling and survival. *Molecular and Cellular Biology*, 22(3), p.965.

Vanhaesebroeck, B., Leevers, S.J., Ahmadi, K., Timms, J., Katso, R., Driscoll, P.C. and Waterfield, M.D., 2001. Synthesis and function of 3-phosphorylated inositol lipids. *Annual Review of Biochemistry*, 70, pp.535-602.

Vanhaesebroeck, B., Vogt, P.K. and Rommel, C., 2010. PI3K: From the bench to the clinic and back. *Current Topics in Microbiology and Immunology*, 347, pp.1-19.

Vivanco, I. and Sawyers, C.L., 2002. The phosphatidylinositol 3-kinase AKT pathway in human cancer. *Nature Reviews Cancer*, 2(7), pp.489-501.

Wang, W.F., Xie, Y., Zhou, Z.H., Qin, Z.H., Wu, J.C. and He, J.K., 2013. PIK3CA hypomethylation plays a key role in activation of the PI3K/AKT pathway in esophageal cancer in Chinese patients. *Acta Pharmacologica Sinica*, 34(12), pp.1560-1567.

Wang, X., Ding, J. and Meng, L.H., 2015. PI3K isoform-selective inhibitors: Next-generation targeted cancer therapies. *Acta Pharmacologica Sinica*, 36(10), pp.1170-1176.

Whitman, M., Downes, C.P., Keeler, M., Keller, T. and Cantley, L., 1988. Type I phosphatidylinositol kinase makes a novel inositol phospholipid, phosphatidylinositol-3-phosphate. *Nature*, 332(6165), pp.644-646.

Education Needs to Support Architecture, Engineering, and Construction Collaboration Using Building Information Modeling

Dilan M. Rostam

Department of Architectural Engineering, Faculty of Engineering, Koya University,
Kurdistan Region - F.R. Iraq

***Abstract*—Projects in the construction industry involve multidisciplinary collaboration between the disciplines of architecture, engineering, and construction (AEC), and others. Conventionally, the collaboration between these disciplines relied on the recurrent exchange of relevant drawings and documents. Building information modeling (BIM) as a model-based process has given AEC professionals the tools to more efficiently plan, design, construct, and manage buildings and infrastructure. Yet the AEC industry has been reluctant in fully adopting the BIM as a single standard. This study explores and identifies the bottlenecks in adopting BIM as a single product lifecycle standard in the construction industry and advise on educating new engineers to become the generation to use a virtual collaborative working space covering the entire building lifecycle. Two conducted surveys targeting the AEC academia and industry revealed the needs for multilevel cross-disciplinary interactive collaborative BIM process modeling, and skilled workforce to increase the graduates' marketability and BIM adaptability. It is concluded that the new age collaborative culture requires new generation of AEC players that are enabled to work on a shared virtual product model supported by proactive BIM skills learned through undergraduate programs.**

***Index Terms*—Architecture; engineering; and construction collaboration, Building information modeling, Building lifecycle, Education, Integrated design.**

I. Introduction

Population is increasingly choosing concentrated urbanism where the demand for various services is growing exponentially to accommodate life. Sustainable cost-effective buildings with longer lifespan are at the center of these services. In response to these, the construction industry has adopted various measures such as rapid industrial building techniques. It is evident that such techniques have been commonly used in manufacturing industries for decades. However, the use of industrialized construction is also expanding in the architecture, engineering, and construction (AEC) industry in the form of building information modeling (BIM) to improve planning, design, construction, and collaboration for increased sustainability, lower costs, and broader safety throughout the lifecycle (Dassault Systèmes, 2014).

The US National BIM Standard defines BIM as a "digital representation of physical and functional characteristics of a facility; shared knowledge resource for information about a facility forming a reliable basis for decisions during its life cycle; also defined as existing from earliest conception to demolition" (NBS-US, 2015). A basic idea of BIM is a collaboration by all actors involved in the building process throughout the lifecycle. The information in the BIM can be extracted, updated, or modified to support and reflect the roles of an actor (Bazjanac, 2006). Therefore, BIM is information modeling and information management in a collaborative digital working environment for the AEC building process. BIM creates a product model based on collective efforts of a coordinated working process using responsive technology which makes it a collaborative e-working environment by nature.

Olofsson, et al. (2008) stated that the major key advantages of BIM are that allow the development of detailed information and analysis at a very early stage of the building process to improve decision making and reduce cross-discipline changes. The primary benefits of early stage engagement of BIM that can be identified are "(1) rapid visualization, (2) better decision support upstream in the project development process, (3) rapid and accurate updating of changes, (4) reduction of labor required to establish reliable space programs, (5) increased communication across the life cycle, and (6) increased confidence in completeness of scope" (Manning and Messner, 2008). Their study of using BIM in some projects reveal clear improvement in engineering design quality, in terms of more accurate drawings, and steadily increasing improvement in labor productivity.

It is evident that the AEC industry is highly interdisciplinary by nature that requires multidisciplinary instructions in the design process. Globally, the AEC companies are required to build more rapidly, be sustainable, improve quality, and satisfy the environmental regulations.

ARO-The Scientific Journal of Koya University
Volume VII, No.2 (2019), Article ID: ARO.10604, 10 pages
DOI: 10.14500/aro.10604
Received: 29 November 2019; Accepted: 08 December 2019
Regular research paper: Published 20 December 2019
Corresponding author's, e-mail: dilan.rostam@koyauniversity.org

 http://dx.doi.org/10.14500/aro.10604

These constraints are currently leading cultural changes in the way, the AEC industry is managing projects (Dassault Systèmes, 2014). BIM is facilitating the core of these cultural changes. However, BIM is not simply a type of software but a process that includes multidisciplinary actors that need to work collaboratively to generate and manage all-inclusive building data. Not only do BIM represents a three-dimensional intelligent model of the building but also "making significant changes in the workflow and project delivery processes" (Hardin, 2009). This brings all previous fragmented subprocesses to one inclusive platform.

Although understanding and mastering the concept of a multidisciplinary virtual working environment based on a single shared product model will by nature bring AEC industry closer than ever, unfortunately today in AEC industry BIM potential is mainly used in isolated design tasks and not for a sustained collaboration process (Thomassen, 2011). This is despite all the increasing usage of digital devices in everyday life, but still the concept of BIM has taken more than 20 years to become the preferred process of the industry in some degree today (Eastman, et al., 2008). Therefore, the focus of this work is to investigate the current views on how BIM can affect the collaborative concept of AEC industry, and in what way the adaptability of the industry toward BIM implementation can be increased.

BIM is not only about how a shared e-working space work technically but also how to act and play a role in such an environment. Therefore, the rules of conduct by actors have direct relation with their level of BIM understanding and skills.

The study aims to explore the collaboration concept of a shared digital model using BIM among AEC professionals through conducting surveys to examine the state of adopting BIM as a collaboration tool mainly in the UK and make recommendations for the best possible path to promote BIM as a single working environment and increase its usability.

II. Methodology

This research collects data from literature to find out current directions in BIM implementations and value for rational collaboration in the construction industry. After the initial studies, further data were collected through two surveys to identify the industry's state of engagement with BIM and their expected collaboration frameworks. They were asked to state their expectations, practical needs and views and the possible impact in collaborative work within the same organization or cross organizations with significant geographic distribution using BIM environment. The second survey dealt with validation of the existing undergraduate programs to understand the future graduates' basic capacity to work in a BIM oriented collaborative working environment as well as culture of BIM concept in education. Findings from the two surveys were used to identify shortcomings in the capacity building for a BIM oriented working environment. This includes BIM and team collaboration within the construction industry context, BIM management, web-based collaborative solutions, and cloud computing.

III. Industry's Collaboration Needs

BIM is one of the most promising developments in the AEC industries (Eastman, et al., 2008) where cross multidisciplinary collaboration and exchange of large building data are required. Conventionally, the means for collaboration sense between actors have been based on the repeated exchange of two-dimensional drawings and documents in form of hard or electronic copies. The long experience of the AEC industry shows that cross-disciplines engagements in preparing of model details and workflow at an early stage of a project are vital to successful design collaboration. However, during the past decade, the global adoption of computer-aided design (CAD) tools has paved the way for BIM as reliable alternative for early interaction acts in AEC projects processing (Singh, et al., 2011).

Singh, et al. (2011) showed that the expectations of BIM as a tool for collaboration are directly dependent on the construction industry's disciplines. For design disciplines, BIM is more an extension to CAD, whereas for others such as contractors and project managers, BIM is an intelligent shared document management system that can quickly take off data from CAD packages directly. However, the visualization of the shared product model is an import requirement across all disciplines, which today makes BIM an important factor in collaboration across the AEC industry.

AEC industries struggle to more productive collaboration is not only about the technological requirements for multidisciplinary interactions but also replacing the long tradition of acting task-based working environment with a new responsive culture of shared electronic product model that brings everyone together with provide adequate support for their particular discipline. Therefore, the success of BIM-based collaboration is directly depending on the adaptation and mindset ability of working in such a shared environment.

In a series of workshops and interviews that were carried out by Bhargav and Lauri (2009) with various building project actors, the following requirements were identified that provide basic insight into what collaborative act means to people involved and how it can be realized. They would like to be able to share ideas in real time, be able to collaborate on a common platform, be able to discuss an idea in a simple way, post any sort of related documents, to search within solutions and previous exchange/documents, ease of use and intuitive interface. These requirements are summarizing the human understanding of the chain of analyzing, processing and decision makings of data in relation to collaboration on a common product model.

Azhar (2011) reveals analyses of the status of BIM in the AEC survey market in the USA and mentions that the AEC industry still relies very much on traditional drawings and practices for processing their projects. At the same time, AEC professionals are realizing the power of BIM for more efficient and intelligent modeling and meaningful collaboration. Most of the companies using BIM reported in strong favor of this technology. The survey findings indicate that users want a BIM application that not only benefits from the powerful documentation and visualization capabilities

of a CAD platform but also supports inclusive design and collaboration acts. Consequently, BIM as technology is improving, and solutions in the market are continuing to evolve as they respond to the user's specific needs (Azhar, 2011).

Many studies are focusing on single disciple such as Shin (2017) and Kaner (2008) also confirmed that BIM and its impact in contributing to collaborative product design from various perspectives. They studied the impact of BIM on the structural engineering collaboration process and concluded that the work efficiency and the quality of the buildings improved when BIM collaboration was used for structural information.

Eastman, et al. (2008) introduces a comparison model based on wide studies on real AEC project to illustrate the importance of the data losses during the lifecycle of a building in a traditional paper-based process against a collaborative BIM-based delivery process (Fig. 1).

It is clear that the AEC industry as a whole has come to terms with the impact of BIM and the necessity for closer interactions in future product model processing. This product model will become the hub for interaction between all actors from concept to end of the lifespan. In other words an object-based product modeling with detailed intelligent building data. Therefore, governments around the world are setting out rules and regulations to lead the industry to full BIM adoption path to single AEC product modeling standard in targeted implementation BIM levels 0, 1, 2, and 3 (Fig. 2).

The UK BIM strategy was reinforced in 2011, which directed the construction industry to make BIM mandatory on all public projects by April 2016 to at least "level 2" BIM maturity. The concept of "BIM levels" (and "BIM level 2 compliance") has become the "accepted" definition by industry, by seeing the adoption process as the next steps in a process that has taken the AEC industry from the drawing boards to the CAD and, finally, into the shared product model in the digital age (NBS, 2014).

According to NBS, 2014, BIM levels are a government adoption process from a level to the next level for moving the construction industry to "full" collaborative working in a progressive, distinct, and recognizable way. Mills (2015) states these levels run from 0 to 3 are used as reference measures of BIM maturity.

However, the current collective historical experiences and requirements in AEC industry have brought to live the concept of level 3 BIM which represents a full collaboration between all disciplines on a shared product model in a common working space. All parties can access and modify the shared model with anticipated rights and dependencies that eliminates the risk for conflicting information, which allow collaboration between actors (Khanzode et al., 2008).

BIM level 3 extended collaboration and product lifecycle management tools can minimize waste and costs, improve sustainability, and lower the overall building process cost as well as introducing a new culture of AEC collaboration.

IV. Survey and Analysis on AEC Collaboration

The BS 1192:2007 and the complementary document PAS BS 1192-2:2013 state that the collaboration between the participants in construction projects is vital to the efficient delivery of product models. The guidelines provide instruction to the AEC industry which is increasingly working in new collaborative environments to achieve higher standards of quality and extending reuse of existing knowledge and experience (BS 1192, 2007).

Currently, in the majority of real-life AEC projects, the collaboration act taking place as the user of a tool in one discipline will import IFC models from other disciplines to their local computer application. If there is an problem related to one of the imported models, the best response by

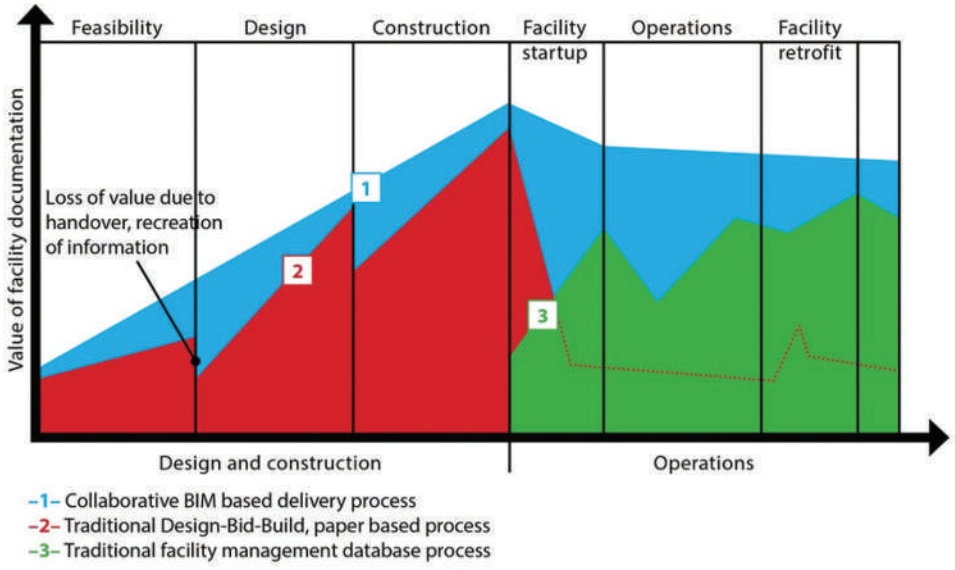

Fig. 1. Data integrity (Eastman, et al., 2008): Graphic presentation of the data losses during the lifetime of a building in a traditional paper-based process versus a collaborative building information modeling-based delivery process.

http://dx.doi.org/10.14500/aro.10604

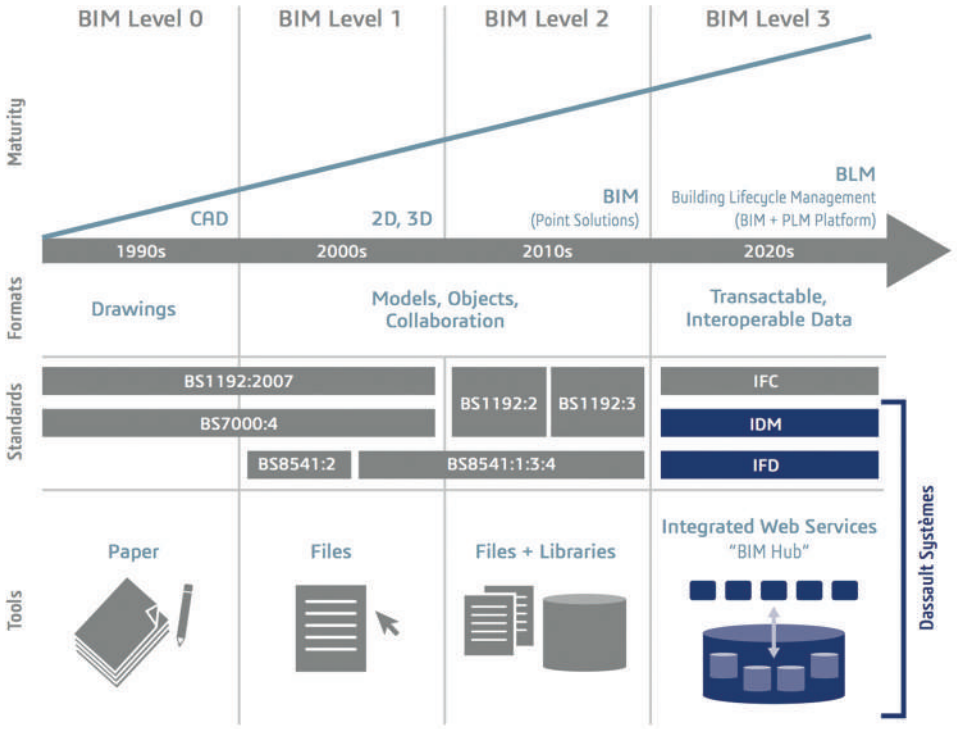

Fig. 2. An updated building information modeling maturity model from computer-aided design to building lifecycle management (Dassault Systèmes, 2014).

the user is to report that problem so they can be resolved in the original BIM authoring application from where this model originated (Stangeland, 2011).

Azhar (2011) carried out a survey to understand the current and future trends in collaboration, from a practical view. He explained that the study disclosed a number of concerns in today's collaboration conduct which circulated toward "process, technology, and people related problems" (Azhar, 2011). However, it is evident that the diversity of existing collaboration systems, compatibility problems, "training and learning curve, controlling the BIM, change and version management in models, ownership and responsibility of model data, intellectual property rights, reliability of model contents and the volatile nature of models, and uncertainty of the BIM market" obstruct the scope of BIM collaboration (Shafiq, et al., 2012).

This study carried out two parallel surveys to evaluate the current position in relation to the concept of BIM implementation and collaboration in the AEC industry and academic institutes. The study managed to collect 280 responses from academics and 89 from the industry. The survey was a parallel study between the UK and Kurdistan Region of Iraq (KRI) where only 39 academics responded and no companies responded to the survey. However, over 70% of responders to both surveys believed that collaboration is only meaningful when a common platform for real interaction exists (Fig. 3). At the same time, 85% said there should be a motivation in place for adjoining new technology that supports active collaboration as for the moment; the trends are very slow and not preferable. Many identified BIM as an emerging process empowering more meaningful collaboration in the right direction.

Over 72% of the participants agreed that collaboration through the BIM platform increased their overall productivity and quality of this project outcome. This understanding indicated to be directly related to simple, available, and sensible communication tools that eliminated the redoing and recurrent tasks. Many respondents believed that using BIM brought changes to their normal routine work and they acted differently accordingly to fit within the circumstances. However, the AEC industry still faces many challenges to adopt BIM strategies as a single alternative for project processing. The majority of the respondents indicated that lack of knowledge and clarity, leadership strategies, motivation, and lack of training are among clear reasons behind the slow adoption of BIM (Fig. 4).

This shows that there are clear indications that the virtual collaborative working environment requires a new type of skills that directing the new generation project processing more effectively. Howard and Björk (2008) also advocate the reforming of the building process rather than focusing on new technological concepts; therefore, with BIM implementation, there is a requirement to engage a new BIM skilled role within the multidisciplinary team to overview the coordination of the process model. Such perception of the future AEC project processing has led to many new adjustments in how the public sectors are engaging the AEC with their projects. The AEC industry market statistics show that the UK Government's requirements to use BIM in projects have led many organizations adopting BIM for the first time (Eadie, et al., 2015). Therefore, there is a tremendous pressure on the AEC industry to increase their marketability and working

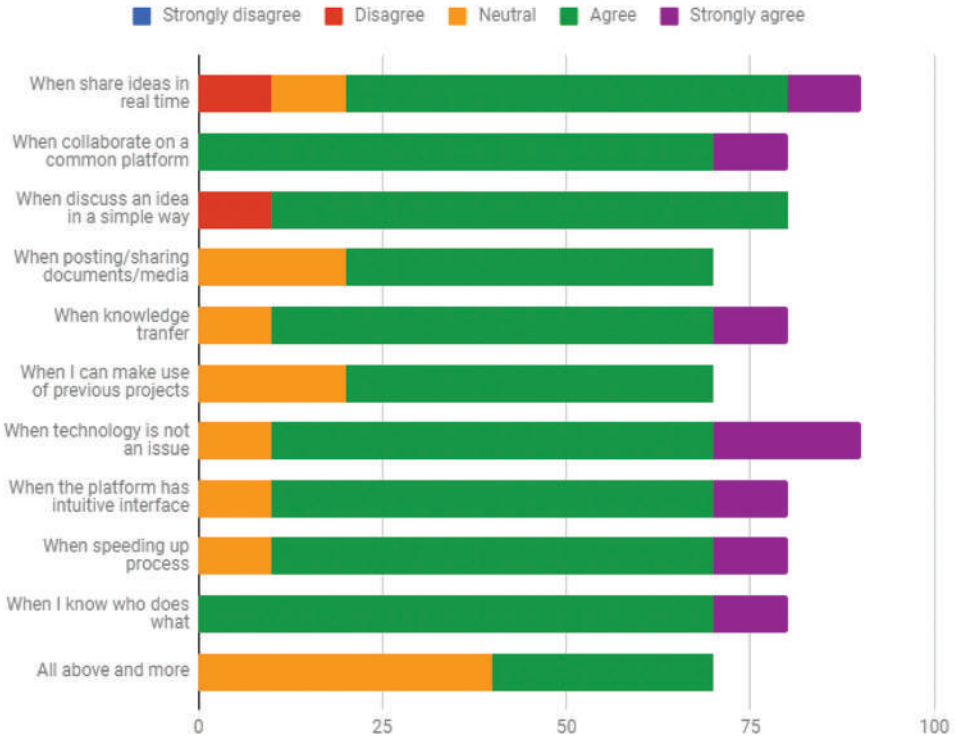

Fig. 3. Majority of respondents believed that a common platform, simplicity, and clarity in actions are empowering meaningful collaboration.

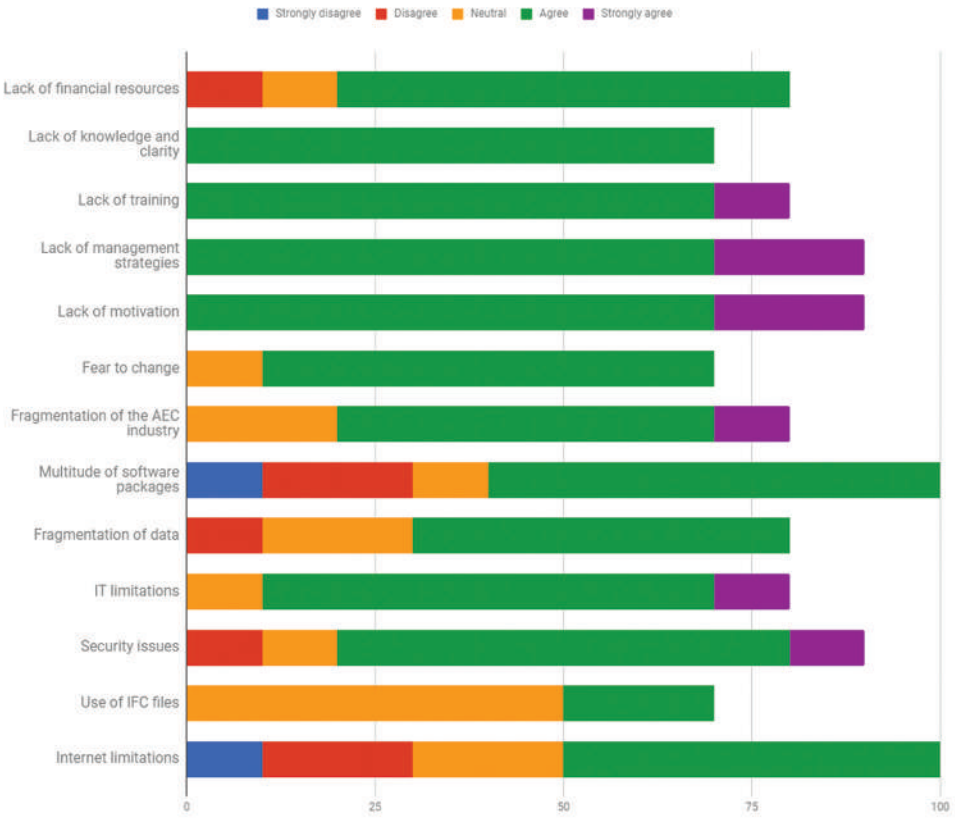

Fig. 4. Architecture, engineering, and construction industry's challenges in adopting clear building information modeling strategies.

fashion by engaging in next BIM level 3 and bring further closer all-inclusive collaboration in shared electronic working space that has positive impacts throughout the lifecycle of the product model.

V. Shared Product Model on BIM-cloud

All AEC software vendors have built software to fulfill their specific tasks and talk to a computer but that does not necessarily mean they talk to other actors involved in

the design process. As a result, the computer and human communication on the same design product is immensely isolated.

The global nature of the AEC industry and the international treaties focusing on the industrial impact on carbon emission levels govern a new concept of industrialization of the AEC industries. To keep a proactive role in this new era, all global players need to get involved and have a common roadmap and be competitive in the wider market with a new strategy.

Evidently the AEC industry tends to realize such strategy by putting a model at the center of the project and creating BIM, which will be possible to engage with deeper information into the cost and constructability. Therefore, connecting actors and technologies used in the instruction will make it possible to work smarter and make better decisions (Autodesk 2015). These trends are clear indications for Software Industry to respond accordingly.

Software vendors specializing in providing tools to the AEC industry led by users' requirements and the rapid advancement of IT are pushing for better marketability in a dynamic ever-changing market. They are looking for easy access scalable products; therefore, the cloud computing has opened a limitless possibility for innovative software. Simply explained, cloud computing is providing computing services such as storage, databases, software, and more using the Internet "the cloud." With the internet accessibility, usage and reliability on the rise it is practical to use a network of geographically distributed servers hosted on the internet to store, manage, and process data, rather than a local server or a desktop computer. This has made cloud computing to a key aspect of realizing BIM level 3 by the future for the industry that allows for real time multidisciplinary remote access collaboration within an ultimate internet browser-based BIM environment.

Singh, et al. (2011) defined a BIM shared working workspace as a collaboration platform that retains a repository of the entire building data. However, he reported many practical problems in using such platforms that have a direct impact on the collaboration process. These shortcomings identified mostly in role dependencies and responsibilities, which are critical to the setup and access to the integrated BIM model as well as interactive help functions within general (Singh, et al., 2011).

There are clear indications of cultural changes in the construction industry, in particular, the concept of collaboration and its impact on budgets and product lifecycle, which are now addressing Singh, et al. (2011) concerns. Currently, many specialized companies are already providing solutions for the entire construction lifecycle inform of collaborative platforms to facilitate the engagement around shared product models and documentations, such as Aconex (aconex.com), TeamBinder (teambinder.com), and Tekla BIMsight and RIB (rib-software.com.au). Company such as Aconex claims that they have processed 16,000 projects of $1 trillion in value from 70 countries with greater geographically distributed nature (Aconex, 2017). At the core of services provided by these companies lays the new trend in working with shared BIM and data interoperability that the IFC data set provides. Such a shared product model concept was advised and tested already in small scale by implementation and evaluation of a virtual collaborative design environment system at the University of Nottingham back in 2005 (Roshani and Tizani, 2005).

However, despite the construction industry's recent advances in technology adoption, overall management of those tools remains irregular, and the adaptation process is very slow. According to a recent survey of construction industry professionals and academic community by this study, 72% said that they have collaborated using BIM in some form in their line of work, but only 55% has received any sort of BIM training, whereas over 65% agreed that using BIM has improved company's overall productivity and project outcomes. In comparison between common software programs and cloud-based systems, the responders believed that the current available software caused data duplication problems, redundant activity, and wasted time. Further, 45% found accessing the latest set of documents and having the most current information to be a challenge. Nonetheless, more than 90% said that cloud technology is the most practical option for the industry although they showed a moderate level of confidence in BIM level 3 (Fig. 5).

There is a huge difference between the requirements for collaboration within a single discipline and collaboration across multiple disciplines within one office and multiple offices. Azhar (2011) emphasizes as we are leaving behind the requirement for BIM levels 1 and 2, the industry has overcome the obstacle of common data format and moving toward a shared product model. Nevertheless, the existing AEC collaboration model which works for documents but for model collaboration, has created a legacy mindset in the industry that needs to be replaced with "a new concept for virtual collaboration that promote new culture for collaborative working environment which will align model collaboration with a redefined industry collaboration protocols" empowered by BIM in cloud computing. The shared cloud-based product model should also provide multiple users with all-inclusive collaboration operations on model data simultaneously (Azhar, 2011). This will decrease the risk for conflicting information.

VI. BIM and Education

The construction industry has been struggling to maximize its productivity, quality and sustainability and, at the same time, minimize their wastes and loses. In a marketing research Forbes and Ahmed (2010) found that only 30% working tie in the construction industry is effective and the rest is wasted (Forbes and Ahmed, 2010). Concerning that labor productivity level in the construction industry is almost the same as 100 years ago and yet globally 75% of construction work is not finished on time, the industry is looking for a digital revolution to speed up its productivity and bringing the cost down (E-Difice, 2017).

Fig. 5. Level of confidence in various building information modeling level among the professionals and academics responders to the survey of this study.

However, various market analyses and the study shows that building performance and operation are immensely improved by adopting BIM (Azhar, 2011), but when new technologies are adopted more work practices and learning needed to adjust to the new cultural environment. Therefore, moving beyond the software concepts, a whole new institutional workspace is created which means more intense collaboration between different disciplines that require fundamental changes in their way of working and acting.

Despite a common definition, we generally notice that BIM emerges differently to different people which are the source for failed collaboration culture. This is caused due to various pathway of BIM implementation, training, and engaging of workforce strategies across the AEC industry. However, with the current increase of design complexity globally, it is urgently required to bring closer the academic collaboration of the disciplines involved in the design and construction process (Poerschke, et al., 2010) for a common BIM ground to empower future graduates engaging in the industry.

Isolation of AEC students within discipline-specific education programs, departments, and schools has impacted on graduates' ability to function within interdisciplinary design teams when they enter the industry. Not only new graduates commonly hindered by poor cross-disciplinary communication, coordination, and negotiation skills but also they emerge from educational institutions with a narrow perception of what it means to participate in the design process as a member of their specific discipline. Understanding the goals and constraints of other disciplines is key to working well in cross-disciplinary projects. They have still not become a common setting since they are challenged with coordinating different learning objectives, curricula schedules, and teaching responsibilities, as well as different research and design cultures that exist among the disciplines (Fruchther et al., 2003).

Education is an essential part of successful BIM adoption, which is becoming widespread in the AEC professions, and it is increasingly expected from graduates to know this technology. Attempts to cultivate collaboration between departments such as architecture, architectural engineering, civil engineering, and other design disciplines have been ongoing for decades (Fruchter, 2003). Academia should not only react to this expectation but also should take the lead in researching the effects of BIM concerning, for example, the changes of collaboration structures, business models, and the design process. (Fruchter and Lewis, 2003).

However, introducing the integrated environment and the use of BIM within undergraduate AEC programs will lead to an intensive collaborative educational experience for students of the involved disciplines and to the mutual understanding of technical and social aspects of a collaborative design process which is an increasing prerequisite of graduate marketability.

The EUBIM (2016) Task Group which is leading the European efforts to common BIM strategies and digital construction industry devise that "in order to create capacity in the effective and consistent use of BIM, training providers and academia need to be equipped with a common definition of the target behaviors expected by the BIM program." Without a consistent definition of the required skills, it is likely that training providers and academia will not be able to develop a sufficient capacity of capable skilled professionals for futuristic construction industry.

In single isolated attempts, it would be unproductive and cost ineffective for the BIM action group to develop industry-wide BIM training courses and training materials. Therefore, it is more desirable to develop a skills framework that layout feasible learning outcomes which industry and academia can then respond to by developing courses and materials with target requirements.

The obviously common understanding, common data exchange, common ways of working will create a foundation for consistent upskilling, training, and education that regulate the future market. This study conducted a survey among academics and students of AEC disciplines at several universities in the UK and the KRI to understand the current trends and understandings related to BIM in higher education. The survey received 280 responses in total, namely 241 from the UK and 39 responses from KRI academics.

Analysis of the respondents revealed that 86% of the respondents had a good level of understanding of BIM concept and value whereas only 43% had ever been engaged in a BIM-based project processing. However, over 90% of the respondents strongly believed in skill values gained through the BIM curriculum in graduates' marketability. Over 82% agreed that adopting new technologies in the construction industry

is directly related to the graduate's relevant skills when they start their careers, therefore, they confirmed that the future trends are good reasons to adopt the new technologies in their curriculums (Fig. 6). Yet 85% of respondents confirmed that lack of deep knowledge, clarity and right skills of BIM have hindered the higher education to integrate the BIM in their programs, especially in more technical disciplines.

The overall knowledge about BIM level 3 and the concept of cloud computing appeared to be very low among academics and students. Nearly 87% of respondents said that they are not confident about BIM level 3 and they do not know what cloud computing means to implementation BIM level 3 or advance shared product model. They also see the lack of knowledge and clarity of BIM related problems as major indicators not providing BIM education at their universities (Fig. 7).

However, it is a huge gap between different level of performing BIM strategies in higher education and the AEC industry which does not show many changes despite the increasing e-resources in our daily life. "This is counterproductive to the overall strategic role and contributions of HEIs to the ongoing BIM digital revolution in AEC industry" (Khosrowshahi, et al., 2015). Furthermore, an earlier study by BAF in 2015 revealed that 40% of questioned academic institutes considered themselves not adequately informed on BIM and the UK Government implementation strategy of BIM levels.

Embedded BIM in undergraduate programs will have a direct impact on the program structure to enable the BIM model to empower learning but adopting this strategy still at a very slow pace (BFA, 2013).

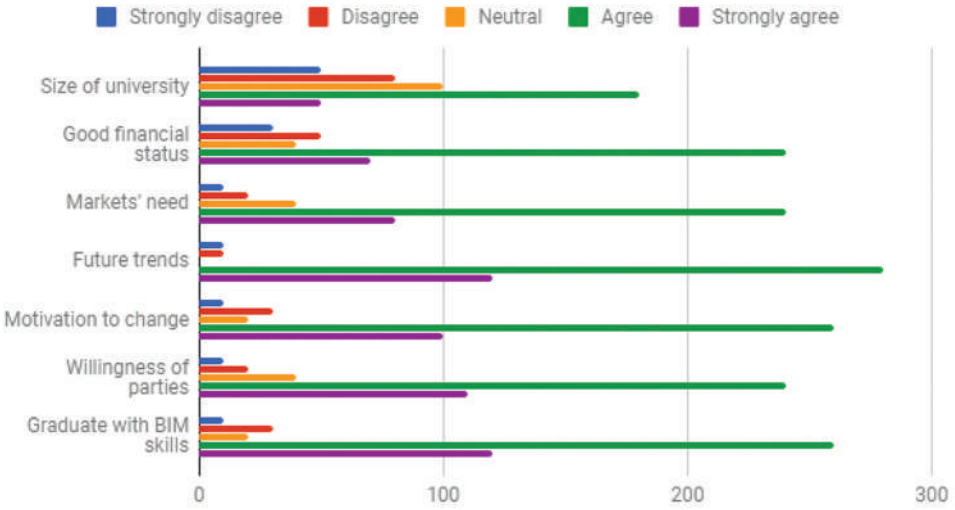

Fig. 6. Academics see the future trends a good reason to adopt new technology.

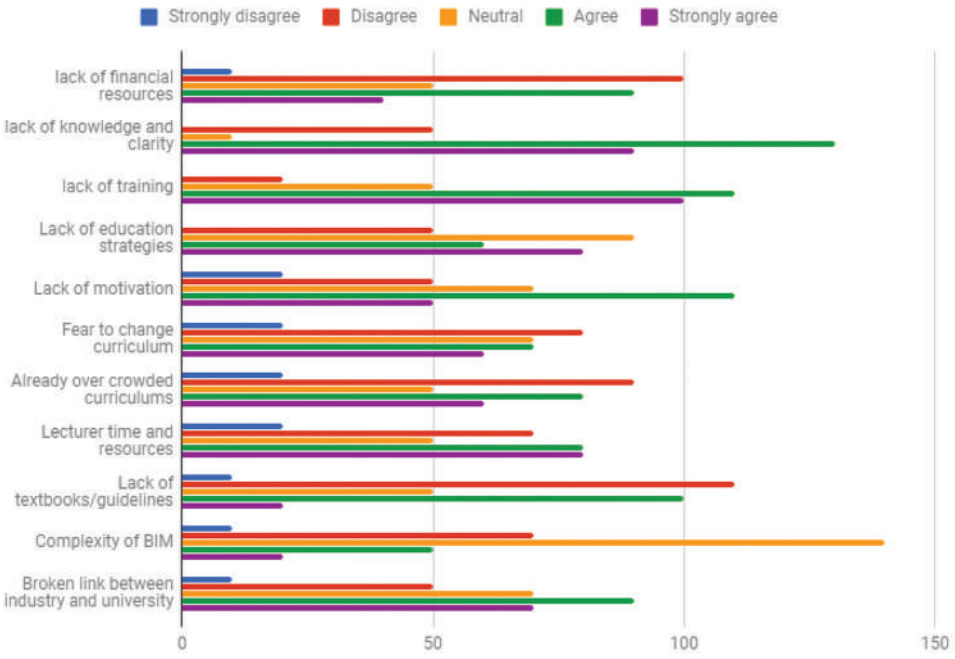

Fig. 7. Academic indicating lack of clarity and knowledge in building information modeling as major bottlenecks in providing building information modeling education.

The BAF (2013) guidelines are providing expected learning outcomes on different levels of knowledge and understanding, practical skills, and transferable skills for embedding the BIM into undergraduate and postgraduate programs, but this has not been widely used by educational yet.

VII. Recommendations

It is now widely acknowledged that the productivity and economic benefits of BIM to the AEC industry widely known and the technology to utilize BIM is rapidly advancing. Yet BIM adoption has been much slower than anticipated (Azhar, et al., 2008 and ARC 2015).

The EUBIM handbook put this in realistic figures and states "if the wider adoption of BIM across Europe delivered 10% savings to the construction sector then an additional £115 billion would be generated for the £1.2 trillion market. Even this impact could be small when compared with the potential social and environmental benefits that could be delivered to the climate change and resource efficiency agenda" (EUBIM, 2016).

BIM adoption would ultimately impose a change in the existing project processing and the whole culture of tradition AEC engagement. An integrated model development needs greater remotely collaboration and communication across disciplines that need to make sense of a virtual world. This means that a different approach to product model development is required in a virtual collaborative setting where all relevant factors contribute to a single shared model. This is a resolution for dynamic construction industry.

To make BIM more feasible for such a dynamic construction industry the shared collaborative environment need to facilitate variety organizational concepts to be selected that suit all standard data management, possible structural and project requirements and accommodate different business models to suit varied industry needs out of the package which is collected and shared from global project processing experiences.

However, these changes in the historical habits of the current industry require actors that have an educational and training background to understand that the culture of virtual working space collaboration in the sense of time and location. Such cultural education cannot be achieved through fragmented seminars but through programs of undergraduate degrees with marketing learning outcomes (Zhang et al., 2016).

In accordance with propagating the new culture of working, the industry needs to identify shortcomings and remove or redefine hurdles for the use of digital data in relation to liability, ownership, and rights that constrain benefits resulting from the wider adoption of BIM in a new ideal future working environment.

Hopkirk (2017) as well as this study reveals that currently there is BIM skills shortage among large companies in the UK. The survey indicated whereas large companies admitting the financial gain of using BIM but they cannot always find the skilled workforce they need (Hopkir, 2017). This clearly shows how the future architect and engineering should be educated with greater marketability in mind to speed up the industry adoption of BIM.

Nevertheless, the problems related to using BIM can be categorized into logistical and technical concerns. For the industry to move forward, the concept of ownership and intellectual property rights need to be changed. As the technical definition of product models has been fragmented to the smallest process and elements, then the ownership needs to be defined as one actors' specific action on these fragmented elements that are digitally signed rather than the whole product model. To facilitate such understanding and prevent disagreement over intellectual property problems, the best solution is to redefine the concept of ownership in a virtual working environment and educate actors with a new mindset for ownership rights and responsibilities that suit the future of the construction industry.

VIII. Conclusions

This study has evaluated the awareness of BIM in general and the problems surrounding the adoption process of BIM in AEC industry and the future AEC collaboration concept in particular. The study has identified the essence of the multidisciplinary collaborative working environment in an AEC virtual working space sharing a BIM-based product model and reflects a realistic capacity building for future construction industry professionals. Despite huge public and private investment in BIM related knowledge transfer, the adaptability pace has been slow. However, the success of a collaborative BIM-based project processing depends on group adoption by the actors that are expected to participate in the collaboration scenarios. Even though the NBS (2016) report revealed that 86% of respondents expect to be using BIM on at least some of their projects in 2016/2017, the working culture is far from the concept of single standard project processing. The future AEC engineers hold the key to making BIM the only method of processing a building project. Therefore, education delivery needs to evolve to accommodate all aspects of BIM processes throughout the product model lifecycle. In this approach, there is a clear need for a more rapid shift from historical habits of construction process practices to more desires futuristic BIM e-collaborative shared working processes.

The findings of this study provide useful information for AEC educational routes and industry considering adopting future level 3 BIM working strategy. The future of the construction industry is ever more defined by BIM advancement which is both exciting and challenging. It is obvious that BIM will enhance and redefine the collaboration as we know it and bring the AEC industry to much closer interdisciplinary actions and eventually lead to improved overall performance with a greater impact on the building lifecycle. This requires a closed-loop between AEC educational institutes, companies, and tools developer.

Acknowledgment

The author wishes to acknowledge his gratitude to the University of Nottingham, Department of Civil and Structural Engineering to facilitate this research work,

and also special thanks to Koya University and Ministry of Higher Education in the KRI to approve the terms and conditions of this study.

References

Aconex, 2017. *BIM Management Software for Construction Projects*. Available from: https://www.aconex.com/bim-management. [Last accessed on 2017 Aug].

ARC, 2015. *Construction Professionals Make the Case for an Industry-Specific Cloud-based Document Management Application*. ARC Document Solutions.

Autodesk, 2015. *Getting More Value from your BIM Process with Autodesk Collaboration and Data Management Products*. Available from: http://www.static-dc.autodesk.net/content/dam/autodesk/www/solutions/building-information-modeling/bim-value/bim-data-management-and-collaboration-sept-2013.pdf. [Last accessed on 2016 May 03].

Azhar, S., 2011. Building information modeling (BIM): Trends, benefits, risks, and challenges for the AEC industry. *Leadership and Management in Engineering,* 11(3), pp.241-252.

Azhar, S., Hein, M. and Sketo, B., 2008. Building Information Modeling: Benefits, Risks and Challenges." *Proc., 44th Associated Schools of Construction National Conference*, Auburn, AL.

Bazjanac, V., 2006. *Information and Communication Technologies Improving Efficiencies*. CRC, Boca Raton, FL.

Bhargav, D. and Lauri, K., 2009. Collaborative knowledge management a construction case study. *Automation in Construction,* 18(7), pp.894-902.

BIM Academic Forum UK., 2013. Embedding BIM within the Taught Curriculum. BS 1192, 2007, *Collaborative Production of Architectural, Engineering and Construction Information Code of Practice*, Annex (PAS 1192-2), BSI.

Dassault Systèmes, 2014. *Architecture, Engineering and Construction End-to-End Collaboration by BIM Enabled by BIM Level 3, An Industry Approach Based on Best Practices from Manufacturing*. Available from: http://www.emailing.3ds.com/res/dassault/a0dcaca10708f569ec7fb57ec7e577f5.pdf. [Last accessed on 2016 Feb].

Eadie, R., Browne, M., Odeyinka, H., McKeown, C. and McNiff, S., 2015. A survey of current status of and perceived changes required for BIM adoption in the UK. *Built Environment Project and Asset Management*, 5(1), pp.4-21.

Eastman, C., Teicholz, P., Sacks, R. and Liston, K., 2008. *BIM handbook: A Guide to Building Information Modeling for Owners, Managers*, *Designers, Engineers, and Contractors.* 1st ed. Publisher: Wiley, Hobokenpp, p.490.

E-difice, 2017. *The Construction Sector is in Need of a R-e-VOLUTION*. Available from: http://www.e-difice.com/en. [Last accessed on 2017 Jul].

EUBIM Task Group, 2016. *Handbook for the Introduction of Building Information Modelling by the European Public Sector, The European Union.* EUBIM Task Group, Europe.

Forbes, L.H. and Ahmed, S.M., (Eds.) 2010. *Modern Construction: Lean Project Delivery and Integrated Practices (Industrial Innovation Series)*. CRC Press, Boca Raton, FL.

Fruchter, R. and Lewis, S., 2003. Mentoring models in support of P5BL in architecture/engineering/construction teamwork. *International Journal of Engineering Education*, 19(5), pp.663-671.

Fruchter, R., 2003. Innovation in Engaging Learning and Global Teamwork Experiences. In Information Technology 2003: Towards a Vision for Information Technology in Civil Engineering: *Proceedings of the Fourth Join International Symposium on Information Technology in Civil Engineering*, Nashville, Tennessee.

Fruchther, R. and Lewis, S., 2003. Mentoring models in support of p5bl in architecture/engineering/construction global teamwork. *International Journal Engineering Education*, 19(5), pp.663-671.

Hardin, B., 2009. *BIM and construction management.* Wiley, Indianapolis, IN.

Hopkirk, E., 2017. *Skills Shortage Hits BIM Uptake, Survey Finds, News in Building Design*. Available from: https://www.bdonline.co.uk/news/skills-shortage-hits-bim-uptake-survey-finds/5090532.article. [Last accessed on 2017 Nov 14].

Howard, R. and Björk, B., 2008. Building information modelling experts' views on standardisation and industry deployment. *Journal of Advanced Engineering Informatics Archive*, 22(2), pp.271-280.

Kaner, I., Sacks, R., Kassian, W. and Quitt, T., 2008. Case studies of BIM adoption for precast concrete design by mid-sized structural engineering firms. *ITcon*, 13, pp.303-323.

Khanzode, A., Fischer, M. and Reed, D., 2008. Benefits and lessons learned of implementing building virtual design and construction (VDC) technologies for coordination of mechanical, electrical, and plumbing (MEP) systems on a large healthcare project. *ITcon*, 13, pp.324-342.

Khosrowshahi, F., Greenwood, D., Pittard, S. and Garvey, R., 2015. *Current Position and Associated Challenges of BIM Education in UK Higher Education, BIM Academic Forum.* Project Report.

Manning, R. and Messner, J., 2008. Case studies in BIM implementation for programming of healthcare facilities. *ITcon*, 13, pp.246-257.

Mills, F., 2015. *Levels of Definition Explained*. available form: https://www.theb1m.com/video/levels-of-definition-explained. [Last accessed on 2017 Sep].

NBS, 2014. *National BIM Report Survey.* Available from: https://www.thenbs.com/knowledge/nbs-national-bim-report-2014. [Last accessed on 2016 May].

NBS, 2016. *National BIM Report Survey*. Available from: https://www.thenbs.com/knowledge/national-bim-report-2016. [Last Accessed on 2016 Aug].

NBS-US, 2015. *National BIM Standard-United States® Version 3*. Available from: https://www.nationalbimstandard.org/files/NBIMS-US_V3_5.3_BIM_PxP_Guide.pdf. [Last accessed on 2017 Aug 22].

Olofsson, T., Lee, G. and Eastman, C., 2008. Case studies of BIM in use. *ITcon,* 13, pp.244-245.

Poerschke, U., Holland, R.J., Messner, J.I. and Pihlak, M., 2010. BIM Collaboration Across Six Disciplines, *Proceedings of the International Conference on Computing in Civil and Building Engineering*, pp.575-671.

Roshani, D. and Tizani, W., 2005. *Integrated IFC based Collaborative Building Design using Internet Technology*. Civil-Comp Press, Stirlingshire, UK, pp.58.

Shafiq, M.T., Matthews, J. and Lockley, S.R., 2013. A study of BIM collaboration requirements and available features in existing model collaboration systems. *Journal of Information Technology in Construction*, 18, pp.148-161.

Shin, T.S., 2017. Building information modeling (BIM) collaboration from the structural engineering perspective, Korea. *International Journal of Steel Structures*, 17(1), pp.205-214.

Singh, V., Gu, N. and Wang, X., 2011. A theoretical framework of a BIM-based multi-disciplinary collaboration platform. *Automation in Construction,* 20, pp.134-144.

Stangeland, B.K., 2011. *BIM Collaboration Format (BCF), Building Smart-International Alliance for Interoperability*. Available from: <https://www.web.archive.org/web/20120323221319>; http://www.iug.buildingsmart.com/resources/abu-dhabi-iug-meeting/IDMC_017_1.pdf. [Last accessed on 2017 Jan 24].

Thomassen, M., 2011. *BIM and Collaboration in the AEC Industry*, *A Dissertation at Aalborg University*. Denmark.

Zhang, J., Schmidt, K. and Li, H., 2016. BIM and sustainability education: Incorporating instructional needs into curriculum planning in CEM programs accredited by ACCE. *Sustainability (Switzerland)*, 8(6), p.525.

Skin Temperature Distribution over Human Head Due to Handheld Mobile Phone Call Using Thermal Imaging Camera

Yazen A. Khaleel[1], Salah I. Yahya[2,1] and Rahel Kh. Ibrahim[3]

[1]Department of Software Engineering, Faculty of Engineering, Koya University, Danielle Mitterrand Boulevard, Koya KOY45, Kurdistan Region – F.R. Iraq

[2]Department of Communication and Computer Engineering, Cihan University-Erbil, Kurdistan Region – F.R. Iraq

[3]Department of Civil Engineering, Faculty of Engineering, Koya University, Danielle Mitterrand Boulevard, Koya KOY45, Kurdistan Region – F.R. Iraq

***Abstract*—The possible biological hazards due to the mobile phone electromagnetic (EM) field exposure are caused mainly by a temperature rise in tissue. Hence, the calculation of temperature in tissue may be more realistic than the calculation of specific absorption rate (SAR) due to the more direct relationship between temperature and safety. The heat transfer to human tissue due to a phone call is caused by a combined effect of conductive heat transfer caused by the basic non-microwave-related activity of the mobile phone and the absorption of the microwave. This paper investigates the role of heat transfer in living tissue due to thermal conduction. This is achieved using a thermal imaging camera to measure and map the skin temperature distribution over human head due to mobile phone EM emission. Two commercial mobile phone brands, that is, Apple iPhone 7 Plus and Huawei P20 Pro, are used at 1800 MHz cellular connection and approximate radiated power of 0.125 W to measure the skin temperature over human head at both, cheek and tilt position for 6 and 30 min calls. The results show that in spite of the direct proportion between the deposited SAR and temperature increase in human tissues, the heat transfer due to thermal conduction may not directly proportional to the SAR, where other factors may play important roles, for example, mobile phone chassis material, heated battery, antenna location inside the mobile phone, and mobile phone position in close proximity to head.**

***Index Terms*—Apple iPhone 7 Plus, Huawei P20 Pro, Bioheat transfer equation, Mobile phone, Specific absorption rate.**

I. Introduction

Using mobile phones in proximity to human head at different positions impose an electromagnetic field (EMF) interaction between the mobile phone and the head tissues. The absorption of EM energy generated by the mobile phone in the human tissue, calculated as the specific absorption rate (SAR), has become a point of critical public discussion due to the possible health risks. SAR, therefore, becomes an important performance parameter for the marketing of cellular mobile phones and underlines the interest in optimizing the interaction between the mobile phone and the user by both consumers and mobile phone manufacturers.

In general, SAR is the appropriate metric for determining EM energy exposure in the very near field of an radiofrequency (RF) source (Allen, 1996; Association of Radio Industries and Businesses Standards, 2002; Australian Communications Authority, 2003; European Committee for Electrical Standardization, 2001; European Committee for Electrical Standardization, 2001; Federal Communications Commission, 1997; Human Models, Instrumentation, and Procedures, 2006; IEEE Standard, 2003; IEEE Standards, 2006). SAR is expressed in watts per kilogram (W/kg) of biological tissue and is generally quoted as a figure averaged over a volume corresponding to either 1 g or 10 g of body tissue. The SAR of a wireless product can be measured in two ways. It can be measured directly using body phantoms, robot arms, and associated test equipment or by mathematical modeling (Al-Mously, 2010). The handhold of a mobile phone plays an important role on the deposited SAR value in human head, and this may affect the temperature increase in head (Al-Mously and Abousetta, 2008a; Al-Mously and Abousetta, 2008b; Al-Mously and Abousetta, 2008c).

The main cause of the possible biological hazards due to the mobile phone EM emission is the temperature rise in tissue. Thus, it is preferred to calculate temperature rather than the SAR in human head tissues due to the more direct relationship between temperature and safety. Accordingly, the effect of localized SAR for mobile phones should also be related to the temperature rise in the human head.

The temperature increase in human head tissues during a mobile phone call, at cheek and tilt position, has been calculated in a number of studies (Al-Mously and Abousetta,

ARO-The Scientific Journal of Koya University
Volume VII, No.2 (2019), Article ID: ARO.10596, 6 pages
DOI: 10.14500/aro.10596
Received 19 November 2019; Accepted 21 December 2019
Regular research paper: Published 28 December 2019
Corresponding author's e-mail: yazen.adnan@koyauniversity.org

2009; Bernardi, et al., 2000; Bernardi, et al., 2001; Fujimoto, et al., 2006; Gandhi, et al., 2001; Hirata and Shiozawa, 2003; Ibrahiem, et al., 2005; Li and Gandhi, 2006; Rodrigues, et al., 2007; Rodrigues, et al., 2008; Samaras, et al., 2007; Van Leeuwen, et al., 1999; Wainwright, 2000; Wang and Fujiwara, 1999; Zygiridis and Tsiboukis, 2008), and a brief description of their exposure conditions and types of RF source model has been presented in Al-Mously, 2010.

In the previous reported works, the temperature increase in human head tissues has been calculated numerically using both homogeneous and heterogeneous human head phantom during mobile phone calls of 30 min and 6 min, according to IEEE/ANSI/FCC (Federal Communications Commission, 1997; IEEE Standard, 2003; IEEE Standards, 2006) and International Commission on Non-Ionizing Radiation Protection (ICNIRP) (European Committee for Electrical Standardization, 2001; European Committee for Electrical Standardization, 2001), respectively. The temperature increase in human head tissues has been calculated implementing the bioheat equation (BHE) (Pennes, 1948) based on the calculated SAR. The SAR according to IEEE/ANSI/FCC standards is calculated for an averaging mass of 1 g, whereas it is for 10 g according to the standard ICNIRP. The international standards, that is, IEEE/ANSI/FCC and ICNIRP, have been set for SAR limits according to tissue type, that is, head, limb, and whole body. No temperature limits have been set by any standard. This is because the temperature increase in tissue depends on many factors that are difficult to be measured using phantom with test equipment. Rusnani and Norsuzila (2008) used an infrared thermal camera to measure the temperature surface distribution due to three mobile phone brands in close proximity to the user's head after 6 and 30 min calls. The maximum recorded temperature after 30 min calls were 2.9°C, 1.1°C, and 2.0°C due to Nokia 3160 (Max. SAR = 1.14 W/kg), Samsung SGH300 (Max. SAR = 0.74 W/kg), and Sony Ericson T230 (Max. SAR = 0.60 W/kg), respectively. Rusnani and Norsuzila (2008) claimed that the temperature increase in the head is not due to the phone battery heating as long as the maximum temperature of the mobile phone is stayed below the temperature of head. Rusnani and Norsuzila (2008) did not consider the temperature increase in the head skin due to the EM near filed, but the phone battery heating. Moreover, he did not consider the effect of the mobile phone positions, cheek and tile with respect to head, according to the IEEE-Std. 1528-2003. Al-Mously (2010) measured the temperature increase in two mobile phone chases, candy bar type Motorola L71 and clamshell type Motorola RAZR V3i, after 60 min call, and then, the two mobile phones were simulated, using 3D EM simulation software, in close proximity to head at cheek position to measure the temperature increase in pinna tissue due to thermal conduction. Bauer, et al. (2018) investigated the influence of smartphones' operation modes on the superficial temperature distribution in the human pinna region. He observed that there are statistically significant differences between mean temperatures of the pinna before and immediately after the use of the smartphone, independent of whether RF communication was on (normal mode) or off (flight mode). The increase in tissue temperature was caused by a combined effect of conductive heat transfer caused by the basic non-microwave-related activity of the smartphone and the absorption of the microwave.

This paper shows that the temperature increase in head tissue due to the thermal conduction for long phone call duration may play an important role. The temperature increase due to the thermal conduction does not necessary depend on the mobile phone SAR, but on other factors, for example, handheld position (ventilation gap between mobile phone and human head), antenna location inside the mobile phone, battery temperature increase, etc.

II. Pennes BHE

Temperature ($T = T(x, y, z, t)$ [°C]) can be modeled in the head with a numerical implementation, for example, finite difference, of the bioheat transfer equation (BHE), developed by Pennes (1948):

$$\rho c \frac{\partial T}{\partial t} = \nabla\left(k \nabla T\right) + \rho Q_{met} + \rho\left(\mathrm{SAR}\right) - B\left(T - T_{blood}\right) \quad (1)$$

$$B = \rho_{blood}\, c_{blood}\, \rho\omega \quad (2)$$

where the different values of ρ (kg/m^3) (material density), c (J/[kg °C]) (specific heat capacity), k (W/[m °C]) (thermal conductivity), Q_{met} (W/kg) (metabolic heat generation rate), B (W/[m^3 °C]) (blood perfusion coefficient), and ω (L/[s kg]) (blood perfusion rate) for several different tissues were acquired from literature (Bernardi, et al., 2000; Bernardi, et al., 2001; Fujimoto, et al., 2006; Hirata and Shiozawa, 2003; Li and Gandhi, 2006) and are given in Rusnani and Norsuzila (2008) (Al-Mously and Abousetta, 2009). It should be noticed that the results based on experiments involving animals were used for most of the thermal parameters required in the human head model. The uncertainties in the maximum

TABLE I
SAR in Head Tissues of Apple iPhone 7 Plus and Huawei P20 Pro for Non-occupational/Unaware Users in American and European Regions

American IEEE/ANSI/FCC					
Phone brand	SAR (W/kg) in head	Measurement method	Limit (W/kg)	Averaging mass	Time
Apple iPhone 7 Plus	1.190	C95.1	1.6	1 g	30 min
Huawei P20 Pro	1.030				
European ICNIRP					
Phone brand	SAR (W/Kg) in head	Organization/body	Limit (W/kg)	Averaging mass	Time
Apple iPhone 7 Plus	1.340	EN50360	2.0	10 g	6 min
Huawei P20 Pro	0.730				

SAR: Specific absorption rate

temperature increases caused by those in thermal parameters were investigated in Hirata, et al., 2003; Samaras, et al., 2007.

Heat transfer in living tissue is a complex process and includes conduction, convection, and blood perfusion (such as delivery of the arterial blood to a capillary bed), cooling of human body by radiation, and metabolic heat generation (Ghassemi and Shahidian, 2017).

In Equation (1), the term on the left represents the rate of change in the stored internal energy of the tissue, the term $\nabla\ (k\nabla T) = k\nabla^2 T$ is the heat transfer due to thermal conduction, which is under investigation of this work, and the last term relates to convection heat loss associated with blood flow.

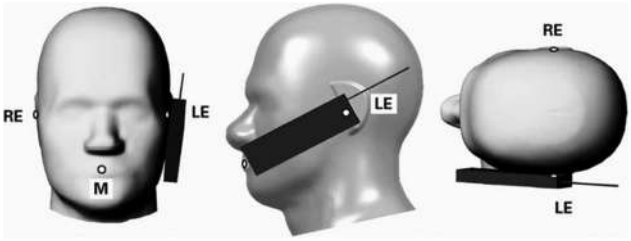

Fig. 1. Specific anthropomorphic mannequin with mobile phone in cheek position on the left side according to the IEEE-Std. 1528-2003. RE: Right pinna, LE: Left Pinna, and M: Mouth.

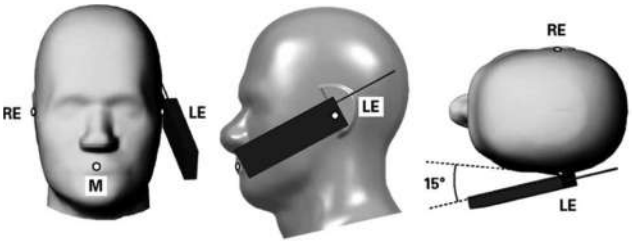

Fig. 2. Specific anthropomorphic mannequin with mobile phone in tilt position on the left side according to the IEEE-Std. 1528-2003. RE: Right pinna, LE: Left pinna, and M: Mouth.

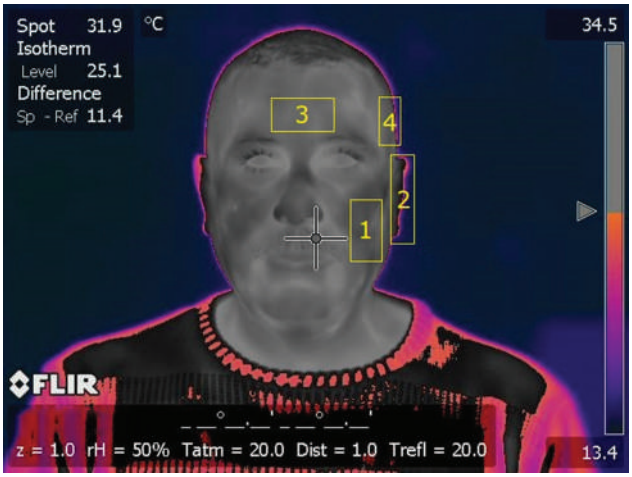

Fig. 3. Front view of the human head with indicated four regions that their surface temperatures are measured due to mobile phone calls using FLIR SC660 thermal imaging camera. Region 1: Cheek, region 2: Pinna, region 3: Forehead, and region 4: Side head.

III. Skin Temperature Measurement Procedure and Results

According to Equation (1), it is very clear that the thermal conduction plays an important role in heat transfer in living tissue. Thus, mapping the surface temperature distribution on human head skin may give a deeper perception about the term $\nabla\ (k\nabla T) = k\nabla^2 T$.

Two commercial mobile phone brands are selected to be investigated in terms of the temperature increase in human head skin that both may cause, that is, Huawei P20 Pro and iPhone 7 Plus. Their SAR values based on the manufacturer datasheet are listed in Table I.

According to Table I, Apple iPhone 7 Plus shows more deposited SAR in human head tissue than Huawei P20 Pro, based on both organization standards; American IEEE/ANSI/FCC and European ICNIRP. Consequently, and based on the reported previous works, the temperature increase in human head due to a phone call EMF emission caused by iPhone 7 Plus is more than the one caused by Huawei P20 Pro. This is true since the temperature increase in human tissue is directly proportional to the deposited SAR.

The procedure of skin temperature measurement over human head is by making phone calls for 6 min and 30 min using the mobile phones Apple iPhone 7 Plus and Huawei P20 Pro, at both cheek and tilt positions. Hence, eight phone

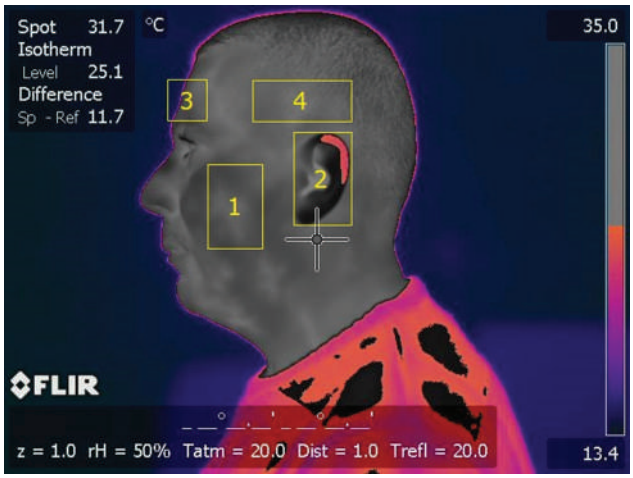

Fig. 4. Side view of the human head with indicated four regions that their surface temperatures are measured due to mobile phone calls using FLIR SC660 thermal imaging camera. Region 1: Cheek, region 2: Pinna, region 3: Forehead, and region 4: Side head.

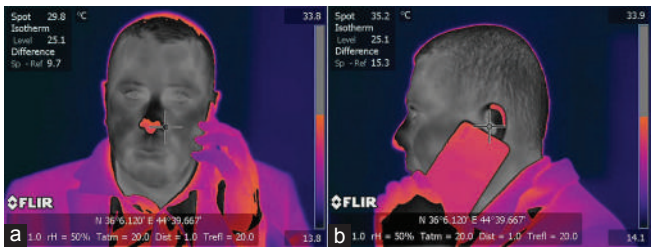

Fig. 5. (a and b) Apple iPhone 7 plus handheld in close proximity to human headshot by the FLIR SC660 thermal imaging camera.

http://dx.doi.org/10.14500/aro.10596

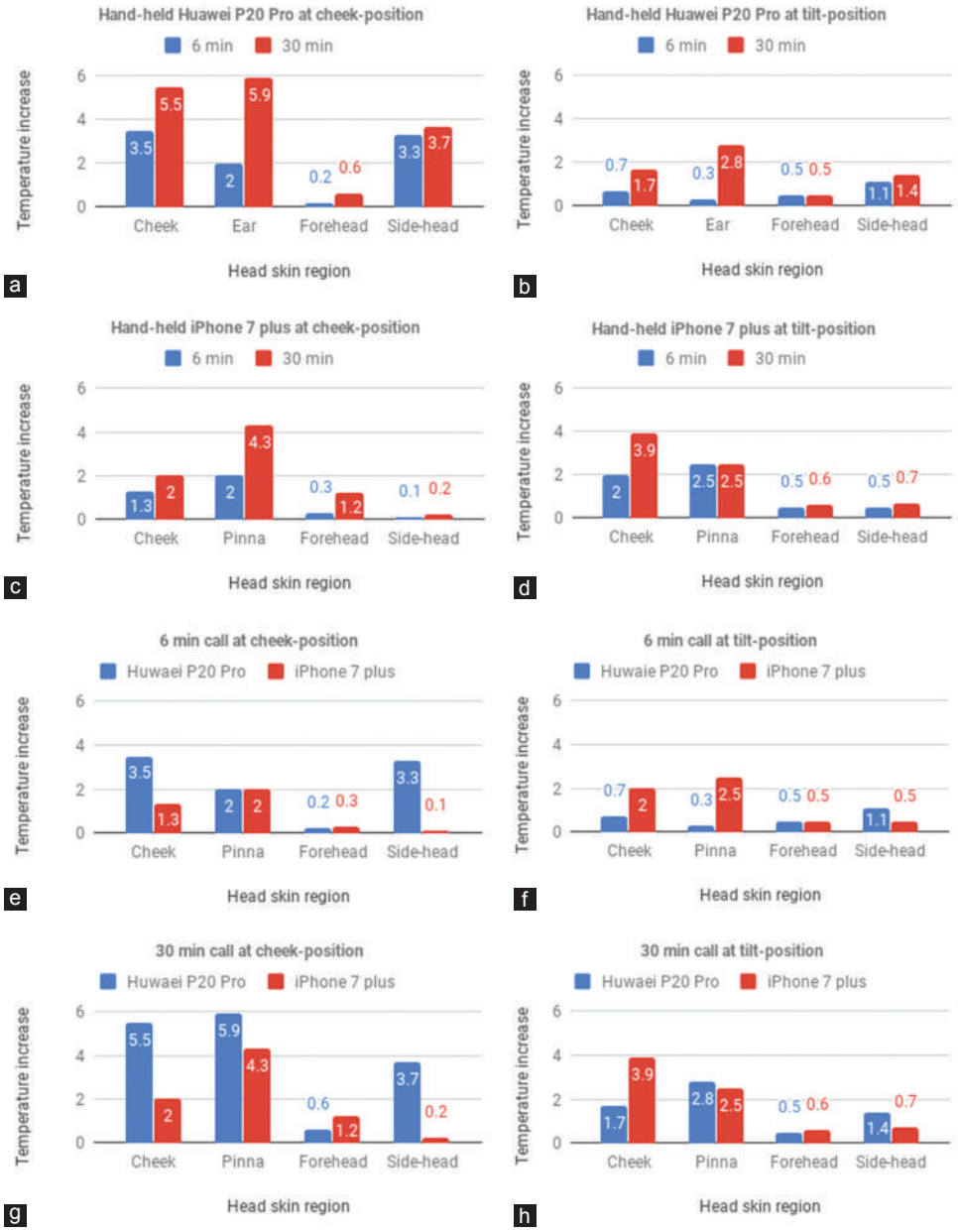

Fig. 6. Measured temperature (°C) distribution in head skin regions, that is, cheek, pinna, forehead, and side head, for different mobile phone brands after 6 and 30 min calls. (a) Handheld Huawei P20 Pro at cheek position, (b) handheld Huawei P20 Pro at tilt position, (c) handheld iPhone 7 Plus at cheek position, (d) handheld iPhone 7 Plus at tilt position, (e) 6 min call at cheek position, (f) 6 min call at tilt position, (g) 30 min call at cheek position, (h) 30 min call at tilt position.

call scenarios of standardized tone are conducted, using the same room temperature and by the same person at the same body and mobile phone temperatures. The temperature is measured by a thermal imaging camera in each scenario after removing the mobile phone, immediately. The cheek and tilt position of the mobile phone in close proximity to head is defined by IEEE-Std. 1528-2003, is defined in Figs. 1 and 2.

A thermal imaging camera type FLIR SC660 is used for the measurement, and four regions over human head are selected to measure the temperature after phone calls of 6 and 30 min. Figs. 3 and 4 show a thermal camera image of the human head, indicating the four regions under measurements, that is, cheek, pinna, forehead, and side head.

Fig. 5 shows the front and side view of human making a phone call using Apple iPhone 7 Plus at tilt position shot by the FLIR SC660 thermal imaging camera.

Fig. 6 shows the temperature values of the skin of the cheek, pinna, forehead, and side head regions, all are measured for the mobile phones Apple iPhone 7 Plus and Huawei P20 Pro at cheek and tilt positions and after durations 6 and 30 min calls.

IV. Discussion and Conclusion

According to the skin temperature distribution is shown in Fig. 6, the following are concluded:

1. The temperature increase in the head skin regions is directly proportional to the phone call duration, for the same mobile phone and the same mobile position with respect to head
2. Huawei P20 Pro causes more skin temperature increase over human head at cheek position than at tilt position. The same scenario exists for the Apple iPhone 7 Plus, but in the pinna and forehead regions, only. This may due to different antenna location inside both mobile brands
3. At cheek position, and though it has less SAR, Huawei P20 Pro shows more temperature increase in the skin of the cheek, pinna, and side head, as compared with Apple iPhone 7 Plus, after 6 and 30 min phone calls. This may due to different antenna locations inside both mobile brands and different battery heat
4. At tilt position, Huawei P20 Pro shows more temperature increase than Apple iPhone 7 Plus in the skin of the pinna after 6 min and on the skin of side head after 6 and 30 min phone calls
5. The results at tilt position do not follow the trend of the results at cheek position. This is due to the ventilation space between the mobile phone and the cheek.

Based on the above conclusions and the results in Fig. 6, it is obvious that the skin temperature distribution over the human head, and consequently the thermal conduction, does not follow the SAR values trend. The temperature increase in the head skin regions is due to both, heated battery and the EM near field of the mobile phone. Although Huawei P20 Pro deposited less SAR in head tissues, as compared with Apple iPhone 7 Plus, Table I, it causes more temperature increase in the head skin at cheek position, at least, for the call durations 6 and 30 min. In summary, the heat transfer due to the thermal conduction depends on other factors rather than on SAR value, only, for example, mobile phone chassis material, mobile phone heated battery, antenna location inside the mobile phone, and mobile phone position in close proximity to head.

References

Allen, S.G., 1996. Radiofrequency field measurements and hazard assessment. *Journal of Radiological Protection*, 11, pp.49-62.

Al-Mously, S. I., 2010. *Design and Performance Enhancement of Cellular Handset Antennas and Assessment of Their EM Interaction with a Human*. Ph.D. The Academy of Graduate Studies.

Al-Mously, S.I. and Abousetta, M.M., 2008a. A novel cellular handset design for an enhanced antenna performance and a reduced SAR in the human head. *International Journal of Antennas and Propagation,* 2008, p.10.

Al-Mously, S.I. and Abousetta, M.M., 2008b. A study of the hand-hold impact on the EM interaction of a cellular handset and a human head. *International Journal of Electronics, Circuits, and Systems,* 2(2), pp.91-95.

Al-Mously, S.I. and Abousetta, M.M., 2008c. Anticipated impact of hand-hold position on the electromagnetic interaction of different antenna types/positions and a human in cellular communications. *International Journal of Antennas and Propagation*, 2008, p.22.

Al-Mously, S.I. and Abousetta, M.M., 2009. A Definition of Thermophysiological Parameters of SAM Materials for Temperature Rise Calculation in the Head of Cellular Handset User. In: *Proceeding of the Progress in Electromagnetics Research Symposium*. Moscow, Russia, pp.170-17. Available from: http://www.piers.org. [Last accessed on 2019 Oct 22].

Association of Radio Industries and Businesses Standards, 2002. *Specific Absorption Rate (SAR) Estimation for Cellular Phone*. ARIB, Japan.

Australian Communications Authority, 2003. *Radio Communications (Electromagnetic Radiation-human Exposure)*. ACA Standard, Canberra.

Bauer, J., Górecki, I., Kohyt, M., Migasiewicz, A. and Podbielska, H., 2018. The influence of smartphones' operation modes on the superficial temperature distribution in the human auricle region. *Journal of Thermal Analysis and Calorimetry*, 133(1), pp.559-569.

Bernardi, P., Cavagnaro, M., Pisa, S. and Piuzzi, E., 2000. Specific absorption rate and temperature increases in the head of a cellular-phone user. *IEEE Transaction on Microwave Theory and Techniques*, 48(7), pp.1118-1126.

Bernardi, P., Cavagnaro, M., Pisa, S. and Piuzzi, E., 2001. Power absorption and temperature elevations induced in the human head by a dual-band monopole-helix antenna phone. *IEEE Transaction on Microwave Theory and Techniques*, 49(12), pp.1118-1126.

European Committee for Electrical Standardization, 2001. *Basic Standard for the Measurement of Specific Absorption Rate Related to Exposure to Electromagnetic Fields from Mobile Phones (300 MHz-3GHz)*. CENELEC, Brussels.

European Committee for Electrical Standardization, 2001. *Product Standard to Demonstrate the Compliance of Mobile Phones with the Basic Restrictions Related to Human Exposure to Electromagnetic Fields (300 MHz-3GHz)*. CENELEC, Brussels.

Federal Communications Commission, 1997. *Evaluating Compliance with FCC Guidelines for Human Exposure to Radio Frequency Electromagnetic Field, Supplement C to OET Bulletin 65*. FCC, Washington, DC, USA.

Fujimoto, M., Hirata, A., Wang, J., Fujiwara, O. and Shiozawa, T., 2006. FDTD-derived correlation of maximum temperature increase and peak SAR in child and adult head models due to dipole antenna. *IEEE Transactions on Electromagnetic Compatibility*, 48(1), pp.240–247.

Gandhi, O.P., Li, Q.X. and Kang, G., 2001. Temperature rise for the human head for cellular telephones and for peak SARs prescribed in safety guidelines. *IEEE Transaction on Microwave Theory and Techniques*, 49(9), pp.1607–1613.

Ghassemi, M. and Shahidian, A., 2017. *Nano and Bio Heat Transfer and Fluid Flow*. Elsevier Inc., Amsterdam.

Hirata, A. and Shiozawa, T., 2003. Correlation of maximum temperature increase and peak SAR in the human head due to handset antennas. *IEEE Transaction on Microwave Theory and Techniques*, 51(7), pp.1834–1841.

Hirata, A., Morita, M. and Shiozawa, T., 2003. Temperature increase in the human head due to a dipole antenna at microwave frequencies. *IEEE Transactions on Electromagnetic Compatibility*, 45, pp.109–117.

Human Models, Instrumentation, and Procedures, 2006. *Part 1: Human Exposure to Radio Frequency Fields from Hand-held and Body-mounted Wireless Communication Devices Procedure to Determine the Specific Absorption Rate (SAR) for Hand-held Devices Used in Close Proximity to the Ear (Frequency Range of 300 MHz to 3 GHz)*. IEC, Geneva.

Ibrahiem, A., Dale, C., Tabbara, W. and Wiart, J., 2005. Analysis of the temperature increase linked to the power induced by RF source. *Progress in Electromagnetics Research*, 52, pp.23-46.

IEEE Standard, 2003. *IEEE Recommended Practice for Determining the Peak Spatial-average Specific Absorption Rate (SAR) in the Human Head from Wireless Communications Devices: Measurement Techniques*. IEEE Standard, New Jersey.

IEEE Standards, 2006. *Standard for Safety Levels with Respect to Human Exposure to Radiofrequency Electromagnetic Fields, 3 kHz to 300 GHz*. Coordinating Committee, Atlanta.

Li, Q.X. and Gandhi, O.P., 2006. Thermal implications of the new relaxed

IEEE RF safety standard for head exposures to cellular telephones at 835 and 1900 MHz. *IEEE Transaction on Microwave Theory and Techniques*, 54(7), pp.3146-3154.

Pennes, H.H., 1948. Analysis of tissue and arterial blood temperature in resting forearm. *Journal of Applied Physiology*, 1, pp.93-122.

Rodrigues, A.O., Malta, L., Viana, J.J., Rodrigues, L.O.C. and Ramírez, J.A., 2008. A head model for the calculation of SAR and temperature rise induced by cellular phones. *IEEE Transaction on Magnetics*, 44(6), pp.1446-1449.

Rodrigues, A.O., Viana, J.J., Rodrigues, L.O. and Ramirez, J.A., 2007. Calculation of temperature rise induced by cellular phones in the human head. *Journal of Microwaves and Optoelectronics*, 6(1), pp.310-322.

Rusnani, A. and Norsuzila N., 2008. Measurement and analysis of handheld mobile telephones using infrared thermal camera. In: *International Confereence RF and Microwave Conference Proceeding*. IEEE, Kuala Lumpur, Malaysia, pp.268-273.

Samaras, T., Kalampaliki, E. and Sahalos, J., 2007. Influence of thermophysiological parameters on the calculations of temperature rise in the head of mobile phone users. *IEEE Transactions on Electromagnetic Compatibility*, 49(4), pp.936-939.

Van Leeuwen, G.M.J., Lagendijk, J.J.W., Van Leersum, B.J.A., Zwamborn, A.P.M., Hornsleth, S.N. and Kotte, A.N.T., 1999. Calculation of change in brain temperatures due to exposure to a mobile phone. *Physics in Medicine and Biology*, 44, pp.2367-2379.

Wainwright, P., 2000. Thermal effects of radiation from cellular telephones. *Physics in Medicine and Biology*, 45, pp.2363-2372.

Wang, J. and Fujiwara, O., 1999. FDTD computation of temperature rise in the human head for portable telephones. *IEEE Transaction on Microwave Theory and Techniques*, 47(8), pp.1528-1534.

Zygiridis, T.T. and Tsiboukis, T.D., 2008. Assessment of the human head exposure to wireless communication devices: Combined electromagnetic and thermal studies for diverse frequency bands. *Progress in Electromagnetics Research B*, 9, pp.83-96.

Theoretical Study of the [4+2] Cycloaddition Reaction of Trifluoroethylene with Five-membered Chalcogens Heterocyclic Compounds

Haydar A. Mohammad-Salim[1] and Hassan H. Abdallah[2]

[1]Department of Chemistry, Faculty of Science, University of Zakho, Duhok 42001, Iraq

[2]Department of Chemistry, College of Education, Salahaddin University, Erbil 44001, Iraq

***Abstract*—[4+2] cycloaddition reaction has enormous significant in organic chemistry synthesis reactions and yet remains unexplored for the synthesis of fluorine-containing compounds. A density functional theory study of the stereo- and regioselectivity of the [4+2] cycloaddition reaction of trifluoroethylene with furan, thiophene, and selenophene was carried out in the gas phase. The B3LYP functional is used throughout in combination with 6-31G(d) basis set. The analysis of stationary points and the energetic parameters indicates that the reaction mechanism is concerted and confirms that the *exo*-adducts are thermodynamically and kinetically more favored than *endo*-adducts. The calculated branching ratio indicates that the *exo*-adducts have the higher percent yield than *endo*-adducts and the yield of *endo*-adducts is increased only slightly on proceeding from furan, through thiophene, and onto selenophene. The analysis of the frontier molecular highest occupied molecular orbital (MO) and lowest unoccupied MO orbitals indicates that the *exo*-adducts are more stable due to their higher energy gab. The reaction energies were compared to the MP2/6-31G(d) and CCSD(T)/6-31G(d) calculations.**

***Index Terms*—Density functional theory, B3LYP, Regioselectivity, Stereoselectivity, [4+2] Cycloaddition.**

I. Introduction

The [4+2] cycloaddition reaction (Diels-Alder reaction) is one of the most powerful reactions for building six-membered carbocyclic ring in organic synthesis (Nicolaou, et al., 2002). The Diels–Alder reaction of conjugated diene with dienophile (alkene or alkyne) is concerted reaction (Houk, et al., 1986; Woodward and Katz, 1959). This reaction proceeds more favorable if electron-rich dienes reacts with electron-poor dienophile. Thus, typical dienes are substituted with electron-donating groups whereas good dienophiles are substituted with electron-withdrawing groups (Gregoritza and Brandl, 2015).

The Diels–Alder reaction may give two stereoisomeric products, *exo*- and *endo*-adducts, relying on the conformation of the transition state when a cyclic diene and dienophile react with each other (Lautens and Edwards, 1989; Nickon, et al., 1978). For that reason, a huge amount of theoretical studies have been devoted trying to explore the reaction mechanism leading to *exo*- and *endo*-selectivity. Density functional theory (DFT) has been used widely and found as a very convenient method for getting reliable results and it has low computational cost (Cossío, et al., 1999; Liu, et al., 1998; Silva and Goodman, 2002). This method has been successfully used in many [4+2] cycloaddition reactions (Domingo, et al., 2002; Domingo, et al., 2014; Fernández and Bickelhaupt, 2014; Ho, et al., 2016; Levandowski, et al., 2018; Rivero, et al., 2017b). Among these studies, computational works were compared with experimental to obtain detailed reaction mechanism, stero- and regioselectivity. Stereoselectivity of the reaction of cyclopentadiene with protonated phenylethylimine was studied at B3LYP/6-31G(d) level of theory (Teixeira, et al., 2009). The results indicate that the *exo*-adduct is found to be more stable than *endo*-adduct. In addition, DFT method at M06-2X/6-31G(d) level of theory was used for the reaction of s-cis-2,3-dibromo-1,3-butadiene and malic anhydride (Rivero, et al., 2017a). This reaction clearly favors the *exo*-adduct over the *endo*-adduct due to the lower activation energy for the *exo* path.

Fluorine-containing organic compounds have found a significant position in organic chemistry and the synthesis of compounds exhibiting exciting properties for medicinal and agricultural purposes. The reaction of 2-fluorooct-1-en-3one with cyclopentadiene was studied experimentally and found to yield the *exo*-adduct preferably under thermal and microwave-assisted conditions (Essers, et al., 2002). The percent yield for *exo*- and *endo*-adducts was found to be 69 and 31%, respectively, under thermal condition, whereas the percent yield became 70 and 30% under microwave-

ARO-The Scientific Journal of Koya University
Volume VII, No.2 (2019), Article ID: ARO.10575, 9 pages
DOI: 10.14500/aro.10575
Received 22 October 2019; Accepted 16 December 2019
Regular research paper: Published 28 December 2019
Corresponding author's e-mail: hayder.salim@uoz.edu.krd

http://dx.doi.org/10.14500/aro.10575

assisted condition. The reactions of cyclopentadiene with benzyl 2-fluoroacrylate, 2-fluoroacrylic acid amide, 1,1-difluoroethene, and 1,2-diflurodinitro ethene were studied experimentally and the *exo*-adducts were found to be more favorable with higher percent yield than *endo*-adducts (Baum, et al., 1991; Ito, et al., 1999; Ito, et al., 1998; Leroy, et al., 1987).

The Diels–Alder reaction of trifluoroethylene (TFE) with furan and its derivatives has been investigated experimentally (Chambers, et al., 2000). However, based on our knowledge, the detail information about the reaction mechanism, stereo- and regioselectivity have not yet been obtained. Therefore, the aim of this paper is to suggest the mechanism of the cycloaddition of TFE with furan and other heterocyclic compounds containing chalcogens using DFT method. Herein, furan, 2, thiophene, 3, and selenophene, 4 are used in [4+2] cycloaddition reaction with TFE, 1 to investigate the effect of chalcogens on reaction mechanism and regioselectivity. Scheme 1 shows the *exo*- and *endo*-adducts of these [4+2] cycloaddition reactions.

II. Computational Methods

All calculations have been done with the Gaussian 9 package under Linux operation system (Frisch, et al., 2009). DFT method has been proven to be a convenient method for the study of [4+2] cycloaddition reactions and is achieved in this study (Khabashesku, et al., 2001; Lemal, 2017; Parr

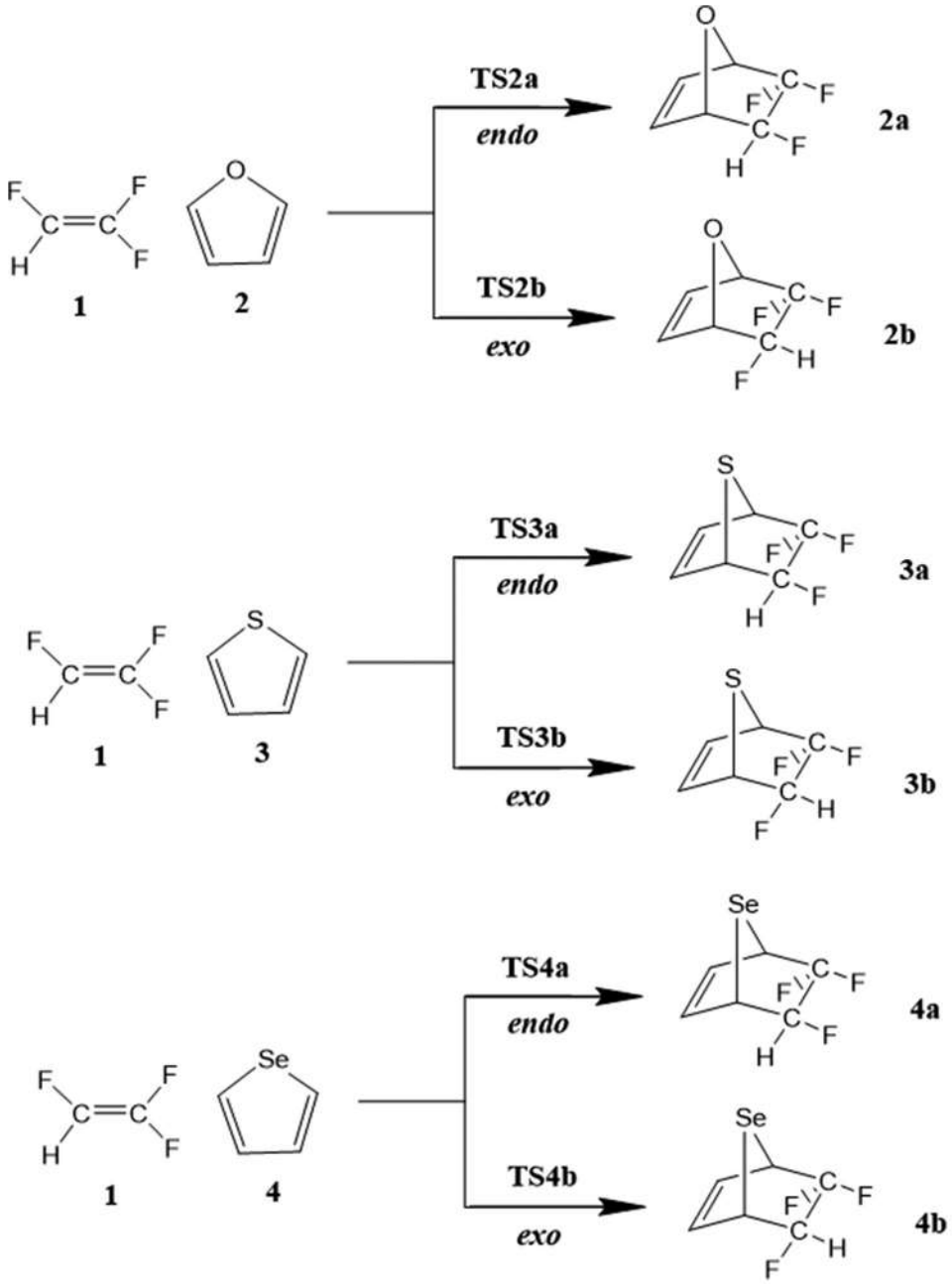

Scheme 1: Reaction paths for the [4+2] cycloaddition reaction of TFE, 1 with furan, 2, thiophene, 3, and selenophene, 4.

and Weitao, 1989). B3LYP functional is used throughout in combination with 6-31G(d) basis set (Ditchfield, et al., 1971; Lee, et al., 1988). MP2 and CCSD(T) methods were used to predict the reaction energies using the same basis set. Frequency calculations were performed to ensure that a transition state has only one imaginary frequency and a local minimum has no imaginary frequencies. Intrinsic reaction coordinate computations were carried out to verify that the transition states connect with the required reactants and products (Fukui, 1970). All energies and thermodynamic parameters reported in this paper were obtained from the frequency calculations at the same level of theory. The enthalpies, Gibbs free energies, and entropies in gas phase were obtained with the standard statistical thermodynamics at 298.15 K and 1 atm. The CYLview software was used as a graphical interface (Legault, 2009).

The global electrophilicity index (ω) is obtained in terms of the electronic chemical potential (μ) and the chemical hardness (η) using the following simple expression (Parr, et al., 1999):

$$\omega = \frac{\mu^2}{2\eta} \quad (1)$$

The chemical hardness (η) and the electronic chemical potential (μ) quantities may be approached in terms of the one-electron energies of highest occupied molecular orbital (HOMO) and lowest unoccupied MO (LUMO), ε_H and, ε_L as (Parr and Pearson, 1983; Parr and Weitao, 1994):

$$\eta \approx \varepsilon_L - \varepsilon_H \quad (2)$$

$$\mu \approx \frac{\varepsilon_H + \varepsilon_L}{2} \quad (3)$$

The relative nucleophilicity index (N) obtained based on the energies of HOMO within the scheme of Kohn-Sham (Kohn and Sham, 1965). This quantity can be defined using equation (4). Where TCE is tetracyanoethylene and is chosen due to its lowest HOMO energy as a reference (Domingo, et al., 2008).

$$N = E_{HOMO(Nu)} - E_{HOMO(TCE)} \quad (4)$$

III. Results and Discussion

In this study, B3LYP/6-31G(d) level of theory is used and transition states for the concerted reaction mechanism have been found. The stationary points analysis involved in the [4+2] cycloaddition reactions of TFE, 1 with furan, 2, thiophene, 3, and selenophene, 4 gave corresponding compound 2a, 2b, 3a, 3b, 4a, and 4b and are sketched in Scheme 1. The relative electronic energies of the transition states and their corresponding products in the gas phase are presented in Figs. 1-3. As shown from these figures, the *endo* transition states (TS2a for TFE+furan, TS3a for TFE+thiophene, and TS4a for TFE+selenophene) are 1.45, 0.52, and 0.1 kcal/mol higher than the *exo* transition states (TS2b for TFE+furan, TS3b for TFE+thiophene, and TS4b for TFE+selenophene), respectively.

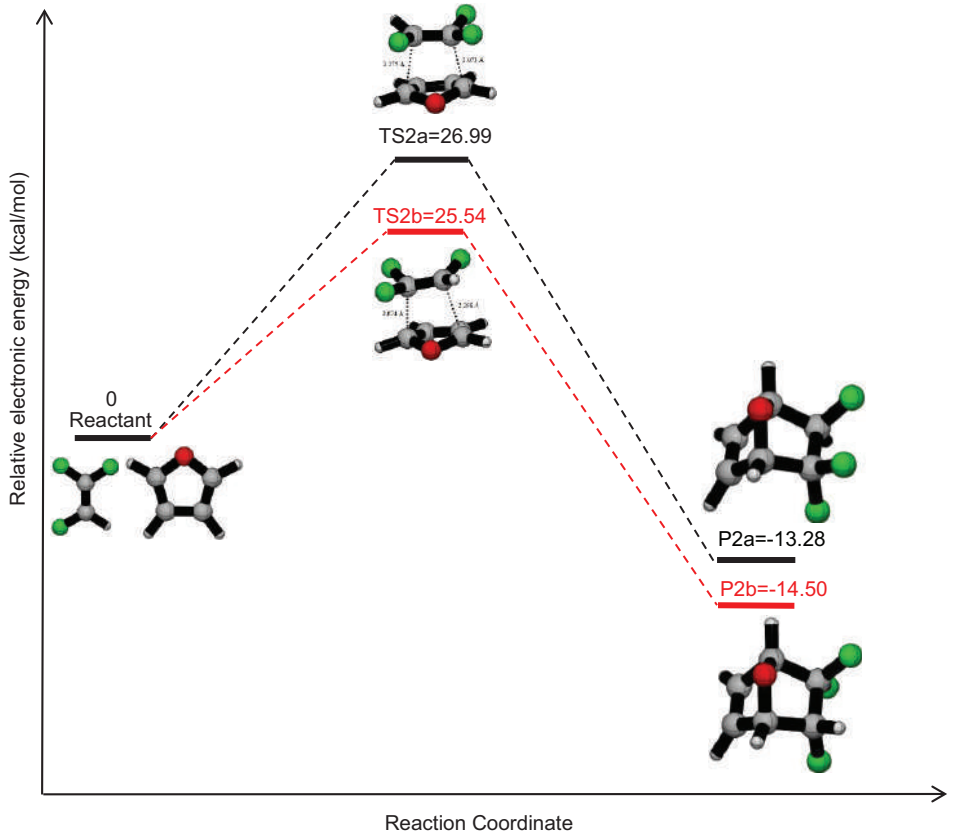

Fig. 1. Energy profile for the [4+2] cycloaddition reaction of trifluoroethylene with furan using B3LYP/6-31G(d) level of theory. The energies are given relative to reactants (R) (kcal/mol).

http://dx.doi.org/10.14500/aro.10575

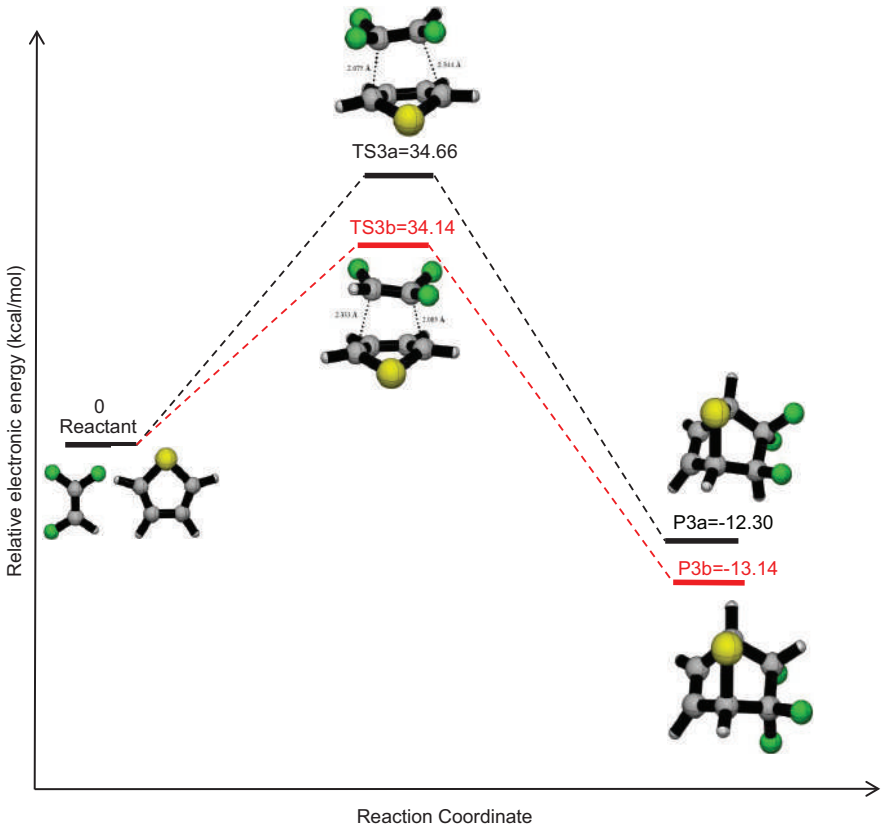

Fig. 2. Energy profile for the [4+2] cycloaddition reaction of trifluoroethylene with thiophene using B3LYP/6-31G(d) level of theory. The energies are given relative to reactants (kcal/mol).

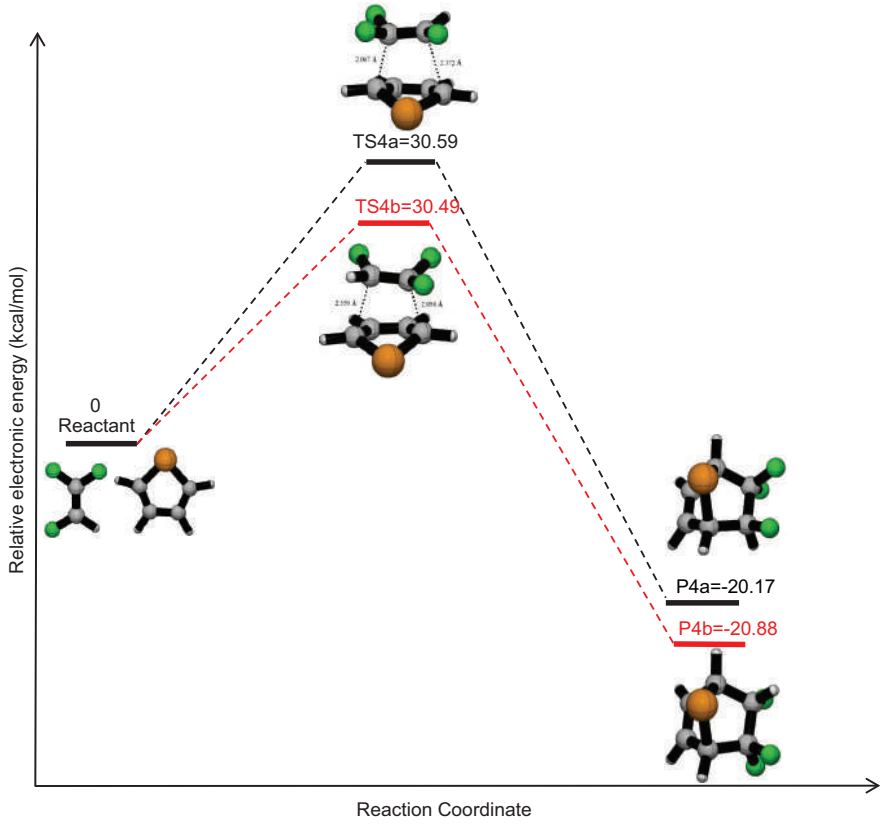

Fig. 3. Energy profile for the [4+2] cycloaddition reaction of trifluoroethylene with selenophene using B3LYP/6-31G(d) level of theory. The energies are given relative to reactants (kcal/mol).

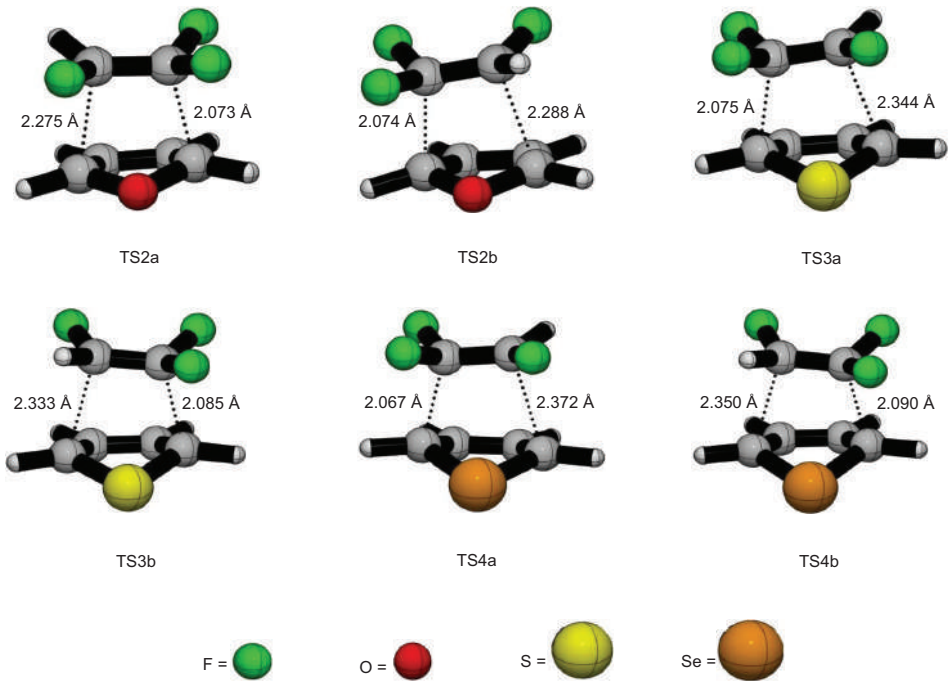

Fig. 4. Optimized geometries of the transition states involved in the [4+2] cycloaddition reactions of trifluoroethylene with furan, thiophene, and selenophene using B3LYP/6-31G(d) level of theory.

The activation energies for these [4+2] cycloaddition reactions are 26.99 kcal/mol for *endo* path and 25.54 kcal/mol for *exo* path for the reaction with furan. For the reaction of TFE with thiophene, the activation energies for *endo* path are 34.66 kcal/mol and for *exo* path are 34.15 kcal/mol. The activation energies for the reaction of TFE with selenophene are 30.58 and 30.49 kcal/mol for the *endo* and *exo* path, respectively. These results confirm that the *exo* reaction paths for three reactions are more favorable than *endo* reaction paths. Based on our knowledge, most of the studies of the *exo*- and *endo*-stereochemistry in the [4+2] cycloaddition reactions have shown that the *exo*-adduct is more stable thermodynamically whereas the *endo*-adduct is formed faster and kinetic control is observed (Cooley and Williams, 1997; Foster, et al., 2015; Hoffmann and Woodward, 1968; Lozynskyi, et al., 2016; Pavelyev, et al., 2016; Rulíšek, et al., 2005; Szalai, et al., 2007). However, in the current study, the *exo*-adduct is kinetically and thermodynamically more favorable than *endo*-adduct. Similar results were found for the [4+2] cycloaddition reaction of Zn-porphyrin trimer with butadiyne, nitroalkenes with methyl vinyl ether and intermolecular cycloaddition reaction of (Z)-1-(2-iodo-3-phenylprop- 2-enyl)-6-oxo-1,6-dihydropyridine-2-carbonitrile (Avalos, et al., 2000; Clyde-Watson, et al., 1998; Yuan and Yu, 2014).

The geometries of the transition states involved in the [4+2] cycloaddition reactions of the TFE with furan, thiophene, and selenophene are presented in Fig. 4. Studying the lengths of the formed bonds in the transition state indicates that these reactions follow asynchronous processes. The lengths, at the regioisomeric transition states, between the carbon atom with two fluorine atoms and carbon atom in heterocycles are shorter. Consequently, the sigma-sigma bond formation at the more electrophilic conjugated positions is more advanced than the other.

TABLE I
The Degree of Asynchronicity, Δd, at the Transition States

Transition states	Δd
TS2a	0.202
TS2b	0.214
TS3a	0.269
TS3b	0.248
TS4a	0.305
TS4b	0.260

The degree of a synchronicity (Δd) can be calculated by considering the lengths difference between the two forming bonds at the transition states. The values of Δd are reported in Table I. The analysis of Δd shows that the *endo* transition states are more asynchronous than the *exo* transition states when TFE reacts with thiophene and selenophene. However, in the case of TFE with furan the degree of asynchronicity of *exo* transition state is more than the *endo* transition state. It can be noted from the table that the Δd increases, for both *endo* and *exo* transition states, on proceeding from furan, through thiophene, and on to selenophene. It can be concluded that the presence of two fluorine atoms with high electronegativity on one side of the TFE leads to a more asynchronous transition states.

MP2 and CCSD(T) methods, using the same basis set, were used to calculate the reaction energies for the title reactions and the results were compared with B3LYP functional. Table II shows the reaction energies for each reaction at three different levels of theory. The MP2 and CCSD(T) methods

http://dx.doi.org/10.14500/aro.10575

both produce more negative reaction energies than B3LYP functional. It is worth to realize that the *exo* path for all reactions is more exothermic than the *endo* path at all levels of theory. This confirms that *exo*-adducts are more favorable than *endo*-adducts. In addition, the reaction energy decreases on proceeding from furan, through thiophene, and onto selenophene. The relative energies for products and transition states at B3LYP/6-31G(d) and MP2/6-31G(d) levels of theory are listed in Table III.

HOMO and LUMO energies in electron volt (eV) at B3LYP/6-31G(d) level of theory are computed for reactants and products, as shown in Table IV. The MO for the most stable *exo*-adducts are shown in Fig. 5. As shown form the results, the energy gap decrease on proceeding from furan to selenophene. It is worth to realize that the energy gap for *exo*-adducts is higher than the *endo*-adducts which indicates the stability of the *exo*-adducts.

The thermodynamic parameters for the [4+2] cycloaddition reactions of TEF with furan, thiophene, and selenophene in the gas phase at 1 atm and 298.15 K with B3LYP functional and MP2 method are listed in Table V. The activation enthalpies for these reactions range from 24.96 to 34.15 kcal/mol using B3LYP functional, whereas these values decrease when MP2 method is used. The activation enthalpies, as shown from the table, for the *exo* paths, are lower compared to the *endo* paths. All products are entropically disfavored. The values of Gibbs free energy for all *exo*-adducts are negative values, which refer to spontaneous reactions. The heat of formation for all products is negative which indicates the stability of these products. The values of Gibbs free energy for products 2a and 3a were found to be 0.56 and 1.76 kcal/mol and these values become more negative when MP2 method is used. However, the Gibbs free energy of 4a and 4b was –6.02 and −6.74 kcal/mol, respectively. These negative values indicate the spontaneity of reactions for both *exo*- and *endo*-adducts. Based on the observed data of thermodynamic parameters, it can be concluded that the *exo* reaction paths are formed faster and have lower heat of formation, thus the *exo* reaction paths are preferred thermodynamically as well as kinetically.

Products branching ratios (BR) were estimated using the method previously used by McFarland, et al., 1974 for all reactions to obtain the product percent yield. The BR for all possible products are collected in Table VI. As shown in Table VI, the *exo*-adducts for all reactions had a higher percent yield than *endo*-adducts. Similar results were obtained experimentally by Richard, et al. for the reaction of TFE with furan (Chambers, et al., 2000). The percent yield of *endo*-adducts increases only slightly on proceeding from

TABLE II
Reaction Energy (in kcal/mol) for Each Reaction at B3LYP/6-31G(d), MP2/6-31G(d) and CCSD(T)/6-31G(d) Levels of Theory

Reactions	Reaction energy (kcal/mol)		
	B3LYP	MP2	CCSD(T)
TFE+furan (*endo*)	−13.3	−24.44	−28.51
TFE+furan (*exo*)	−14.5	−25.88	−30.04
TFE+thiophene (*endo*)	−12.3	−24.89	−28.25
TFE+thiophene (*exo*)	−13.14	−26.03	−29.27
TFE+selenophene (*endo*)	−20.17	−33.38	−36.54
TFE+selenophene (*exo*)	−20.88	−34.38	−37.46

TABLE III
Relative Energies (ΔE) in (kcal/mol) Computed at B3LYP/6-31G(d) and MP2/6-31G(d) Levels of Theory

Structure	ΔE (B3LYP)	ΔE (MP2)
TFE+furan		
Reactants	0.00	0.00
P2a	−13.29	−24.44
TS2a	27.00	19.80
P2b	−14.50	−25.88
TS2b	25.54	18.12
TFE+thiophene		
Reactants	0.00	0.00
P3a	−12.30	−24.89
TS3a	34.66	25.24
P3b	−13.14	−26.03
TS3b	34.15	24.51
TFE+selenophene		
Reactants	0.00	0.00
P4a	−20.17	−33.38
TS4a	30.59	20.54
P4b	−20.88	−34.37
TS4b	30.50	20.27

TABLE IV
HOMO Energies, LUMO Energies, and Energy Gap (in eV unit) for Reactants and Products at B3LYP/6-31G(d) Level of Theory

Structure	HOMO	LUMO	Energy gap
TFE	−6.92	0.73	7.65
Furan	−6.11	0.54	6.64
Thiophene	−6.34	−0.21	6.13
Selenophene	−6.31	−0.33	5.97
P2a	−7.30	−0.48	6.81
P2b	−7.24	−0.37	6.88
P3a	−6.42	−1.13	5.30
P3b	−6.55	−1.11	5.44
P4a	−5.99	−1.46	4.54
P4b	−6.15	−1.48	4.67

HOMO: Highest occupied molecular orbital, LUMO: Lowest unoccupied molecular orbital

TABLE V
Thermodynamic Parameters for Transition States and Products at B3LYP/6-31G(d) and MP2/6-31G(d) Levels of Theory in (kcal/mole) for ΔH and ΔG and in (cal/mol.K) for ΔS

Structure	B3LYP			MP2		
	ΔH	ΔG	ΔS	ΔH	ΔG	ΔS
P2a	−14.47	0.56	−50.40	−25.72	−10.53	−50.96
P2b	−15.68	−0.66	−50.38	−27.16	−11.97	−50.96
P3a	−13.42	1.76	−50.92	−26.11	−10.73	−51.58
P3b	−14.25	0.93	−50.92	−27.25	−11.87	−51.58
P4a	−21.21	−6.02	−50.98	−34.52	−19.14	−51.56
P4b	−21.91	−6.74	−50.87	−35.50	−20.15	−51.48
TS2a	26.42	40.02	−45.61	19.10	32.96	−46.48
TS2b	24.96	38.54	−45.53	17.42	31.27	−46.44
TS3a	34.16	47.88	−46.03	24.63	38.62	−46.93
TS3b	33.63	47.36	−46.04	23.89	37.88	−46.94
TS4a	30.14	43.91	−46.22	19.99	34.03	−47.08
TS4b	30.05	43.81	−46.15	19.71	33.73	−47.02

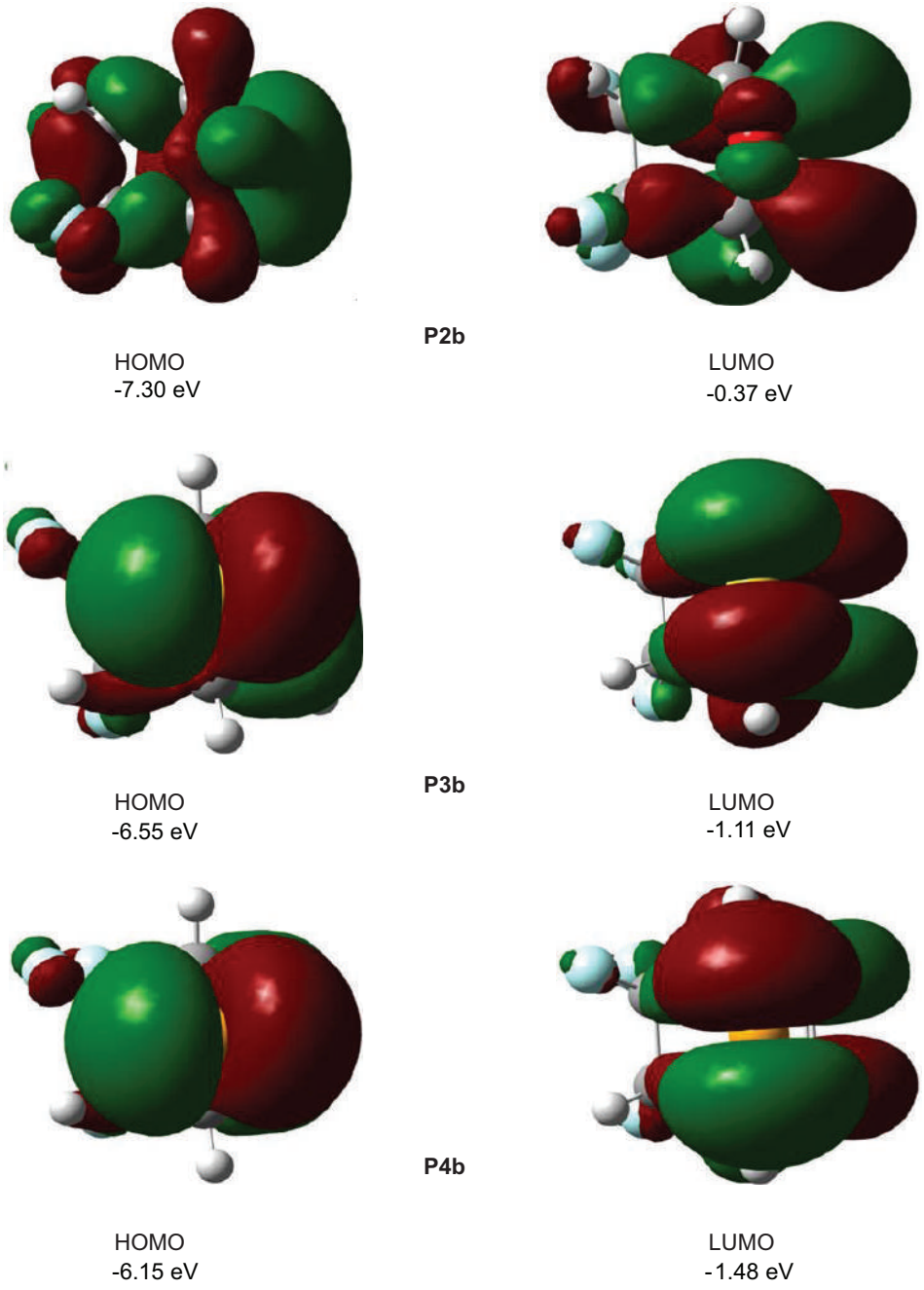

Fig. 5. B3LYP highest occupied molecular orbital and lowest unoccupied molecular orbital of the *exo*-adducts for all reactions at B3LYP/6-31G(d) level of theory.

TABLE VI
PRODUCT BRANCHING RATIOS AND PERCENT YIELD FOR *EXO*- AND *ENDO*-ADDUCTS

Products	Branching ratios	% Yield
P2a	0.114	11.40
P2b	0.886	88.60
P3a	0.1963	19.63
P3b	0.8037	80.37
P4a	0.2283	22.83
P4b	0.7717	77.17

furan, through thiophene, and on to selenophene: About 11.40 %, 19.63%, and 22.83%, respectively. However, the percent yield of *exo*-adducts decreases on proceeding from furan, through thiophene, and on to selenophene: About 88.60%, 80.37%, and 77.17%, respectively.

The global reactivity indices defined within the conceptual DFT is a powerful tool to study the reactivity in polar cycloaddition reactions. The static global properties, namely, chemical hardness (η), global nucleophilicity (N), global electrophilicity (ω), and electronic chemical potential (μ) for the reactants, TFE, furan, thiophene, and selenophene are listed in Table VII.

The electronic chemical potential (μ) of TFE, (μ = −3.10 eV), is lower than furan, (μ = −2.79 eV), indicating thereby that

http://dx.doi.org/10.14500/aro.10575

TABLE VII
THE CHEMICAL HARDNESS (η), ELECTRONIC CHEMICAL POTENTIAL (μ), GLOBAL ELECTROPHILICITY (ω), AND GLOBAL NUCLEOPHILICITY (N) FOR TRIFLUOROETHYLENE, FURAN, THIOPHENE, AND SELENOPHENE IN ELECTRON VOLT

Reactant	η	μ	ω	N
TFE	7.65	−3.10	0.63	1.86
Furan	6.64	−2.79	0.58	2.68
Thiophene	6.13	−3.27	0.87	2.45
Selenophene	5.97	−3.32	0.92	2.48

the net charge will be from the furan to the electron-deficient component, TFE. However, the electronic chemical potential of TFE is higher than thiophene (μ = −3.27 eV) and selenophene (μ = −3.23 eV) indicating that the net charge transfer will be from TEF to the thiophene and selenophene.

The power of electrophilicity for thiophene and selenophene is 0.87 and 0.92 eV, respectively, falls in the range of moderate electrophiles, whereas the for TFE and furan are 0.63 and 0.58 eV, respectively, falls in the range of marginal electrophiles within the ω scale (Domingo, et al., 2002). The electrophilicity power increases on proceeding from furan, through thiophene, and onto selenophene. Conversely, the power of nucleophilicity (N) decreases slightly on proceeding from furan, through selenophene, and onto thiophene: About 2.68, 2.48, and 2.45 eV, respectively.

IV. CONCLUSIONS

The B3LYP/6-31G(d) method was used to study the [4+2] cycloaddition reaction of TFE with furan, thiophene, and selenophene. The thermodynamic parameters associated with the formation of *exo* and *endo* stereoisomers in the gas phase were analyzed. These reactions are taking place through a concerted mechanism. It is observed that, on comparing the energetic results, the reaction paths leading to *exo*-adducts are thermodynamically and kinetically more favorable than *endo*-adducts. MP2 and CCSD(T) methods, using the same basis set, were used to compute the reaction energies and produced more negative reaction energies than B3LYP/6-31G(d) method. The percent yield of the *exo*-adducts is higher than the *endo*-adducts using the analysis of BR. This percent decreased on proceeding from furan to selenophene. The analysis of frontier MO indicates that the *exo*-adducts have larger energy gap than the *endo*-adducts and this indicates the stability of *exo*-adducts.

ACKNOWLEDGMENT

We would like to acknowledge the Department of Chemistry, Faculty of Science at University of Zakho and Department of Chemistry, College of Education at Salahaddin University.

REFERENCES

Avalos, M., Babiano, R., Bravo, J.L., Cintas, P., Jiménez, J.L., Palacios, J.C. and Silva, M.A., 2000, Understanding diastereofacial selection in carbohydrate-based domino cycloadditions: Semiempirical and DFT calculations. *Chemistry A European Journal*, 6(2), pp.267-77.

Baum, K., Archibald, T.G., Tzeng, D., Gilardi, R., Flippen-Anderson, J.L. and George, C., 1991. Synthesis and properties of 1,2-difluorodinitroethylene. *The Journal of Organic Chemistry*, 56(2), pp.537-539.

Chambers, R.D., Gilbert, A.F. ad Powell, R.L., 2000. Cycloaddition reactions of furan derivatives with trifluoroethene. *Journal of Fluorine Chemistry*, 104(2), pp.233-237.

Clyde-Watson, Z., Vidal-Ferran, A., J. Twyman, L.J., Walter, C.J., McCallien, D.W.J., Fanni, S., Bampos, N., Wylie, R.S. and Sanders, J.K.M., 1998. Reversing the stereochemistry of a diels alder reaction: Use of metalloporphyrin oligomers to control transition state stability. *New Journal of Chemistry*, 22(5), pp.493-502.

Cooley, J.H. and Williams, R.V., 1997. Endo and exo-stereochemistry in the diels-alder reaction: Kinetic versus thermodynamic control. *Journal of Chemical Education*, 74(5), p.582.

Cossío, F.P., Morao, I., Jiao, H. and Schleyer, P.V.R., 1999. In-plane aromaticity in 1,3-dipolar cycloadditions. Solvent effects, selectivity, and nucleus-independent chemical shifts. *Journal of the American Chemical Society*, 121(28), pp.6737-6746.

Ditchfield, R., Hehre, W.J. and Pople, J.A., 1971. Self-consistent molecular-orbital methods. IX. An extended gaussian-type basis for molecular-orbital studies of organic molecules. The Journal of Chemical Physics, 54(2), pp.724-728.

Domingo, L.R., Asensio, A. and Arroyo, P., 2002. Density functional theory study of the lewis acid-catalyzed diels alder reaction of nitroalkenes with vinyl ethers using aluminum derivatives. *Journal of Physical Organic Chemistry*, 15(9), pp.660-666.

Domingo, L.R., Aurell, M.J. and Pérez, P., 2014. The mechanism of ionic diels alder reactions. A DFT study of the oxa-Povarov reaction. *RSC Advances*, 4(32), pp.16567-16577.

Domingo, L.R., Aurell, M.J., Pérez, P. and Contreras, R., 2002. Quantitative characterization of the global electrophilicity power of common diene/dienophile pairs in diels alder reactions. *Tetrahedron*, 58(22), pp.4417-4423.

Domingo, L.R., Chamorro, E. and Pérez, P., 2008. Understanding the reactivity of captodative ethylenes in polar cycloaddition reactions. A theoretical study. *The Journal of Organic Chemistry*, 73(12), pp.4615-4624.

Essers, M., Mück-Lichtenfeld, C. and Haufe, G., 2002. Diastereoselective diels alder reactions of α-fluorinated α,β-unsaturated carbonyl compounds: Chemical consequences of fluorine substitution. *The Journal of Organic Chemistry*, 67(14), pp.4715-4721.

Fernández, I. and Bickelhaupt, F.M., 2014. Origin of the "endo rule" in Diels-Alder reactions. *Journal of Computational Chemistry*, 35(5), pp.371-376.

Foster, R.W., Benhamou, L., Porter, M.J., Bučar, D.K., Hailes, H.C., Tame, C.J. and Sheppard, T.D., 2015. Irreversible endo-selective Diels-Alder reactions of substituted alkoxyfurans: A general synthesis of endo-cantharimides. *Chemistry A European Journal*, 21(16), pp.6107-6114.

Frisch, M.J., Trucks, G.W., Schlegel, H.B., Scuseria, G.E., Robb, M.A., Cheeseman, J.R., Scalmani, G., Barone, V., Petersson, G.A., Nakatsuji, H., Li, X., Caricato, M., Marenich, A.V., Bloino, J., Janesko, B.G., Gomperts, R., Mennucci, B., Hratchian, H.P., Ortiz, J.V., Izmaylov, A.F., Sonnenberg, J.L., Williams-Young, D., Ding, F., Lipparini, F., Egidi, F., Goings, J., Peng, B., Petrone, A., Henderson, T., Ranasinghe, D., Zakrzewski, V.G., Gao, J., Rega, N., Zheng, G., Liang, W., Hada, M., Ehara, M., Toyota, K., Fukuda, R., Hasegawa, J., Ishida, M., Nakajima, T., Honda, Y., Kitao, O., Nakai, H., Vreven, T., Throssell, K., Montgomery Jr., J.A., Peralta, J.E., Ogliaro, F., Bearpark, M.J., Heyd, J.J., Brothers, E.N., Kudin, K.N., Staroverov, V.N., Keith, T.A., Kobayashi, R., Normand, J., Raghavachari, K., Rendell, A.P., Burant, J.C., Iyengar, S.S., Tomasi, J., Cossi, M., Millam, J.M., Klene, M., Adamo, C., Cammi, R., Ochterski, J.W., Martin, R.L., Morokuma, K., Farkas, O., Foresman, J.B. and Fox, D.J., 2009, *Gaussian 09 B.01*, Wallingford, CT.

Fukui, K., 1970. Formulation of the reaction coordinate. *The Journal of Physical Chemistry*, 74(23), pp.4161-4163.

Gregoritza, M. and Brandl, F.P., 2015. The Diels-Alder reaction: A powerful tool for the design of drug delivery systems and biomaterials. *European Journal of Pharmaceutics and Biopharmaceutics*, 97, pp.438-453.

Ho, G.M., Huang, C.J., Li, E.Y.T., Hsu, S.K., Wu, T., Zulueta, M.M.L., Wu, K.B. and Hung, S.C., 2016, Unconventional exo selectivity in thermal normal-electron-demand Diels-Alder reactions. *Scientific Reports*, 6, p.35147.

Hoffmann, R. and Woodward, R.B., 1968. Conservation of orbital symmetry. *Accounts of Chemical Research*, 1(1), pp.17-22.

Houk, K.N., Lin, Y.T. and Brown, F.K., 1986. Evidence for the concerted mechanism of the Diels-Alder reaction of butadiene with ethylene. *Journal of the American Chemical Society*, 108(3), pp.554-556.

Ito, H., Saito, A. and Taguchi, T., 1998. Asymmetric Diels-Alder reactions of 2-fluoroacrylic acid derivatives. Part 1: The construction of fluorine substituted chiral tertiary carbon. *Tetrahedron: Asymmetry*, 9(11), pp.1979-1987.

Ito, H., Saito, A., Kakuuchi, A. and Taguchi, T., 1999. Synthesis of 2-fluoro analog of 6-aminonorbornane-2,6-dicarboxylic acid: A conformationally rigid glutamic acid derivative. *Tetrahedron*, 55(44), pp.12741-12750.

Khabashesku, V.N., Kudin, K.N. and Margrave, J.L., 2001. Density functional theoretical studies of [2+2] cycloaddition of simple transient silenes and germenes to ethylene, formaldehyde, and thioformaldehyde, and vibrational analysis of spectra of reactants and cyclic products. *Russian Chemical Bulletin*, 50(1), pp.20-28.

Kohn, W. and Sham, L.J., 1965. Self-consistent equations including exchange and correlation effects. *Physical Review*, 140(4A), p.A1133.

Lautens, M. and Edwards, L.G., 1989. Stereoselectivity in the homo Diels-Alder reaction. *Tetrahedron Letters*, 30(49), pp.6813-6816.

Lee, C., Yang, W. and Parr, R.G., 1988. Development of the Colle-Salvetti correlation-energy formula into a functional of the electron density. *Physical Review B*, 37(2), pp.785-789.

Legault, C., 2009, *CYLview 1.0*. Université de Sherbrooke, Sherbrooke.

Lemal, D.M., 2017. Pathways for concerted [2+2] cycloaddition to cumulenes. *The Journal of Organic Chemistry*, 82(24), pp.13012-13019.

Leroy, J., Molines, H. and Wakselman, C., 1987. Facile synthesis of ethyl 3,3-difluoroacrylate from dibromodifluoromethane and Diels-Alder cycloaddition with furan. *The Journal of Organic Chemistry*, 52(2), pp.290-292.

Levandowski, B.J., Hamlin, T.A., Helgeson, R.C., Bickelhaupt, F.M. and Houk, K., 2018. Origins of the endo and exo selectivities in cyclopropenone, iminocyclopropene, and triafulvene Diels-Alder cycloadditions. *The Journal of Organic Chemistry*, 83(6), pp.3164-3170.

Liu, J., Niwayama, S., You, Y. and Houk, K.N., 1998. Theoretical prediction and experimental tests of conformational switches in transition states of Diels-Alder and 1,3-dipolar cycloadditions to enol ethers. *The Journal of Organic Chemistry*, 63(4), pp.1064-1073.

Lozynskyi, A., Zimenkovsky, B., Karkhut, A., Polovkovych, S., Gzella, A.K. and Lesyk, R., 2016. Application of the 2(5H)furanone motif in the synthesis of new thiopyrano[2,3-d]thiazoles via the hetero-Diels-Alder reaction and related tandem processes. *Tetrahedron Letters*, 57(30), pp.3318-3321.

McFarland, M., Albritton, D.L., Fehsenfeld, F.C., Ferguson, E.E. and Schmeltekopf, A.L., 1974. Energy dependence and branching ratio of the $N2^{+}$ + O reaction. *Journal of Geophysical Research* (1896-1977), 79(19), pp.2925-2926.

Nickon, A., Kwasnik, H.R., Mathew, C.T., Swartz, T.D., Williams, R.O. and DiGiorgio, J.B., 1978. Synthesis and structure proof of C-2 and C-4 monofunctionalized brexanes and brendanes. *The Journal of Organic Chemistry*, 43(20), pp.3904-3916.

Nicolaou, K.C., Snyder, S.A., Montagnon, T. and Vassilikogiannakis, G., 2002. The Diels-Alder reaction in total synthesis. *Angewandte Chemie International Edition*, 41(10), pp.1668-1698.

Parr, R.G. and Pearson, R.G., 1983. Absolute hardness: Companion parameter to absolute electronegativity. *Journal of the American Chemical Society*, 105(26), pp.7512-7516.

Parr, R.G. and Weitao, Y., 1989. *Density-Functional Theory of Atoms and Molecules*. Oxford University Press, Oxford.

Parr, R.G. and Weitao, Y., 1994. *Density-Functional Theory of Atoms and Molecules*. Oxford University Press, Oxford.

Parr, R.G., Szentpály, L.V. and Liu, S., 1999. Electrophilicity index. *Journal of the American Chemical Society*, 121(9), pp.1922-1924.

Pavelyev, R.S., Vafina, R.M., Lodochnikova, O.A., Galiullina, A.S., Romanova, E.I., Balakin, K.V. and Shtyrlin, Y.G., 2016. Stereochemistry of hexachlorocyclopentadiene [4+2]-cycloaddition to 2-substituted 4,7-dihydro-1,3-dioxepins. *Tetrahedron Letters*, 57(35), pp.3902-3907.

Rivero, U., Meuwly, M. and Willitsch, S., 2017a. A computational study of the Diels-Alder reactions between 2,3-dibromo-1,3-butadiene and maleic anhydride. *Chemical Physics Letters*, 683, pp.598-605.

Rivero, U., Meuwly, M. and Willitsch, S., 2017b. A computational study of the Diels-Alder reactions between 2, 3-dibromo-1, 3-butadiene and maleic anhydride. *Chemical Physics Letters*, 683, pp.598-605.

Rulíšek, L., Šebek, P., Havlas, Z., Hrabal, R., Čapek, P. and Svatoš, A., 2005. An experimental and theoretical study of stereoselectivity of Furan-Maleic anhydride and Furan-Maleimide Diels-Alder reactions. *The Journal of Organic Chemistry*, 70(16), pp.6295-6302.

Silva, M.A.A. and Goodman, J.M., 2002. Nitrone cyclisations: The development of a semi-quantitative model from ab initio calculations. *Tetrahedron*, 58(19), pp.3667-3671.

Szalai, M.L., McGrath, D.V., Wheeler, D.R., Zifer, T. and McElhanon, J.R., 2007. Dendrimers based on thermally reversible Furan-Maleimide Diels-Alder adducts. *Macromolecules*, 40(4), pp.818-823.

Teixeira, F., Rodríguez-Borges, J.E., Melo, A. and Cordeiro, M.N.D., 2009. Stereoselectivity of the aza-Diels-Alder reaction between cyclopentadiene and protonated phenylethylimine derived from glyoxylates. A density functional theory study. *Chemical Physics Letters*, 477(1), pp.60-64.

Woodward, R.B. and Katz, T.J., 1959. The mechanism of the Diels-Alder reaction. *Tetrahedron*, 5(1), pp.70-89.

Yuan, L. and Yu, H.T., 2014. Cascade cyclization of 1-(2-yl-3-phenylprop-2-enyl)-6-oxo-1,6-dihydropyridine-2-carbonitrile radical: Mechanistic insights from DFT study. *Computational and Theoretical Chemistry*, 1044, pp.1-9.

General Information

ARO's Mission: ARO seeks to publish those papers that are most influential in their fields or across fields and that will significantly advance scientific understanding. Selected papers should present novel and broadly important data, syntheses, or concepts. They should merit the recognition by the scientific community and general public provided by publication in ARO, beyond that provided by specialty journals.

We welcome submissions from all fields of natural science and technology, and from any source. We are committed to the prompt evaluation and publication of submitted papers. ARO is published biannually; selected papers are published online ahead of print.

Submission

Manuscripts should be submitted by the correspondent authors of the manuscript via the on-line submission page. Regardless of the source of the word-processing tool, only electronic Word (.doc, .docx, .rtf) files can be submitted on-line. There is no page limit. Only online submissions are accepted to facilitate rapid publication and minimize administrative costs. Submissions by any other one but the authors will not be accepted. The submitting author takes responsibility for the paper during submission and peer review. If for some technical reason submission through the email is not possible, the author can contact aro.journal@koyauniversity.org for support. Before submitting please check ARO's guide to authors thoroughly to avoid any delay in the review and publication process.

Authors are explicitly responsible for the language of their texts. Paper should be submitted in a well written in understandable English. Authors should not expect the editor or editorial board to rewrite their paper. Prior to submission, authors should have their paper proofread by a possible academic native speaker of English.

- Submit the Article with contact Information
- File name should be your article tittle
- Don't submit your article in multiple journal, we are taking only minimum time for review process. please don't waste our time
- Once the paper is accepted, it can't be withdrawn
- Please follow publication ethics and regulation
- Avoid plagiarism and copied material
- Strictly Follow ARO's Template

Terms of Submission

Papers must be submitted on the understanding that they have not been published elsewhere and are not currently under consideration by another journal or any other publisher. ARO accepts original articles with novel impacts only. Post conference papers are not accepted "as is", however, regular papers on the same topic but with a different title can be submitted. The new paper should contain significant improvements in terms of extended content, analysis, comparisons with popular methods, results, figures, comments, etc. Please do not forget that the publication of the same or similar material in ARO constitutes the grounds for filing of an (auto) plagiarism case.

The submitting author is responsible for ensuring that the article's publication has been approved by all the other co-authors. It is also the authors' responsibility to ensure that the articles emanating from a particular institution are submitted with the approval of the necessary institution. Only an acknowledgement from the editorial office officially establishes the date of receipt. Further correspondence and proofs will be sent to the author(s) before publication unless otherwise indicated. It is a condition of submission of a paper that the authors permit editing of the paper for readability. All enquiries concerning the publication of accepted papers should be addressed to aro.journal@koyauniversity.org.

Peer Review

All manuscripts are subject to peer review and are expected to meet standards of academic excellence. Submissions will be considered by an editor and "if not rejected right away" by peer-reviewers, whose identities will remain anonymous to the authors.

Guide to Author

We welcome submissions from all fields of science and from any source. We are committed to the prompt evaluation and publication of submitted papers. Selected papers are published online ahead of print. Authors are encouraged to read the instructions below before submitting their manuscripts. This section arranged into an overview speedy guidelines below and more detailed at the bottom section of this page

Manuscript Preparation

Submitting your manuscript will be in two stages namely before final acceptance and after.

Stage one:

At the first stage manuscript needs to be prepared electronically and submitted online via the online submission page in a Word (.doc, .docx, .rtf) format of one column double-spaced page, Times New Roman font type, and 12 p font size. A pdf version of the submitted manuscript should be submitted too. All authors' names, affiliations, e-mail addresses, and mobile phone numbers should be typed on a cover page, indicating the correspondent author.

Stage two:

- File type: MS-Word version 2003 or later.
- Format: The preferred format of the manuscript two-column template with figures and captions included in the text. This template can be downloaded via the following link. Please follow instructions given in the template; http://aro.koyauniversity.org/about/submissions#onlineSubmissions
- Text: All text is in Times New Roman font. The main text is 10-point, abstract is 9-point font and tables, references and captions are 8-point font.
- Figures: Figures should be easily viewed on a computer screen.

Units of Measurement

Units of measurement should be presented simply and concisely using System International (SI) units.

Title and Authorship Information

The following information should be included;

- Paper title.
- Full author names.
- Affiliation.
- Email addresses.

Abstract
The manuscript should contain an abstract. The abstract should be self-contained and citation-free and should not exceed 200 words.

Introduction
This section should be succinct, with no subheadings.

Materials and Methods
This part should contain sufficient detail so that all procedures can be repeated. It can be divided into subsections if several methods are described.

Results and Discussion
This section may each be divided by subheadings or may be combined.

Conclusions
This should clearly explain the main conclusions of the work highlighting its importance and relevance.

Acknowledgements
All acknowledgements (if any) should be included at the very end of the paper before the references and may include supporting grants, presentations, and so forth.

References
References must be included in the manuscript and authors are responsible for the accuracy of references. Manuscripts without them will be returned. ARO is following Harvard System of Referencing. (Learn how to import and use Harvard Styling in your Microsoft Office by following this link:
http://bibword.codeplex.com/releases/view/15852)

Preparation of Figures
Upon submission of an article, authors are supposed to include all figures and tables in the PDF file of the manuscript. Figures and tables should be embedded in the manuscript. Figures should be supplied in either vector art formats (Illustrator, EPS, WMF, FreeHand, CorelDraw, PowerPoint, Excel, etc.) or bitmap formats (Photoshop, TIFF, GIF, JPEG, etc.). Bitmap images should be of 300 dpi resolution at least unless the resolution is intentionally set to a lower level for scientific reasons. If a bitmap image has labels, the image and labels should be embedded in separate layers.

Preparation of Tables
Tables should be cited consecutively in the text. Every table must have a descriptive title and if numerical measurements are given, the units should be included in the column heading. Vertical rules should not be used.

ARO Reviewer/Associate Editor Application Form

ARO is a scientific journal of Koya University (p-ISSN: 2410-9355, e-ISSN: 2307-549X) which aims to offer a novel contribution to the study of Science. The purpose of ARO is twofold: first, it will aim to become an ongoing forum for debate and discussion across the sciences and Engineering. We hope to advance our problem solving capacity and deepen our knowledge regarding a comprehensive range of collective actions. Second, ARO accepts the challenges brought about by multidisciplinary scientific areas and aspires to expand the community of academics who are able to learn from and help to produce advances in a variety of different disciplines.

The Journal is seeking reviewers who can provide constructive analysis of papers thus enhancing overall reputation of the Journal. If any expert is interested in participating of the review process, we highly encourage you to sign up as a reviewer for our Journal and help us improve our presence in domain of your expertise. Appropriate selection of reviewers who have expertise and interest in the domain relevant to each manuscript are essential elements that ensure a timely, productive peer review process. We require proficiency in English.

How to apply

To apply for becoming a reviewer of ARO, please submit the application form by following the link:
http://aro.koyauniversity.org/user/register
To apply for becoming a member of the Editorial Board of ARO, please submit the application form by following the link: http://aro.koyauniversity.org/pages/view/AEB

Both Associate Editor and Reviewers should specify their areas of research and expertise. Applicants must have a doctorate (or an equivalent degree), and if Master degree they need to have significant publishing experience. Please note that;

- You will need to write your full official name.
- Please provide an email which reflects your official name, such as nameOne.NameTwo@... , or your institute's official email.
- All data need to be written in English.

Note: For more information, kindly visit the following websites:

1. aro.koyauniversity.org.
2. http://libweb.anglia.ac.uk/referencing/harvard.htm.
3. http://bibword.codeplex.com/releases/view/15852.

INDEXING


THOMSON REUTERS
Emerging Sources Citation Index
WEB OF SCIENCE™


Crossref


OCLC
WorldCat


PRESERVED IN
LOCKSS


INDEXED IN
DOAJ


Google
Scholar


SHERPA
RoMEO


ROAD
DIRECTORY
OF OPEN ACCESS
SCHOLARLY
RESOURCES


ResearchGATE
scientific network

Koya University (KOU) is a young university established in 2003 and it is located in the city of Koya (Koysinjaq), short distance to the East of the regional capital city of Erbil (Arbil, Hewlêr) in Kurdistan Region of Iraq. It is on the foothills of beautiful High Mountain. Its campus has been carefully laid out to embrace the beautiful mountainous nature. The Koya University has a Faculty system which enhances the interactions between similar academic fields. Today, Koya University has four Faculties: Engineering, Science and Health, Humanities and Social Sciences and Education in addition to the School of Medicine, which all consist of twenty-five scientific departments in different fields, such as Petroleum Engineering, Geotechnical Engineering, Software Engineering, Physics, Chemistry, Clinical Psychology, Social Science, Medical Microbiology and Sport Education.

ARO-The Scientific Journal of Koya University is a biannual journal of original scientific research, global news, and commentary in the areas of Science and Technology. ARO is a Peer-reviewed Open Access journal with CC BY-NC-SA 4.0 license. It provides immediate, worldwide and barrier-free access to the full text of research articles without requiring a subscription to the journal, and has no article processing charge (APC). ARO Journal seeks to publish those papers that are most influential in their fields or across fields and that will significantly advance scientific understanding. ARO Journal is a member of ROAD and Crossref agencies and has got ESCI, DOAJ seal, SHERPA/RoMEO deposit policy, and LOCKSS archiving policy.

KOYA UNIVERSITY

Aro the Scientific Journal Office
Koya University (KOU)
University Park
Danielle Mitterrand Boulevard
Koya KOY45, Kurdistan Region - Iraq
aro.koyauniversity.org

ISSN: 2410-9355 (printed version) ISSN: 2307-549X (electronic version)
ARO - DOI: 10.14500/2307-549X